POLITECNICO DI TORINO
&
ISAE-SUPAERO

A.y. 2024-2025

Politecnico
di Torino

Global stability analysis of a two-dimensional open cavity flow

Supervisors:
Prof. Daniela Tordella
Prof. Gabriele Nastro

Student:
Tommaso Talamucci

Abstract

This thesis presents a global stability analysis of two-dimensional open cavity flows, focusing on the influence of Reynolds and Mach numbers on flow instabilities. The study is conducted using the high-order compressible flow solver IC3, developed by ISAE-Supaero, which enables direct numerical simulations and global stability computations through a matrix-free approach. To ensure the reliability of the numerical framework, different domain geometries and boundary conditions are examined and validated. The linearized Navier-Stokes equations are used to identify dominant instability modes and their dependence on flow parameters. Comparisons with existing results from literature validate the solver's implementation, and the analysis reveals critical thresholds and behaviors associated with the primary shedding modes. These findings contribute to the understanding of instability mechanisms in compressible open cavity flows and support future efforts in flow control design.

Contents

1 Introduction **1**
- 1.1 Context . . . 1
- 1.2 Governing Equations . . . 2
- 1.3 Phenomenology . . . 3
  - 1.3.1 Kelvin-Helmholtz Instability and Shedding . . . 4
- 1.4 Numerical analysis . . . 5
  - 1.4.1 DNS analysis . . . 5
  - 1.4.2 IC3 . . . 5
- 1.5 Stability Analysis . . . 6
- 1.6 Internship goals . . . 8

2 Stability theory **9**
- 2.1 Linear Stability Theory . . . 9
- 2.2 Base Flow characteristics . . . 11
  - 2.2.1 Modal and Non-Modal Analysis . . . 11
  - 2.2.2 Local and Global Approaches . . . 12
- 2.3 Local approach . . . 13
  - 2.3.1 Spatial and Temporal Theory . . . 13
  - 2.3.2 Dispersion relation and phase velocity . . . 14
- 2.4 Global approach . . . 15
  - 2.4.1 Primary and secondary instabilities . . . 15
  - 2.4.2 Primary instability and bifurcations . . . 17
  - 2.4.3 Limit cycle instabilities . . . 18
  - 2.4.4 Resolution of the EV problem . . . 20
  - 2.4.5 Arnoldi algorithm and Krylov Schur method . . . 20
  - 2.4.6 Implementation in IC3 . . . 22

3 Numerical stability methods and parametric influences on open cavity flows **23**
- 3.1 Numerical methods for stability analyses . . . 23
  - 3.1.1 Modal analysis . . . 24
  - 3.1.2 Non-modal analysis . . . 26
- 3.2 Influence of control parameters . . . 29
  - 3.2.1 Influence of the perturbation's location . . . 29
  - 3.2.2 Influence of the perturbation's frequency . . . 32
  - 3.2.3 Influence of the Mach number . . . 33
  - 3.2.4 Influence of the Reynolds number . . . 40
  - 3.2.5 Influence of the boundary layer thickness . . . 41

3.2.6 Influence of the aspect ratio 42

4 Analysis of a cavity invested by a flow at $Re = 502$ and $M = 0.6$ 44
4.1 Physical domain 45
4.1.1 Boundary conditions 45
4.1.2 Initial conditions 47
4.1.3 Mesh 48
4.2 Numerical Methods 50
4.3 Frequency spectrum 53
4.3.1 Fast Fourier Transform 53
4.3.2 Results 54
4.4 Stability analysis 58
4.4.1 Base flow determination using SFD 59
4.4.2 Perturbation around the base flow 63
4.4.3 Dispersion relation 68
4.4.4 Phase velocity 74
4.4.5 Limit cycle 77

5 Influence of the Reynolds and Mach numbers 79
5.1 Influence of the Reynolds number 79
5.2 Influence of the Mach number 88

6 Conclusions 94

List of Figures

1.1 Open cavity flow scheme (taken from Cattafesta et al. [4]) 3
1.2 Shear flows' velocity profile 4
1.3 Behaviours of the flow when the perturbation applied to it is gradually amplified 6
1.4 Representation of three different cases where the perturbation's amplitude grows, taken from Cherubini, Picella, and Robinet [9] 7
1.5 Von Karman vortex trail 8

2.1 Mechanics of a point particle 9
2.2 Wake behind a cylinder 16
2.3 Representation on the phase space of the attractors 17
2.4 Schematic representation of the Hopf bifurcation in the phase space . 18
2.5 Schematic representation of the Poincaré map 19
2.6 Krylov-Schur method 21

3.1 Representation of non-orthogonal vectors 24
3.2 2D Poiseuille flow eigenspectrum and neutral curve obtained using non-modal analysis 28
3.3 Domain used by Citro et al. [24] 30
3.4 Absolute value of the direct and adjoint eigenfunctions of the four unstable modes identified by Citro et al. [24] 31
3.5 Sensitivity of the first unstable mode (the wavemaker) as found by Citro et al. [24] 31
3.6 Instantaneous numerical schlieren, instantaneous vorticity contours and time averaged streamlines shown for different Mach numbers, aspect ratio $\frac{L}{D} = 6$ and $Re_\theta = 19$. Taken from Sun et al. [26] 34
3.7 Physical domain used by Yamouni, Sipp, and Jacquin [29] 35
3.8 Eigenspectrum of an open cavity flow at $Re = 7500$ for different Mach numbers (Yamouni, Sipp, and Jacquin [29]) 36
3.9 Location of the k branches with the Rossiter feedback aeroacoustic mechanism (taken from Yamouni, Sipp, and Jacquin [29]) 37
3.10 Spatio-temporal evolution of the global modes of the branch $k = 3$ (taken from Yamouni, Sipp, and Jacquin [29]) 38
3.11 Pressure field of a cavity in a channel flow at $Re = 2900$ and $M = 1e^{-3}$ (taken from Bailey, Abbá, and Tordella [30]) 39

3.12 Picture taken from Bailey, Abbá, and Tordella [30]. The dimensioned absolute values of the pressure and kinetic energy transport are showed for a cavity at $M = 1e^{-3}$ at different Reynolds numbers. The dots represent the pressure transport, while the squares the kinetic energy transport. We put the focus on the change in behaviour obtained after $Re = 1000$. It is in fact possible to distinguish a descending behaviour of the pressure transport interpolation curve (meaning pressure outflow from the cavity becomes greater than the inflow). This behaviour is considered to be a consequence of the generation of acoustic waves leaving the cavity. The kinetic energy transport also sees a change in the behaviour going from an exponential growth to a logarithmic one. $Re = 1000$ is then considered the first occurrence of unsteadiness (instabilities). 40
3.13 Eigenspectrum for a cavity with aspect ratio $\frac{L}{D} = 1$, $M \approx 0$ and $Re = 7500$ showed for different ratios $\frac{L}{\theta_0}$ (Yamouni, Sipp, and Jacquin [29]) 42
3.14 Neutral curve of an open cavity flow showed for different aspect ratios (Meseguer-Garrido et al. [31]) 43

4.1 Fluid domain adopted in the simulations 44
4.2 Fluid regions definition 45
4.3 Schematic representation of the possible fluctuations occuring at the top surface of the domain 46
4.4 Boundary conditions applied to the two different configurations of fluid domain 47
4.5 Initial mesh used to run the simulations containing 379000 elements . 48
4.6 Pressure visualization inside the domain that makes it possible to observe fluctuations coming from the outer boundary of the domain . 49
4.7 Location of the sponge zones inside the domain 49
4.8 Final meshes used for the analyses for the two configurations of domain 50
4.9 Representation of a quad element studied using finite volumes method 51
4.10 Representation of a quad element studied using spectral differences methods 52
4.11 Virtual probes used for the determination of the frequency spectrum . 52
4.12 FFT spectrum of the normalized streamwise velocity 54
4.13 Comparison between the spectrum obtained using the IC3 solver and the one obtained by Sun et al. 55
4.14 Frequency spectrum obtained considering the whole field 56
4.15 Comparison between the spectrum obtained using the flat TOP surface and the inclined one 57
4.16 Mesh used for the comparison between the SD2 method and finite volumes 57
4.17 Comparison between the spectrum obtained using the finite volumes method and the spectral differences SD2 58
4.18 Absolute residuals obtained applying the Selective Frequency Damping 61
4.19 Base flow's streamlines 61

4.20 Semi-logarithmic plot of the streamwise velocity U_x, the density ρ and the total energy E using finite volumes and spectral differences to obtain the base flow 62
4.21 Eigenspectra obtained perturbing the base flow using the IC3 solver . 64
4.22 Eigenspactra comparison between the one obtained by Sun et al. and the one determined using the IC3 solver 65
4.23 Algebraic growth representation until the saturation of the disturbances 66
4.24 Velocity profile on the upstream edge of the cavity 67
4.25 Contours of the real part of $\hat{U}_x$ of the eigenvectors of the modes I, II, IV 67
4.26 Line probe used to obtain informations about the perturbations' wave lengths 68
4.27 Spatial FFT spectra executed on the real part of $\hat{U}_x$ to determine the dominant α of the four modes 69
4.28 Virtual rulers used to qualitatively visualize the wave lengths of the four modes 70
4.29 Virtual ruler applied on the visualizations from Sun et al. [11] 70
4.30 Comparison between the acoustic wave visualizations obtained by Bailey, Abbá, and Tordella [30] and using IC3 72
4.31 Visualization of the pressure field of the dominant mode for the case at $Re = 502$ and $M = 0.4$ 73
4.32 Dispersion relation 74
4.33 Phase velocity differences qualitatively plotted for $t = t_0$ 75
4.34 Phase velocity differences qualitatively plotted for $t = t_f$ 76
4.35 Summarizing representation of the eigenspectra, the dispersion relation and the phase velocities for the four modes 77
4.36 Limit cycle 78
4.37 Limit cycle (section $u - \dot{u}$) 78

5.1 Influence of the Reynolds number on the shedding frequency 81
5.2 Fixed points (base flows) at different Reynolds numbers 82
5.3 Eigenspectra showing the Reynolds influence on the global modes . . 83
5.4 Eigenvalues' evolution while increasing the Reynolds number: comment on each mode 84
5.5 Critic Reynolds 85
5.6 Non-negligible modes appearing as the Reynolds increases 86
5.7 Influence of the Reynolds number on $\omega_r^*(\alpha)$ and $St_D(\alpha)$ 87
5.8 Mach influence on the frequency spectrum 89
5.9 Base flows obtained with different Mach numbers 90
5.10 Eigenspectra under the Mach influence 91
5.11 Behaviour of each mode under the Mach influence 92
5.12 Visualization of the eigenmodes at $M = 0.4$ showed as contours of the real part of $\frac{\hat{U}_x}{u_\infty}$ 93

List of Tables

4.1 Table containing the initial condition values and reference physics values imposed in the simulation for a flow at $Re = 502$ an $M = 0.6$. . 47
4.2 Table containing the first three harmonics' Strouhal number and frequency in the FFT spectrum for a flow at $Re = 502$ and $M = 0.6$. . . 56
4.3 Table containing the values of the parameters χ and Δ of the SFD method. The gain (χ) is the parameter that turns the approximated most unstable eigenvalue stable, while Δ is the filter width. 60
4.4 Table showing the comparison between the eigenvalues determined by Sun et al. and the ones determined doing a stability analysis on IC3 perturbing the base flow. The eigenvalues are listed from I to IV going from the most amplified mode (that represents the shedding mode) to the least amplified one. It is possible to see that there are some differences in the results. These can be related to a slight difference in the boundary layer momentum thickness θ. 65
4.5 Wavelengths and wave numbers of the dominant modes. 69
4.6 Comparison of the wavelengths determined using IC3 and by Sun . . 71
4.7 Comparison of the parameters adopted by Bailey, Abbá, and Tordella [30] and in the present work 71
4.8 Phase velocities of the different modes 74

5.1 Reynolds numbers used for studying its influence on the development of the instabilities 80
5.2 Influence of the Reynolds number on St_D and parameters used for the SFD 81
5.3 Table containing the dominant wave numbers for the four modes denoting the shedding phenomena. They are determined applying a spatial FFT to the signal over a line inside the shear layer along the x direction. 83
5.4 Mach numbers used for studying its influence on the development of the instabilities 88
5.5 Influence of the Mach number on St_D and parameters used for the SFD 89

Chapter 1

Introduction

1.1 Context

Cavity flows have been a significant topic of interest in the first years of 21st century, as it is well evidenced by the recent review articles produced (Louis Cattafesta et al. [1], Rowley and Williams [2] to cite some of them). However, as with other archetypical flows, it is still possible to exploit existing knowledge to deepen our understanding of certain physical behaviours of flows in general that remain unresolved. Recent works show that the interest in these flows is still relevant [3]. For this purpose, cavities are widely used in the study of flow stability because, as the Reynolds number increases, they are characterized by a rapid generation of unstable motions, which tend to transition the flow to turbulence.
By studying flow stability using numerical codes, the aim is to one day achieve a better ability to reduce losses caused by flows becoming turbulent.
From a practical perspective, cavity flows are observed in the aeronautical field, near landing gear bays, hatches, or even small surface irregularities on an aircraft. Determining how these behave when subjected to high Reynolds number and compressible flow regimes (approximately high Mach numbers) can, in practical terms, lead to the development of control methods that reduce flow instabilities around an aircraft, thereby reducing losses.
The interest in cavity flows then re-emerged these late years by studying possible ways to suppress the oscillations in the flow-field. Passive methods were insightfully examined by Prudhomme et al. [3], that could create a passive control method for oscillations changing the shape of the rear edge of the cavity. In order to study different configuration to optimize the control methods, it is mandatory to have a clear and accurate knowledge about the flow characteristics in different regimes, especially going towards transonic flow conditions. It is then necessary to preliminary determine the flow instabilities.
The study of instabilities is part of a specific field of fluid dynamics called *hydrodynamic stability*, which emerged in the late nineteenth century through the works of Helmholtz, Kelvin, Rayleigh, and Reynolds. The studies primarily investigated low Reynolds number flows under terrestrial conditions, thus treated numerically as incompressible flows. For years, technological limitations prevented moving away from these conditions, which, however, have become of great interest in the last decade as potential applications expand: stratospheric flight, Martian exploration, or the development of active turbulence control devices are just a few of the goals

requiring a departure from low Reynolds number and incompressible conditions.
To achieve these goals, it is therefore necessary to investigate high Reynolds and compressible flows, but a solid physical foundation is still lacking.
With this thesis, we aim to contribute to this field, enhancing the understanding of these specific flows.

1.2 Governing Equations

The motion of a compressible Newtonian fluid is fully described by the Navier-Stokes equations, derived by applying the conservation laws of mass, momentum, and energy. In their conservative three-dimensional form for an ideal gas, they are expressed as:

$$\begin{cases} \dfrac{\partial \rho}{\partial t} + \nabla \cdot (\rho \mathbf{u}) = 0 \\ \dfrac{\partial \rho \mathbf{u}}{\partial t} + \nabla \cdot (\rho \mathbf{u} \otimes \mathbf{u}) = -\nabla p + \nabla \cdot \left[\mu(\nabla \mathbf{u} + \nabla \mathbf{u}^T) - \dfrac{2}{3}\mu \nabla \cdot \mathbf{u} \delta_{ij} \right] \\ \dfrac{\partial \rho E}{\partial t} + \nabla \cdot (\rho \mathbf{u} E + p\mathbf{u}) = \nabla \cdot (K \nabla T) + \nabla \cdot \left(\mathbf{u} \left[\mu(\nabla \mathbf{u} + \nabla \mathbf{u}^T) - \dfrac{2}{3}\mu \nabla \cdot \mathbf{u} \delta_{ij} \right] \right) \end{cases} \tag{1.1}$$

where ρ is the fluid density, $\mathbf{u}$ the velocity vector, p the pressure, T the temperature, and E the total energy. The viscosity μ and thermal conductivity K are considered constant.
From now on, the system will be written in a compact form using the Navier-Stokes operator:

$$\frac{\partial \mathbf{q}}{\partial t} = \mathcal{N}(\mathbf{q}) \tag{1.2}$$

with $\mathbf{q} = (\rho, \rho\mathbf{u}, \rho E)$ representing the state vector and $\mathcal{N}$ the non-linear Navier-Stokes operator.
Three different dimensionless parameters are also introduced:

$$Re = \frac{\rho_\infty U_\infty D}{\mu}, \quad M_\infty = \frac{U_\infty}{\sqrt{\gamma \frac{p_\infty}{\rho_\infty}}}, \quad St = \frac{fD}{U_\infty}. \tag{1.3}$$

These are the Reynolds, Mach, and Strouhal numbers, respectively. Quantities with the subscript $_\infty$ represent free-stream flow properties, D is the reference length, γ is the ratio of specific heats, and f is the characteristic frequency.

1.3 Phenomenology

Considering a generic cavity, without focusing too much (for now) on its geometric characteristics, we can depict a situation similar to that represented in the figure below (*Figure* 1.1):

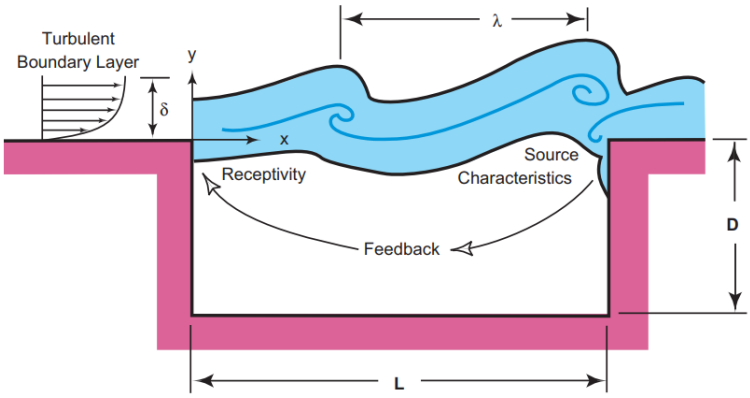

Figure 1.1: *Schematic representation of a cavity flow of length L and depth D, representing qualitatively the feedback mechanism, so the sensitivity of the flow in correspondence to the upstream edge to the acoustic waves coming from the downstream edge of the cavity. Picture taken from Cattafesta et al. [4].*

As the Reynolds number varies, different phenomena can occur. The flow, initially assumed to be parallel to the wall, experiences a forced separation point at the upstream edge of the cavity. As the Reynolds number increases past the threshold determining instability onset, the characteristic *shedding* phenomenon occurs. Additionally, the flow may fail to reattach to the wall after passing the downstream edge of the cavity, interacting with it instead. The oscillations generated by the interaction between the shear layer (caused by differing flow velocities in the cavity and the free stream) and the wall, especially at the reattachment point, produce acoustic noise in the form of pressure waves. These waves tend to propagate upstream, interacting with the hydrodynamic part of the flow (*receptivity*). The mechanisms governing noise generation are primarily four:

- amplification of disturbances by the shear layer
- shear layer-vortex interaction creating pressure waves
- acoustic wave feedback
- receptivity of the leading edge (pressure waves generate vorticity).

These combined mechanisms can result in a highly unsteady flow field characterized by discrete tones and background noise. This phenomenon is generally called the *Rossiter mechanism.*

In the classical view of cavity flows, from a dynamical systems perspective, the oscillations are referred to as *self-sustained oscillations* (Morris [5], Rowley and Williams [2]): an unstable equilibrium point exists such that small disturbances can cause continuous oscillation growth. In this case, it is necessary to consider

the existence of *non-linearities* that dampen these oscillations. Without considering non-linearities, the oscillations would continue to grow indefinitely. It is important to note that even if the disturbance ceases, the oscillations would continue to amplify.
The amplification is due to coupling between instabilities in the shear layer and the acoustic mode in the cavity depth direction.

A different perspective proposed by Rowley suggests the presence of *lightly damped* oscillations [6]. These oscillations tend to amplify background noise caused by incoming acoustic waves or boundary layer turbulence. In this case, removing the disturbance stops the amplification.

1.3.1 Kelvin-Helmholtz Instability and Shedding

The first mechanism typical of cavity flows is the Kelvin-Helmholtz instability, leading to what has previously been referred to as *shedding*.
To define this instability, it is necessary to briefly introduce the shear layer, prominently present in cavity flows.

The *shear layer* is a thin region with steep tangential velocity gradients, where vorticity is usually concentrated.

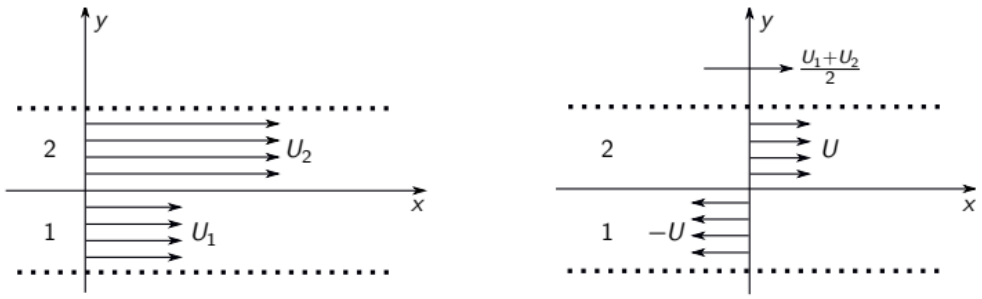

Figure 1.2: *Tangential velocity difference in shear flows. Shear flows are a typical flow configuration that appears when a steep velocity gradient is present between fluid layers. To simplify the problem represented on the left (where both U_1 an U_2 are present), it is a common procedure to shift the reference system so that the average velocity U is the only one needed.*

In cavity flows, this steep velocity gradient is particularly prominent at the leading edge. The flow, arriving at the cavity with the free-stream velocity of the undisturbed flow, encounters a relatively still flow inside the cavity. This significant velocity difference leads to the onset of the Kelvin-Helmholtz instability. For sufficiently high Reynolds numbers that make the *base flow* unstable, these vortical structures can amplify. The mechanism of periodic vortex shedding from the leading edge of the cavity corresponds to the shedding phenomenon.

1.4 Numerical analysis

Without numerical methods it would not be possible to obtain any results on a notably amount of mathematics problems. Citing one of the most important textbooks in this field, '*numerical analysis is the study of algorithms for problems in continuous mathematics*' (Trefethen and Bau [7]). Breaking down this definition, we get some of the main concepts of numerical analysis.
First of all, the concept of *algorithm* can be understood as a step-by-step process to get to a result. These processes are said by Trefethen to be used to solve *continuous mathematics*, so the part of mathematics that deals with real and complex numbers (as stated in the book) instead of purely integer values. The aim of numerical analysis is to get a result which is close enough to the exact solution of the problem. This is possible analyzing and using *numerical methods*.

1.4.1 DNS analysis

Coming to fluid dynamics, one of the most preferred techniques to solve the Navier-Stokes equations is the *Direct Numerical Simulation*. This method provides a complete three dimensional and time dependent solution of the N-S equations. As it is easy to understand, DNS need a sufficient computing power and efficiency to be implemented. Not too many years ago, quite a few flows could practically be studied using this technique, but technology is evolving at high rates, so that it is now easier to implement such computationally heavy numerical methods in CFD solvers.
In order to develop and use a powerful method such DNS, it is necessary to adopt some adjustments in the definition of the CFD simulation. First of all, for the direct numerical simulation to solve the exact flow equations every scale of the fluid domain should be resolved. Particularly when it comes to stability and turbulence, we are obliged to adopt a grid resolution which is sufficient to solve the eddies from the biggest to the smallest (Kolmogorov's) scale. This requirement is the main cause of the high computational cost of DNS, but it is also the reason why they are an unsurpassed technique to study turbulence.

In the works of this internship, DNSs are carried out to solve the fluid motion equations, particularly using the IC3 solver.

1.4.2 IC3

IC3 is a high order compact solver for the solution of the compressible Navier-Stokes equations developed from ISAE-SUPAERO. The IC3 solver implement different libraries in order to solve different fluid dynamics problems, spanning from shocks to stability using different numerical methods.
Concerning stability analysis, the originality of the IC3 solver is the possibility to run three dimensional global stability analysis (without imposing simplifications based on the flow's characteristics) on a quite vast selection of flows.
The code is still growing to implement different sophisticated numerical methods and solution techniques.

1.5 Stability Analysis

When discussing stability, it is necessary to first introduce the concept of *order*: a system is perceived as *ordered* if it exhibits certain symmetry properties. Stability is strongly tied to the idea of order, as it studies the conditions under which the system loses symmetry, also known as *bifurcation*.
The subject of stability is widely studied across various fields, not exclusively fluid dynamics. However, we will focus on this application for obvious reasons.

The concept of stability is linked to the presence of disturbances, which can enter the system with varying amplitudes. The following schematic is presented:

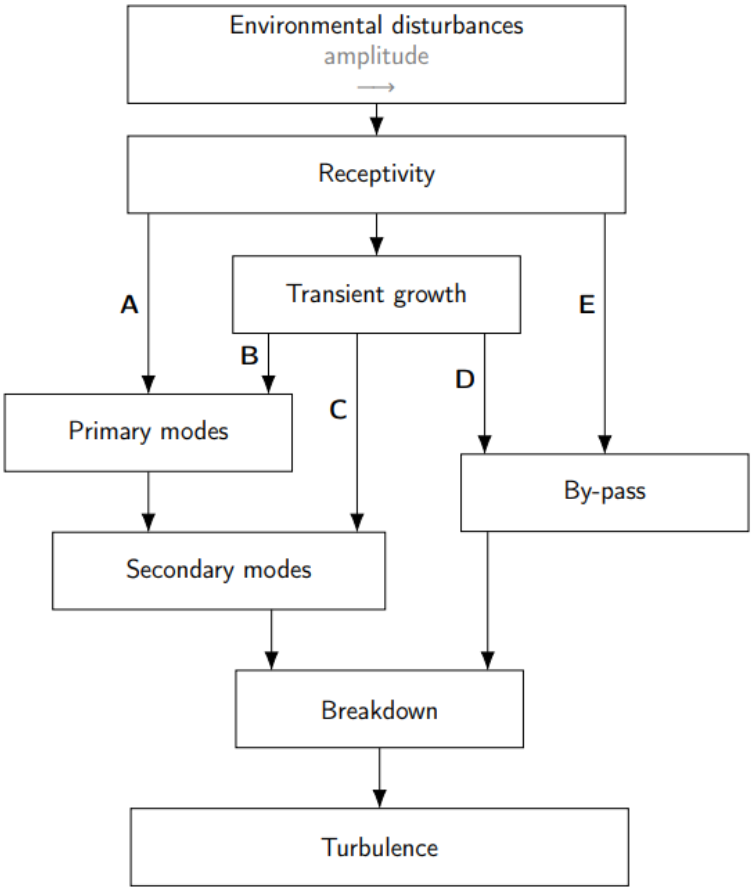

Figure 1.3: *Reference scheme representing the different behaviours of the flow when an increasing amplitude disturbance is applied to the flow. Going from left to right the disturbance's amplitude is growing leading to different modes and bifurcation in the flow. The scheme is taken from M.V. Morkovin [8].*

The diagram is read from left to right in terms of increasing disturbance amplitude (path A originates from small disturbances, path E from large ones). Depending on the system's characteristics, it may be more or less sensitive to disturbances, a property known as *receptivity*.
The following cases can then be distinguished:

- *Case A*: for small disturbances, the system may transition from stable to unstable through a primary bifurcation. The mode responsible for this bifurcation is

thus referred to as the *primary mode*. Subjecting the system to further perturbations of greater amplitude can result in additional bifurcations, called *secondary bifurcations*, caused by *secondary modes*. In typically two-dimensional systems, secondary modes lead to the flow becoming three-dimensional. An example of this phenomenon is schematically represented in the image below (*Figure 1.4*).

- *Case B*: here, the initial disturbance amplitude is larger, and the system experiences a transient growth of the disturbance, leading it back to Case A as previously shown.

- *Case C*: the disturbance amplitude is sufficient for the flow to bypass the primary bifurcation entirely, manifesting the secondary mode directly (*Figure 1.4*).

- *Cases D and E*: the disturbances are strong enough to bypass classical modes entirely and reach (whether or not preceded by transient growth) the stages leading to turbulence (*Figure 1.4*).

All these cases lead to a *breakdown* of structures that subsequently generates *turbulence*. In these latter phases, the connection to deterministic mathematics is lost, and statistical formulations become necessary. Stability focuses on the deterministic part of the problem.

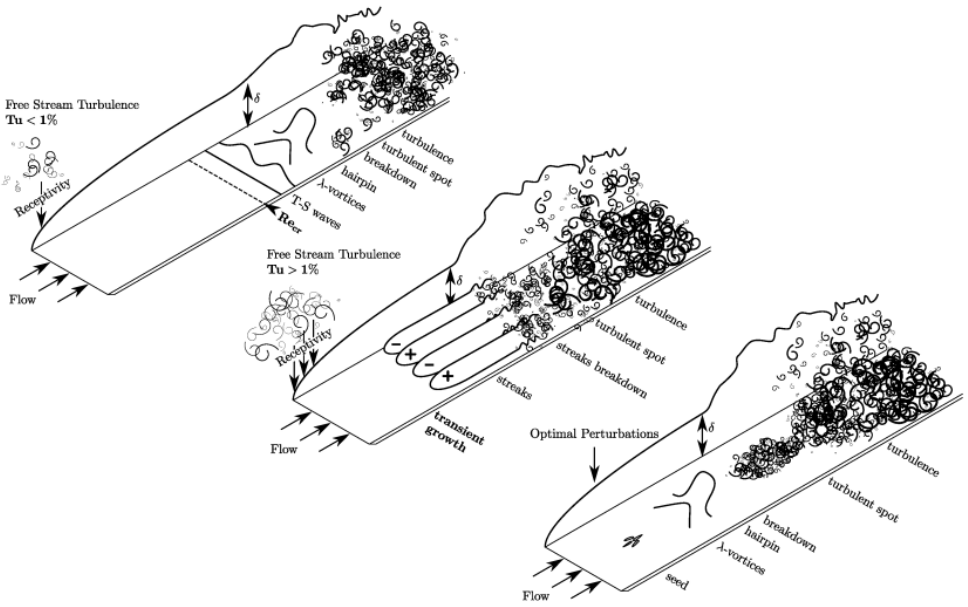

Figure 1.4: *Different cases explaining the concept of receptivity (sensitivity to the applied perturbations). The case A on top shows the behaviour of the flow when a small perturbation is applied: a first bifurcation (primary) causes the generation of a Tollmien-Schlichting wave, and increases until a secondary bifurcation brings three-dimensionality to the flow leading to breakdown; the case C in the middle shows the behaviour of the flow when the amplitude of the perturbation is sufficient to bypass the first bifurcation; case D on the bottom immediately manifest transient growth and turbulence. The picture is taken from Cherubini, Picella, and Robinet [9].*

Another example can be made by representing a cylinder of infinite length immersed in a fluid with varying Reynolds number (velocity in this case). Imagine increasing the Reynolds number; the first bifurcation occurs at $Re = 47$, determining the transition to the vortex shedding instability. Increasing the Reynolds number further, a second bifurcation occurs at $Re \simeq 10^2$, rendering the problem three-dimensional.

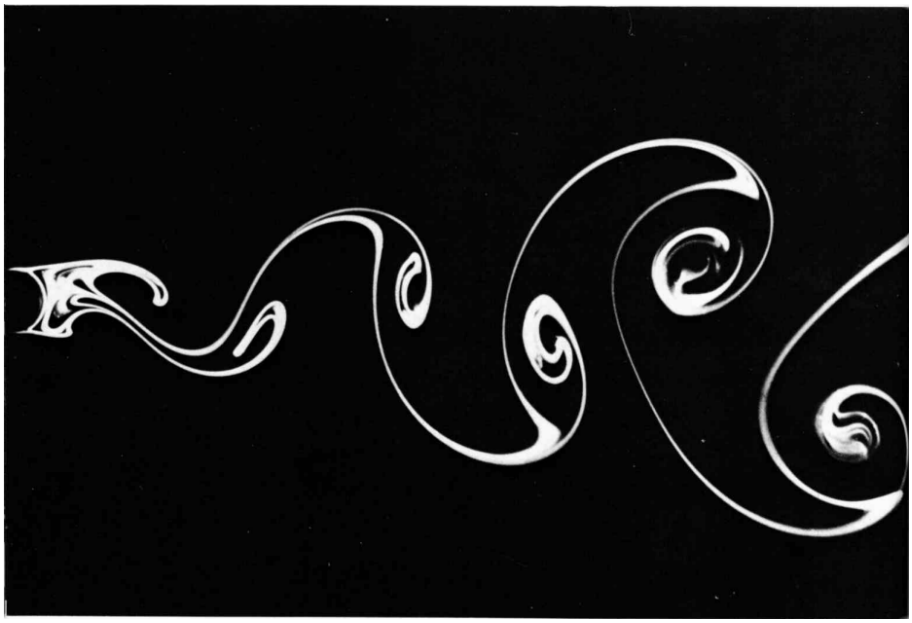

Figure 1.5: *Vortex shedding (primary mode) downstream of a cylinder. Considering an infinite length cylinder, this phenomenon happens exactly when the Reynolds number reaches the value of $Re = 47$. Picture taken from Van Dyke [10].*

Note that the shedding phenomenon is the one that will represent the first bifurcation also in the work presented, as it will be shown later in the report.

1.6 Internship goals

The aim of the internship and of this master thesis is to use the IC3 solver in order to execute a global stability analysis on a cavity flow while assuring the right boundary condition are applied without altering the results. Moreover the results are compared to a work published by Sun et al. in 2017 [11]. The ultimate goal is to implement different numerical methods and solution techniques in the IC3 solver while always assuring the validity of the results.

Chapter 2

Stability theory

2.1 Linear Stability Theory

To study flow instabilities and their transition to turbulence, one of the fundamental methods is *linear stability theory.*
Linear stability theory determines the stability of solutions of differential equations and trajectories of dynamical systems under the hypothesis of *small perturbations.* However, this study requires the definition of an *equilibrium point*, which will now be defined in more detail. Let us first distinguish the possible cases by introducing the following schematic:

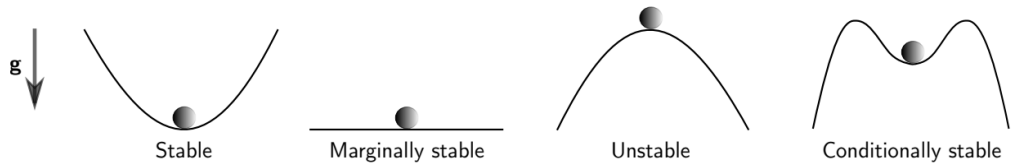

Figure 2.1: *Mechanics of a point particle. From left to right we can see the different configurations. Please note that using the linear stability theory applying small perturbations the 'conditionally stable' case cannot exist.*

A fundamental assumption of linear stability theory is that the amplitude of the perturbations is small. Specifically, considering ϵ as the perturbation amplitude, it is assumed that $\epsilon \ll 1$. Referring to the above schematic, the case of *conditionally stable* systems is excluded from linear stability theory, as significant perturbation amplitude is required for this to manifest.
The starting equations for linear stability theory are the dimensionless Navier-Stokes equations, here written for incompressible flows for the sake of simplicity:

$$\begin{cases} \frac{\partial \mathbf{u}}{\partial t} + \mathbf{u} \cdot \nabla \mathbf{u} = -\nabla p + \frac{1}{Re} \nabla^2 \mathbf{u} \\ \nabla \cdot \mathbf{u} = 0 \end{cases} \tag{2.1}$$

In compact form, this system can be written using the *Navier-Stokes operator* $\mathcal{N}$:

$$\frac{\partial \mathbf{q}}{\partial t} = \mathcal{N}(\mathbf{q}, \mathcal{C}) \tag{2.2}$$

where $\mathcal{C}$ is the *flow parameter vector* and $\mathbf{q}$ is the *state vector* (whose components

define the flow state):

$$\mathbf{q} = \begin{Bmatrix} \mathbf{u} \\ p \end{Bmatrix} \tag{2.3}$$

The equilibrium point around which perturbations are applied can now be defined. In linear stability theory, oscillations are considered relative to the *base flow*, which is the stationary solution of the Navier-Stokes problem. The base flow is defined by the state variable:

$$\mathbf{Q} = \begin{Bmatrix} \mathbf{U} \\ P \end{Bmatrix} \tag{2.4}$$

By definition, the base flow can be interpreted as:

$$\mathbf{Q} \equiv \mathbf{q} \ : \ \frac{\partial \mathbf{q}}{\partial t} = \mathcal{N}\left(\mathbf{q}, \mathcal{C}\right) = \mathbf{0} \tag{2.5}$$

Note: It is crucial to understand that linear stability is only possible when considering the base flow as a reference point around which perturbations act. This will now be deduced mathematically.

Using the definition of $\mathbf{Q}$, the flow can be decomposed as:

$$\mathbf{q} = \mathbf{Q} + \epsilon \mathbf{q}' \tag{2.6}$$

That is, as the sum of the base flow and a perturbation of amplitude $\epsilon \ll 1$.
Substituting this decomposition into the Navier-Stokes equations:

$$\begin{cases} \dfrac{\partial \mathbf{U}}{\partial t} + \epsilon \dfrac{\partial \mathbf{u}'}{\partial t} + \mathbf{U} \cdot \nabla \mathbf{U} + \mathbf{U} \cdot \nabla \epsilon \mathbf{u}' + \epsilon \mathbf{u}' \cdot \nabla \mathbf{U} + \epsilon \mathbf{u}' \cdot \nabla \epsilon \mathbf{u}' = \\ = -\nabla P - \nabla \epsilon p' + \dfrac{1}{Re} \nabla^2 \mathbf{U} + \dfrac{1}{Re} \nabla^2 \epsilon \mathbf{u}' \\ \nabla \cdot \mathbf{U} + \nabla \cdot \epsilon \mathbf{u}' = 0 \end{cases} \tag{2.7}$$

Recalling the components of the state vector, we observe that within the equations:

$$\begin{cases} \frac{\partial \mathbf{U}}{\partial t} + \mathbf{U} \cdot \nabla \mathbf{U} = -\nabla P + \frac{1}{Re} \nabla^2 \mathbf{U} \\ \nabla \cdot \mathbf{U} = 0 \end{cases} \tag{2.8}$$

These are solutions of the Navier-Stokes equations by definition and can therefore be eliminated from the perturbed system. Among the remaining terms, the non-linear terms are very small (and thus negligible), leaving only the linear terms proportional to the perturbation amplitude ϵ:

$$\begin{cases} \dfrac{\partial \mathbf{u}'}{\partial t} + \mathbf{U} \cdot \nabla \mathbf{u}' + \mathbf{u}' \cdot \nabla \mathbf{U} = -\nabla p' + \dfrac{1}{Re} \nabla^2 \mathbf{u}' \\ \nabla \cdot \mathbf{u}' = 0 \end{cases} \tag{2.9}$$

Thus, it has been demonstrated that, in linear stability theory, the base flow is essential (as it is a solution of the Navier-Stokes equations), and the perturbation amplitude need not be large (as long as $\epsilon \ll 1$).
In compact form, this can be written as:

$$\frac{\partial \mathbf{q}'}{\partial t} = \mathcal{L}\left(\mathbf{Q}, \mathcal{C}\right) \mathbf{q}' \tag{2.10}$$

Where $\mathcal{L}$ is the Jacobian of the Navier-Stokes operator:

$$\mathcal{L} = \left(\frac{\partial \mathcal{N}}{\partial \mathbf{q}}\right)_{\mathbf{q}=\mathbf{Q}} \tag{2.11}$$

Note that no assumptions about the form of the perturbation have been made up to this point.
It is crucial to recognize that near the base state $\mathbf{Q}$, the dynamics of the perturbation can be studied using the dynamics of the linearized system.

2.2 Base Flow characteristics

Based on the spatial and temporal properties of the base flow, some assumptions and simplifications can be considered.

2.2.1 Modal and Non-Modal Analysis

Concerning the *temporal* properties of the base flow, two cases can be distinguished:

- For $\mathbf{Q} = \mathbf{Q}(\mathbf{x})$ stationary and considered a fixed point, a *Modal Analysis* is performed. In this case, the perturbation can be represented as a linear superposition of exponential perturbations with time dependence:

$$\begin{aligned}
\mathbf{q}'(\mathbf{x},t) &= \sum_{j=1}^{\infty} \hat{\mathbf{q}}_j(\mathbf{x}) e^{\omega_j t} + \text{c.c.} \\
&= \sum_{j=1}^{\infty} \hat{\mathbf{q}}_j(\mathbf{x}) e^{[\Re(\omega_j)+i\Im(\omega_j)]t} + \text{c.c.} \\
&= \sum_{j=1}^{\infty} \hat{\mathbf{q}}_j(\mathbf{x}) e^{\Re(\omega_j)t} \left[cos(\Im(\omega_j)t) + isin(\Im(\omega_j)t)\right] + \text{c.c.}
\end{aligned} \tag{2.12}$$

  where ω_j is the complex frequency of the perturbation. Its real part $\Re(\omega_j)$ corresponds to the *growth rate* of the perturbation (indicating whether the perturbation is amplified $\Re(\omega_j) > 0$ or damped $\Re(\omega_j) < 0$), and its imaginary part corresponds to its frequency ($\Im(\omega_j) = 2\pi f_j$ pulsation of the perturbation). Note that, since the perturbations are linearly independent, considering the asymptotic behavior as $t \to \infty$, the flow dynamics will be determined by the perturbation with the largest $\Re(\omega_j)$, i.e., the most amplified (or least damped) mode.
  Substituting the perturbation form 2.12 into the compact system 2.10, the following relation is obtained:

$$\frac{\partial \hat{\mathbf{q}}_j(\mathbf{x}) e^{\omega_j t}}{\partial t} = \mathcal{L}\hat{\mathbf{q}}_j(\mathbf{x}) e^{\omega_j t} \tag{2.13}$$

  Performing the time derivative and simplifying the exponential:

$$\omega_j \hat{\mathbf{q}}_j(\mathbf{x}) = \mathcal{L}\hat{\mathbf{q}}_j(\mathbf{x}) \tag{2.14}$$

This corresponds to an eigenvalue problem (EVP) in the eigenvalues ω_j and eigenvectors $\hat{\mathbf{q}}_j(\mathbf{x})$ of the operator $\mathcal{L}$. Consequently, conducting a modal analysis corresponds to performing a spectral analysis of the linear operator.

- For $\mathbf{Q} = \mathbf{Q}(\mathbf{x}, t)$ time-dependent, a *Non-Modal Analysis* is performed.
  In this case, the base flow is non-stationary, and the perturbation is no longer assumed to have an exponential form:

$$\mathbf{q}' = \mathbf{q}'(x, t) = \sum_{j=1}^{\infty} \hat{\mathbf{q}}_j(\mathbf{x}, t) + \text{c.c.} \tag{2.15}$$

  Here, the perturbation cannot be considered as a linear superposition of independent perturbations. Non-modal analysis thus exhibits transient growth depending on individual perturbations. However, the asymptotic behaviour for $t \to \infty$ still reflects the least stable mode of the system.

  In the present work, a *modal analysis* is conducted.

2.2.2 Local and Global Approaches

Depending on the *spatial* properties of the base flow, the type of stability analysis changes.
Specifically, based on the spatial symmetries of the flow, there may be one or more directions of *homogeneity*, and it can be assumed that the perturbation evolves as a Fourier series along these directions:

- For $\mathbf{Q} = \mathbf{Q}(x_1, t)$, where x_2 and x_3 are directions of homogeneity, a *Local Approach* is used:

$$\mathbf{q}' = \hat{\mathbf{q}}(x_1, t) e^{[i(\alpha x_2 + \beta x_3)]} + \text{c.c.} \tag{2.16}$$

- For $\mathbf{Q} = \mathbf{Q}(x_1, x_2, t)$, where x_3 is the direction of homogeneity, a *Bi-Global Approach* is used:

$$\mathbf{q}' = \hat{\mathbf{q}}(x_1, x_2, t) e^{(i\alpha x_3)} + \text{c.c.} \tag{2.17}$$

- For $\mathbf{Q} = \mathbf{Q}(x_1, x_2, x_3, t)$ with no directions of homogeneity, a *(Tri-)Global Approach* is used:

$$\mathbf{q}' = \mathbf{q}'(x_1, x_2, x_3, t) = \mathbf{q}'(\mathbf{x}, t) \tag{2.18}$$

Here, α and β are the real wave numbers in the x_2 and x_3 directions, respectively. If the form of the perturbation (2.12) is substituted into the spatial evolution system using the local or bi-global approach, a simplified eigenvalue problem arises, where the eigenvalues ω_j depend on the wave number:

$$\begin{cases} \omega_j = \omega_j(\alpha) & \text{in the case of local analysis} \\ \omega_j = \omega_j(\alpha, \beta) & \text{in the case of bi-global analysis} \end{cases} \tag{2.19}$$

These are called *dispersion relations*.
For tri-global analysis, it is often referred to as *Global Stability Theory*.
In this case, no directions of homogeneity exist, meaning the spatial evolution of the base flow cannot be assumed a priori and therefore the dispersion relation loses its

value.
In this thesis, a *global* approach is used, even if it is considered interesting to go back to a fictitious local approach to determine the dispersion relation.
The stable/unstable nature of the base flow $\mathbf{Q}$ is determined by the spectral properties of the linear operator $\mathcal{L}$, following this criteria:

- The base state is said to be *globally stable* if $\Re(\omega_j) < 0 \ \forall \ j \in \mathbb{N}$. In this scenario the perturbations are damped in time and the perturbed flow will always go back to its initial equilibrium state;
- The base state is considered *globally unstable* if $\Re(\omega_j) > 0$ at least for a value of j. It means that there will be at least one perturbation that will grow in time making the flow diverging from its original equilibrium state. It is not said within this criteria if the flow will indefinitely diverge or if it will converge to a different equilibrium state;
- The base state is *marginally stable* if the leading eigenvalue satisfies $\Re(\omega_j) = 0$. When this happens, the perturbation is neither damped or amplified.

2.3 Local approach

Even if the analysis that is executed in the work of this master thesis belongs to the branch of *global stability analysis*, the local approach deserves some interest, as it gives us the knowledge to step up to the more general case.
We consider from now on a base flow $\mathbf{Q} = \mathbf{Q}(x_1, t)$ with x_2 and x_3 homogeneous directions:

$$\mathbf{q}'(\mathbf{x}, t) = \hat{\mathbf{q}}(x_1, t) e^{[i(\alpha x_2 + \beta x_3)]} e^{\omega t} + \text{c.c.} \tag{2.20}$$

2.3.1 Spatial and Temporal Theory

For flows where only one variable is independent in the equations (e.g., Poiseuille flow), i.e., using a local stability approach, two different analyses can be conducted: if the amplification/damping of the perturbation is considered in space, it is called a *spatial approach*, whereas if the perturbation evolves over time, a *temporal approach* is used. Starting from the local stability equation (2.16):

$$\mathbf{q}'(\mathbf{x}, t) = \sum_{j=1}^{\infty} \hat{\mathbf{q}}_j(x_1) e^{i(\alpha x_2 + \beta x_3)} e^{\omega t} + \text{c.c.} \tag{2.21}$$

For the sake of simplicity and without losing generality, a two-dimensional flow is considered (the dependence on x_3 is lost):

$$\mathbf{q}'(\mathbf{x}, t) = \sum_{j=1}^{\infty} \hat{\mathbf{q}}_j(x_1) e^{i(\alpha x_2)} e^{\omega t} + \text{c.c.} \tag{2.22}$$

1. In *Temporal Theory*, $\alpha \in \mathbb{R}$ and $\omega \in \mathbb{C}$:

$$\begin{aligned} \mathbf{q}'(\mathbf{x}, t) &= \sum_{j=1}^{\infty} \hat{\mathbf{q}}_j(x_1) e^{i\alpha x_2} e^{\omega_j t} + \text{c.c.} \\ &= \hat{\mathbf{q}}_j(x_1) \left[cos(\alpha x_2) + isin(\alpha x_2) \right] e^{\Re(\omega_j)t} \ldots \\ &\quad \ldots \left[cos(\Im(\omega_j)t) + isin(\Im(\omega_j)t) \right] + \text{c.c.} \end{aligned} \tag{2.23}$$

The dominant term is thus the exponential, which governs the decay and amplification of perturbations:

- $\Re(\omega_j) < 0 \quad \Rightarrow$ the disturbance is damped over time $\quad \Rightarrow$ **stable**
- $\Re(\omega_j) = 0 \quad \Rightarrow$ it neither increases nor decreases $\quad \Rightarrow$ **neutral**
- $\Re(\omega_j) > 0 \quad \Rightarrow$ the disturbance is amplified over time $\quad \Rightarrow$ **unstable**

The disturbance can be considered as a wave packet resulting from the superposition of periodic waves along the x_2 direction, with a wavelength $\lambda = \frac{2\pi}{\alpha}$. Each wave follows the exponential term, decaying/growing over time with a *growth/decay rate* determined by $\Re(\omega_j)$ and has a *phase velocity* $v_\phi = \frac{\Im(\omega_j)}{\alpha}$. In cases where all waves have the same phase velocity, the medium is referred to as *non-dispersive*. It is also possible to define the velocity of the wave packet, the *group velocity*, as $v_g = \frac{d(\Im(\omega_j))}{d\alpha}$.

2. In *Spatial Analysis*, $\alpha \in \mathbb{C}$ and $\omega \in \mathbb{R}$:

$$\begin{aligned} \mathbf{q}'(\mathbf{x},t) &= \sum_{j=1}^{\infty} \hat{\mathbf{q}}_j(x_1) e^{i\alpha_j x_2} e^{\omega t} + \text{c.c.} \\ &= \hat{\mathbf{q}}_j(x_1) \left[cos(\Re(\alpha_j)x_2) + isin(\Re(\alpha_j)x_2)\right] e^{-\Im(\alpha_j)x_2} ... \\ &\quad ... \left[cos(\omega t) + isin(\omega t)\right] + \text{c.c.} \end{aligned} \tag{2.24}$$

Similarly to the temporal case, the exponential term governs the system:

- $\Im(\alpha_j) < 0 \quad \Rightarrow$ the disturbance is amplified in space $\quad \Rightarrow$ **unstable**
- $\Im(\alpha_j) = 0 \quad \Rightarrow$ it neither increases nor decreases $\quad \Rightarrow$ **neutral**
- $\Im(\alpha_j) > 0 \quad \Rightarrow$ the disturbance is damped in space $\quad \Rightarrow$ **stable**

To perform a comprehensive and non-simplified analysis, it would be necessary to use both approaches. It is not always possible to know in advance which method is more appropriate, and using only one of them might not adequately describe the flow.

2.3.2 Dispersion relation and phase velocity

While studying hydrodynamic stability by using a local approach and the temporal theory it is possible to consider the wave as a superposition of perturbation waves, as in 2.23. Anytime a wave is moving inside a specific medium, it is possible to define a *dispersion relation*, that is, a mathematical expression that links the pulsation of the wave with its wave number based on the characteristics of the base flow and of the transmission medium.
The dispersion relation is usually represented by the mathematical expression:

$$\mathfrak{F}(\alpha, \omega, \mathbf{Q}, \mathcal{C}) = 0 \tag{2.25}$$

And it is the output of a local stability analysis eigenvalue problem, or from a different point of view, the existence of an eigenfunction constrains α and ω to satisfy this relation. Usually the aim of the dispersion relation is to define:

$$\omega = \omega(\alpha) \tag{2.26}$$

So, as previously said, the pulsation of the wave as a function of the wave number. From this expression it is possible to define the physical medium as *dispersive* or *non-dispersive*. In a dispersive medium, waves with different wavelengths (wave numbers) propagates with different speeds, so that the wave packet sees a distortion while it propagates ($v_\phi \neq v_g$). On the contrary, in a non-dispersive medium the single waves' speed is the same as the packet speed ($v_\phi = v_g$), so that the wave packet propagates without any distortion.

In order to better understand the concept, it is necessary to define the *phase speed*:

$$v_\phi = \frac{\Im(\omega)}{\alpha} \tag{2.27}$$

Where $\Im(\omega) = 2\pi f$ is the angular pulsation and α the real wave number. Note that the same definition would still be appropriate if both ω and α were complex, thus considering the real part of the wave number $\alpha_r = \frac{2\pi}{\lambda}$ (the streamwise wave number) in 2.27.

Once the phase velocity is defined, it is possible to obtain the *group velocity*:

$$v_g = \frac{\partial \Im(\omega)}{\partial \alpha} \tag{2.28}$$

From its definition, it is obvious that $v_\phi = v_g$ when $\Im(\omega) = \Im(\omega(\alpha))$ is linear.

2.4 Global approach

The majority of open flows is characterized by a certain loss of homogeneity and symmetry of the flow. In cases where the three dimensionality of the flow dynamics is not negligible any more, it is necessary to improve the techniques to run stability analyses. The global approach then considers a base flow $\mathbf{U}(\mathbf{x}, t)$ without spatial symmetries and so does for the perturbations. Also, as the term itself suggests, global stability analysis considers the changes in the base flow in the whole fluid domain. As written in paragraph 2.2.2 the perturbation is described by:

$$\mathbf{q}'(\mathbf{x}, t) = \hat{\mathbf{q}}(x_1, x_2, x_3)e^{\omega t}\,. \tag{2.29}$$

The global stability analysis using a modal approach is based on finding the solution to the eigenvalue problem:

$$\omega_j \hat{\mathbf{q}}_j(\mathbf{x}) = \mathcal{L}\hat{\mathbf{q}}_j(\mathbf{x}) \tag{2.30}$$

which admit a solution when the determinant $(\mathcal{L} - \omega_j \mathbf{I})$ is zero. That is the aim of the future analyses.

2.4.1 Primary and secondary instabilities

In *Paragraph* 1.5 the concept of receptivity was introduced, which is an indicator of the influence of a system to external disturbances. Usually the receptivity relies on the influence of certain parameters on the system.

For the sake of the explanation, let's consider a cylinder of infinite length invested by the flow (*Figure* 2.2). The evolution of the flow behind a cylinder has been widely studied in the past, so that there is quasi-perfect knowledge of the phenomena involved. It is perfectly known the response of the fluid at changes of the Reynolds number, which is the parameter that controls this type of fluid configuration.
Starting from $Re \simeq 0$, the flow is perfectly attached to the cylinder's surface. Increasing the Reynolds number until $Re \simeq 5$ is reached, the flow begins to manifest two steady counter-rotating vortices behind the cylinder, creating a recirculation bubble. This situation is recognized to be the first appearance of a convective instability. Increasing the Reynolds number a first local absolute instability occurs, even if the convective instability still dominates the dynamics of the flow. However, when the Reynolds number reaches the value of $Re \simeq 47 = Re_{cr_1}$, the absolute instabilities are large enough to make the flow globally unstable. The instabilities develop as a series of swirling vortices periodically detaching the cylinder's surface. This mechanism is the self-sustained von Karman vortex-sheet, which corresponds to the so called *primary instability* of the system. As anticipated in 1.5 the primary modes rarely alter the spatial symmetries of the flow, which still remains bi-dimensional.
Each time a periodic phenomena develops (making the flow unstable), it is said that a *bifurcation* has occurred. A bifurcation occurs each time an equilibrium state is left to reach another one, not necessarily stable.
Reaching $Re \simeq 180 = Re_{cr_2}$, the wake behind the cylinder becomes three-dimensional, and a second bifurcation occurs. Usually many different types of secondary bifurcation may occur, but within the scope of this work we will spend a few words on the primary bifurcation, which will be the only one evidently occurring.

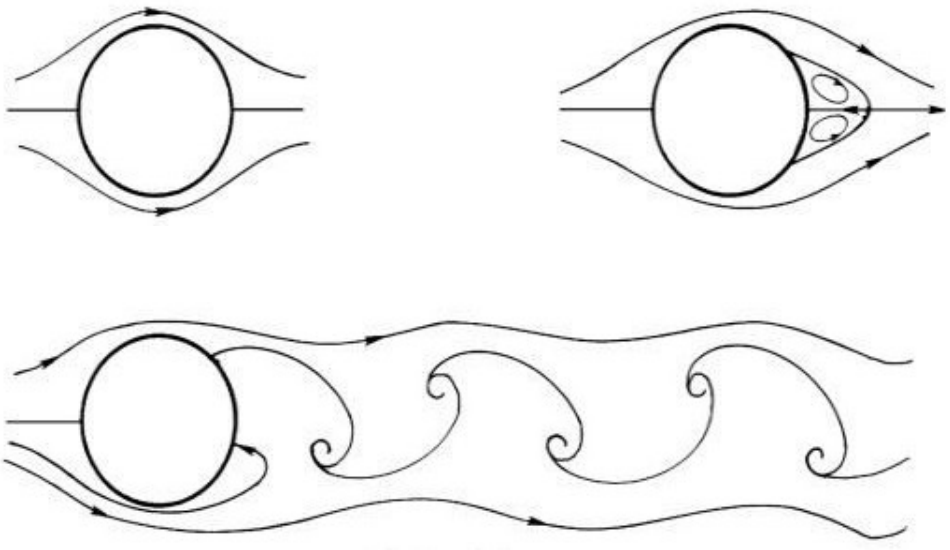

Figure 2.2: *Wake behind an infinite cylinder changing the control parameter Re: for $Re < 5$ the flow is perfectly attached to the cylinder's surface (upper left); increasing the Reynolds number up to $Re = 25$ a local absolute instability appears behind the cylinder (upper right). Given that the instabilities are still small, the convective instability still dominates the wake. After having reached the Re_{cr_1} the von Karman mechanism occurs, resulting in swirling vortices periodically detaching from the cylinder's surface. Scheme adapted from Kundu et al. [12].*

2.4.2 Primary instability and bifurcations

Without losing generality, we may affirm that whenever a control parameter varies we expect some changes in the configuration of the flow. As well as for the cylinder, many other flow have the same behaviour while changing the Reynolds number: when $Re < Re_{cr_1}$ the solution is stationary, when $Re_{cr_1} < Re < Re_{cr_2}$ the solution becomes periodic and a von Karman vortex sheet appears, and for $Re > Re_{cr_2}$ a secondary bifurcation leading to a three-dimensional evolution of the flow occurs. The two critic values Re_{cr_1} and Re_{cr_2} act as limits to two different equilibrium states, which are generally referred to as *attractors*. The name is a consequence of the fact that the dynamics of neighbouring initial state will converge towards them as $t \to \infty$. Please note that the two attractors are two equilibrium states for the flow, so they are stable solutions, also referred to as *fixed points*. Fixed points can also be represented in the phase space $(\mathbf{q}, \dot{\mathbf{q}})$, as shown in *Figure* 2.3.

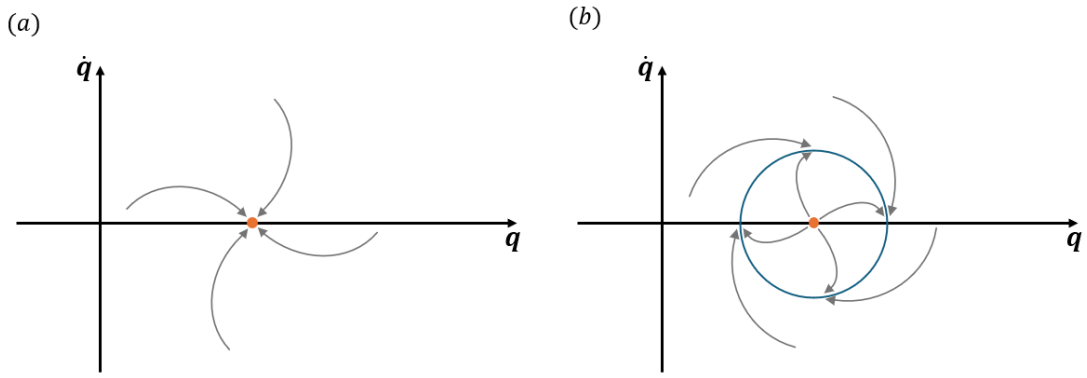

Figure 2.3: *Representation on the phase space of the attractors. In (a) the stable fixed point is represented ($Re < Re_{cr_1}$ with the solutions converging towards it. Case (b) ($Re_{cr_1} < Re < Re_{cr_2}$) represents the stationary solution represented as the orange dot is unstable, and the system evolve towards another stable limit cycle (represented in blue) which is the periodic solution. Scheme adapted from Rolandi [13].*

When a stable fixed point sees a transition towards a limit cycle (defined by the appearance of a periodic solution), the bifurcation goes by the name of *Hopf bifurcation* (*Figure* 2.4).

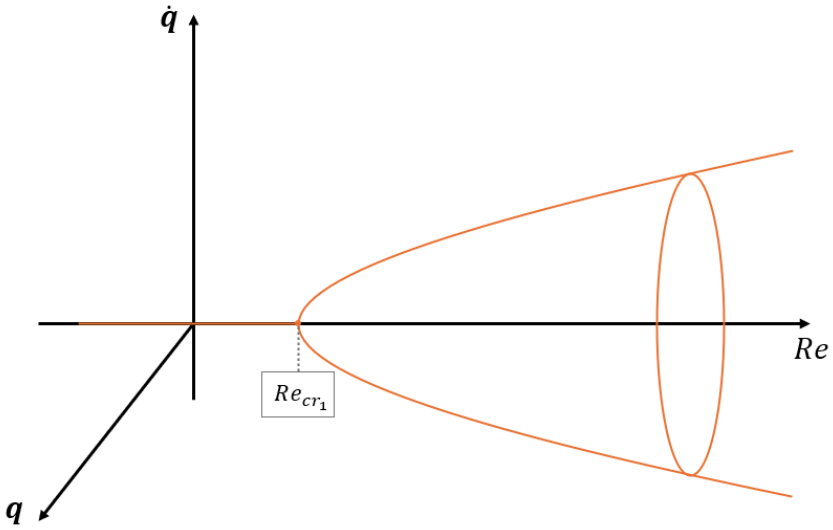

Figure 2.4: *Schematic representation of an Hopf bifurcation in the phase space. The Hopf bifurcation occurs whenever a stable fixed point tends towards a periodic solution when the values of Re_{cr_1} is reached. Please note that if we took a slice of the graph at a fixed Reynolds number we would obtain what is represented in Figure 2.3. In particular, considering $Re < Re_{cr_1}$ we would obtain Figure 2.3 case (a), while slicing for $Re > Re_{cr_2}$ would give us Figure 2.3 case (b). Scheme adapted from Rolandi [13].*

Basically Hopf bifurcation is associated to the most amplified eigenvalue of the Jacobian matrix $\mathcal{L}$ which crosses the real axis at $Re = Re_{cr_1}$

2.4.3 Limit cycle instabilities

In order to understand how the IC3 solver solves the global stability analysis eigenvalue problem, it is necessary to introduce the Floquet theory, which is useful to study linear differential equations with time-periodic coefficients. Following the explanation of Charru [14] and Rolandi [13], we can define a periodic linear operator $\mathcal{L}(t) = \mathcal{L}(t + T)$ where T is the oscillation period. In this case the equation 2.10 becomes:

$$\frac{\partial \mathbf{q}'}{\partial t} = \mathcal{L}(t)\mathbf{q}' \tag{2.31}$$

The Floquet analysis is based on the study of the limit cycle using the so called *Poincaré section*. The concept is to consider an arbitrary Poincaré section Σ which intersects with the periodic orbit, and to store a single point of the trajectory for each cycle of motion (*Figure* 2.5). The points collected on Σ define the *Poincaré map*, whose evolution gives valuable informations about the stability of the system.

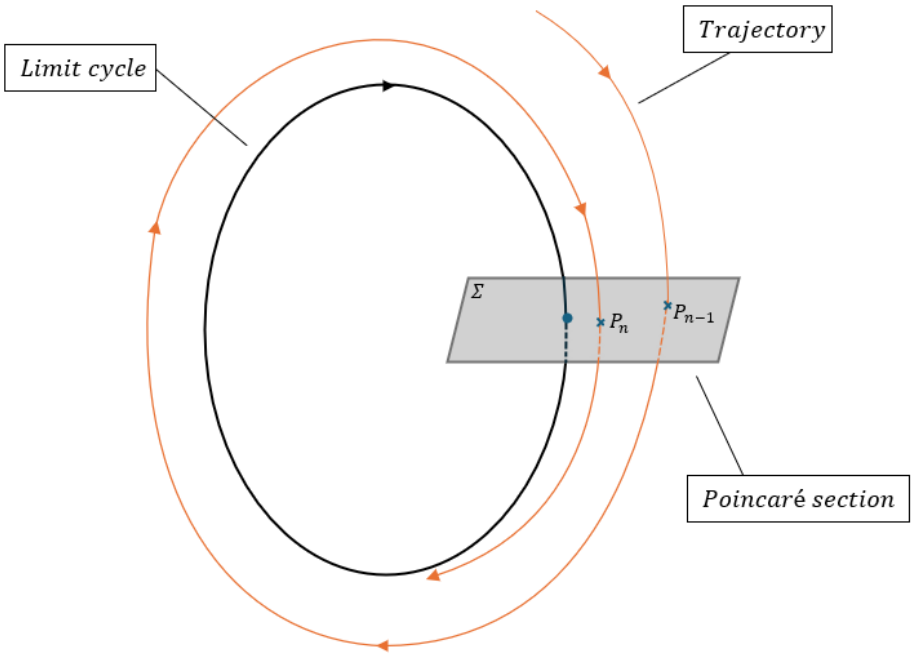

Figure 2.5: *Schematic representation of the Poincaré map. The orange trajectory intersects with the Poincaré section Σ each cycle of motion. The blue point represents the intersection between the limit cycle and the Poincaré section. Scheme adapted from Rolandi [13].*

Mathematically speaking, we can introduce the *Floquet transition matrix* $\phi(0,T)$ which relates the states of the systems at the times $t=0$ and $t=T$ so that:

$$\mathbf{q}'(T) = \phi(0,T)\ \mathbf{q}'(0) \tag{2.32}$$

This expression is similar to the analytical solution of 2.10 when an initial condition at $t=0$ is applied:

$$\mathbf{q}'(t) = e^{\mathcal{L}t}\mathbf{q}'(0) \tag{2.33}$$

We can observe that $\phi(0,T) = e^{\mathcal{L}T}$. The eigenvalues of the Floquet transition matrix ϕ are usually called *Floquet multipliers* μ. It is usual connotation to define the *exponential propagator matrix* $\mathcal{M} = e^{\mathcal{L}T}$.
The Floquet multipliers μ, which are the eigenvalues of the exponential propagator matrix, and the eigenvalues of the Jacobian matrix $\mathcal{L}$ are evidently correlated by the relation:

$$\mu = e^{\omega T} \tag{2.34}$$

In conclusion, the stability of each mode can be deduced either from the real part of ω or the modulus of μ:

$$\begin{cases} \omega_r < 0 \text{ or } |\mu| < 1 \ \Rightarrow \ \text{the flow is stable} \\ \omega_r > 0 \text{ or } |\mu| > 1 \ \Rightarrow \ \text{the flow is unstable} \end{cases} \tag{2.35}$$

The IC3 solver finds the eigenvalues of the propagator matrix and determines the Jacobian matrix's eigenvalue from them.

2.4.4 Resolution of the EV problem

It should be clear at this point that the global stability analysis considers a perturbation in the form:

$$\mathbf{q}' = \hat{\mathbf{q}} e^{\omega t} \text{ with } \hat{\mathbf{q}} = \left[\hat{\rho}, \hat{\rho u}, \hat{\rho E}\right]^T \tag{2.36}$$

The perturbation acts around the base state $\mathbf{Q}$ following the already told equation:

$$\frac{\partial \mathbf{q}'}{\partial t} = \mathcal{L}\mathbf{q}' \tag{2.37}$$

Where $\mathcal{L} = \left(\frac{\partial \mathcal{N}(\mathbf{q})}{\partial \mathbf{q}}\right)_{\mathbf{Q}}$ is the Jacobian matrix of the Navier-Stokes operator determined at the base state. Solving the eigenproblem means to find the spectrum of $\mathcal{L}$: in order to analyse the flow stability the main goal is to study the most amplified mode that states the asymptotic behaviour of the perturbation.
Given that determining explicitly the Jacobian matrix could result in a very expensive calculation, it is common to apply *matrix-free* approaches where the Jacobian matrix's coefficients are determined evaluating matrix-vector products. There are multiple matrix free approaches in literature, but the one that is implemented in IC3 (and then briefly explained in this chapter) is the *Krylov-Schur method* (Hernandez, Roman, and Vidal [15], Stewart [16]). As every Krylov projection method, its aim is to determine an approximation of the most relevant eigenvalues (hence eigenvectors) of a matrix.
Basically the Krylov-Schur method solves a generic eigenproblem:

$$A\mathbf{x} = \lambda\mathbf{x} \tag{2.38}$$

considering a subspace $\mathfrak{K}_m$ of dimension m, which is created from the $n \times n$ matrix A and a vector $\mathbf{b}$ of length n:

$$\mathfrak{K}_m(A, \mathbf{b}) = span\{\mathbf{b}, A\mathbf{b}, A^2\mathbf{b}, ..., A^{m-1}\mathbf{b}\} \tag{2.39}$$

Where $\{\mathbf{b}, A\mathbf{b}, A^2\mathbf{b}, ..., A^{m-1}\mathbf{b}\}$ is usually called *Krylov sequence*. Under certain particular assumptions, the Krylov sequence converges towards the eigenvector associated with the most amplified mode as the subspace dimension $m \to \infty$.
The Krylov-Schur method is a method that implements iteratively the *Arnoldi algorithm*, which is very shortly presented in the next paragraph without going into the details.

2.4.5 Arnoldi algorithm and Krylov Schur method

The Arnoldi algorithm simplifies the eigenproblem $A\mathbf{x} = \lambda\mathbf{x}$ by approximating the eigenvalues and eigenvectors of A with those of a reduced matrix (the Hessenberg matrix, which is a matrix with zero entries under the first subdiagonal) and evaluating the residuals in order to check convergence.

$$AV_m = V_m H + residuals \tag{2.40}$$

where A is the large matrix to approximate, V_m is an orthonormal basis (such that $V_m^T V_m = I$) and H is the Hessenberg matrix.
Usually the Arnoldi algorithm can be applied when a small number of eigenvalues is

required, otherwise the reduced matrix become too large and too computationally difficult to compute. Here comes the Krylov-Schur algorithm [17], that uses iteratively the Arnoldi factorization implementing a truncation mechanism that reduces the matrix size.
If k eigenvalues are needed, the Krylov subspace dimension m is fixed so that $m > k$. The Arnoldi factorization is then applied for the m dimensioned subspace.
Once the factorization is completed, the subspace is reduced to the k dimension, where k represents the 'wanted' eigenpairs (the ones with the largest module eigenvalues). The remaining $m - k$ 'unwanted' eigenpairs are reordered and truncated. The dimension of the matrix is then smaller then before, and the Arnoldi algorithm can be applied again on the k dimensioned subspace. The iteration stops when a certain tolerance is reached by the Arnoldi residual.
A scheme for the Krylov-Schur method is represented in *Figure* 2.6:

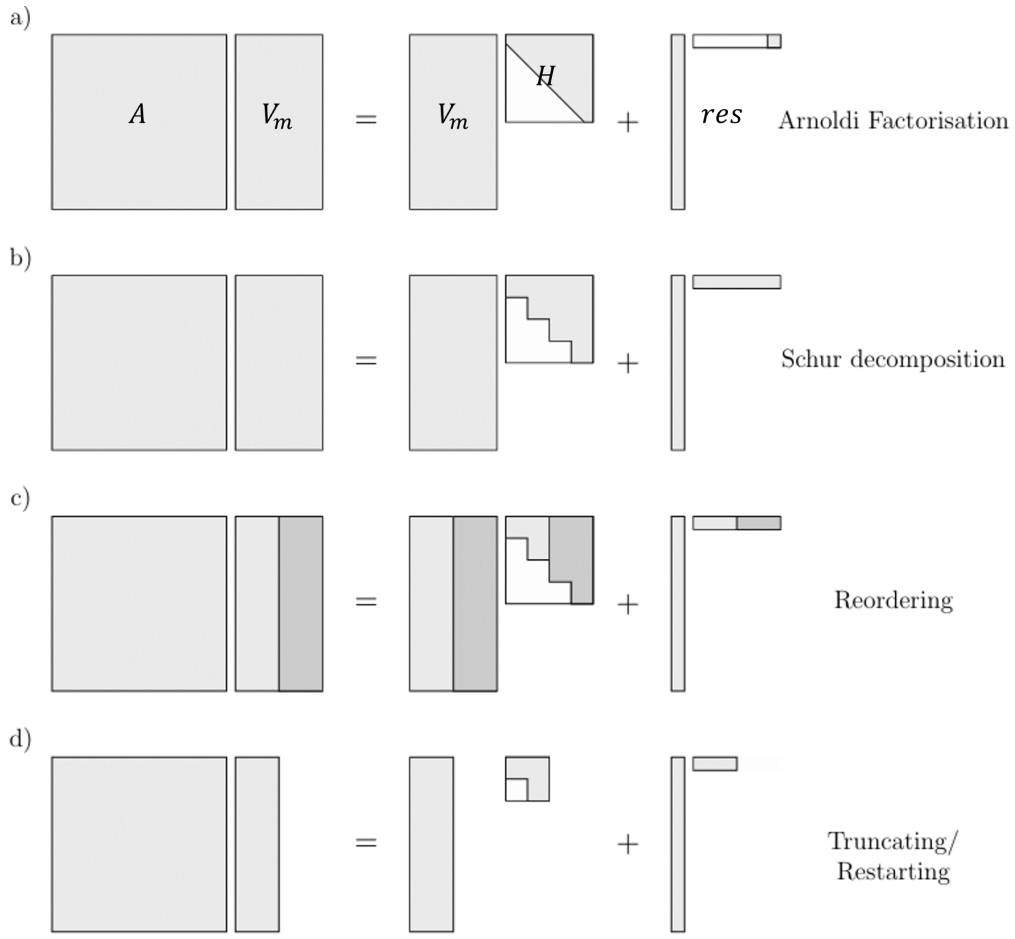

Figure 2.6: *Scheme representing the Krylov-Schur method. The dimension of the Krylov subspace m is chosen such that if k is the number of eigenvalue needed, $m > k$. The Arnoldi factorisation is executed on the subspace to create the Hessenberg reduced matrix (a); then the 'wanted' and 'unwanted' eigenpairs are identified (b) and reordered (c); the truncation of the unwanted eigenpairs diminishes the dimension of the subspace, making it easier to apply again the Arnoldi algorithm if not enough eigenvalues have converged. Scheme adapted from Rolandi [13].*

2.4.6 Implementation in IC3

We have seen how, using the Arnoldi and Krylov-Schur algorithm, it is possible to determine the eigenvalues of a large scale matrix (the Jacobian matrix in our case) using only matrix-vector products. This brings us to the matrix free formulation used in the IC3 solver, which is the *time-stepping exponential transformation.*

We consider the analytic solution of 2.30, already showed in 2.33:

$$\mathbf{q}'(\tau) = \mathcal{M}\mathbf{q}'(0) \tag{2.41}$$

where the propagator $\mathcal{M} = e^{\mathcal{L}\tau}$. The Arnoldi algorithm can be applied to the propagator $\mathcal{M}$ instead of the Jacobian matrix $\mathcal{L}$, where the matrix-vector product $\mathcal{M}\mathbf{q}'$ corresponds to the perturbation at a certain time $t = \tau$.
The Chiba method is used as described by CHIBA [18] Tezuka and Suzuki [19], so that:

$$\mathcal{M}\mathbf{q}' = \frac{\mathbf{q}_+^\tau - \mathbf{q}_-^\tau}{2\epsilon} \tag{2.42}$$

where $\mathbf{q}_+^\tau$ and $\mathbf{q}_+^\tau$ correspond to the DNS solutions corresponding to the initial conditions $(\mathbf{Q} + \epsilon\mathbf{q}')$ and $(\mathbf{Q} - \epsilon\mathbf{q}')$ integrated until τ. Applying the Krylov-Schur method on the approximation of $\mathcal{M}\mathbf{q}'$ it is possible to determine the eigenpairs $(\mu, \hat{\mathbf{q}}_\mathcal{M})$.
At this point the eigenpairs of $\mathcal{L}$ $(\omega, \hat{\mathbf{q}}_\mathcal{L})$ can be obtained inverting the exponential relation between $\mathcal{L}$ and $\mathcal{M}$:

$$\omega = \frac{log|\mu| + i\ arg(\mu)}{\tau}\,. \tag{2.43}$$

Chapter 3

Numerical stability methods and parametric influences on open cavity flows

This chapter aims to provide a clearer framework for the analyses carried out during my time at ISAE-SUPAERO by offering additional context on the various methods available for conducting stability studies. Moreover, it highlights the key parameters that must be considered when performing these analyses.

3.1 Numerical methods for stability analyses

The first part of this chapter is focused on the different methodologies adopted to perform stability analyses. The present is just an overview based on the review written by Taira et al. [20].
As previously said, we know that we can apply two different approaches:

- The *modal analysis* is used to determine the asymptotic behaviour of the base flow. By determining different modes, we can consider the perturbations as their superposition and determine whether each mode is amplified or damped. This study, which is basically a spectral analysis of the Navier-Stokes operator, does not give a very complete overview of the flow' s behaviour, given that the transient is not considered.

- The *non-modal analysis* let us determine the transient growth of the perturbations. This analysis has much more physical sense as an asymptotically stable base flow may become turbulent during the transient growth.

The importance of transient growth studies is a consequence of the non-normality of the Navier-Stokes operator. The characteristic of *non-normal* operators is that their eigenvectors are non-orthogonal, resulting in what is showed in *Figure* 3.1. If we consider two eigenvectors ϕ_1 and ϕ_2 and we do the difference between them, vector f is obtained. By decreasing ϕ_1 and ϕ_2's lengths the resulting difference vector f tends to align to the direction of ϕ_1 and to increase its norm. This mechanism, that happens only when a non-normal operator is involved, determines a transient growth of the perturbations in the short time, and it is the reason why it is useful to execute a non-modal analysis when it comes to hydrodynamic stability.

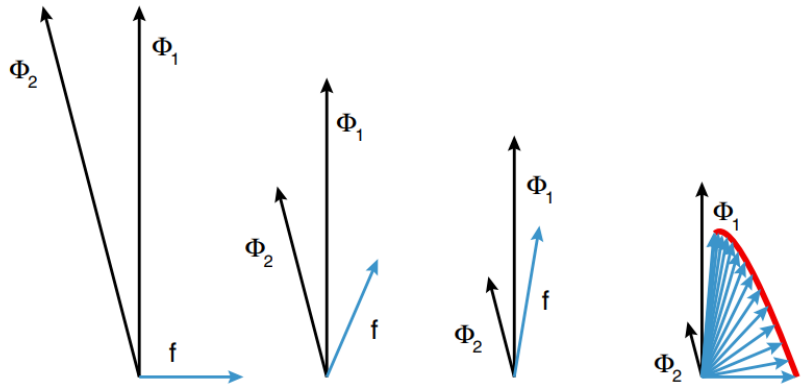

Figure 3.1: *Figure representing two non-orthogonal vectors ϕ_1 and ϕ_2. In the picture, the vector f represents the difference between ϕ_1 and ϕ_2. When the lengths of ϕ_1 and ϕ_2 decrease differently during the iterations, the difference vector f tends to align to the direction of ϕ_1 while increasing its length. The result is that the superposition of non-orthogonal eigenfunctions can produce in the short term a growth of the perturbation's norm. This would not happen in the case of two orthogonal vectors where the difference vector f would decrease in length as ϕ_1 and ϕ_2 shrink. The picture is taken from Schmid [21].*

3.1.1 Modal analysis

This thesis work is focused on the realization of a modal analysis on a cavity flow using the linear stability theory. This methodology will be fully explained in the next chapters.
In general, many different approaches to modal analysis exist. The modal decomposition is based on the extrapolation of the most energetic and dynamically important features of different flows (modes), and mainly two frameworks have been developed to do so (Taira et al. [20]):

1. When we use the flow field data as input of the modal analysis we can refer to *data-based techniques*;

2. When the analysis is based on discrete operators that derive from the Navier-Stokes equations we are referring to *operator-based techniques*.

Whatever it is the chosen technique, the modal analysis is based on the determination of the eigenvectors having the eigenvalue with the largest magnitude. This is possible using the Eigenvalue and Singular Value Decomposition (EVD and SVD respectively), two methods that are used to reduce matrices' dimensions and extrapolate the eigenvectors. The reader is addressed to Taira et al. [20] for a deeper understanding of these two methods. The main difference between them is the working matrix's size: the eigenvalue decomposition works on square matrices, while the singular value decomposition works on rectangular matrices. Both extrapolate the eigenvectors and eigenvalues with the largest magnitude, but while the SVD always works, the EVD can be applied only in certain cases. The EVD convenience is the computational cost, a lot smaller than that of the SVD.
Starting from the data-based techniques, we introduce the following: the *Proper Orthogonal Decomposition* (POD), the *Balanced POD* (BPOD), and the *Dynamic Mode Decomposition* (DMD).

The POD provides an algorithm that decompose the data field into modes to capture the flow features containing high energy. Using as input a snapshot of any scalar or vector field $\mathbf{q}(\mathbf{x}, t)$, the POD determine as output a set of modes $\phi_j(\mathbf{x})$, their corresponding temporal coefficients $a_j(t)$ and the energy levels identified by λ_j. The modes are given in order of their amount of energy. The POD, whose algorithm is showed in details in Taira et al. [20], is mainly used because of the low amount of data needed to represent the flow field and its fast convergence properties. Moreover, its output is a set of basis vectors with the minimal dimensions, making it a useful method to create reduced order models. However, the modes that the POD method identifies are arranged in order of energy content but not dynamical relevance in the flow, so it is possible to miss some important flow dynamics.

This last issue is covered using the Balance POD (BPOD). This method can determine two different sets of modes, one based on the inputs (for example external disturbances), one focused on the desired outputs. It is said that BPOD balances the properties of *controllability* and *observability*. The first property defines the features that are most excited by the inputs, while the second one refers to the modes that give the largest outputs. When we say that BPOD balances these two properties the meaning is that this method determines a coordinate system where the most controllable directions are also the most observable [20].
The two sets of modes are called *balancing modes* and *adjoint modes*, and they are ranked by controllability and observability. The adjoint system solved using this method will be better explained when non-modal analysis is presented. For now it is sufficient to know that the study of the adjoint system makes the BPOD a useful tool to study transient growth and to create input-output model that can be used to control the perturbations.
On the contrary, the need for the snapshots from the adjoint simulations makes it difficult to adopt the BPOD on experimental measurements.

The last data-based technique is the Dynamic Mode Decomposition (DMD), that decomposes time-resolved data into modes, each represented by a characteristic frequency of oscillation and a growth/decay rate. Specifically, the decomposition is applied to a best-fit linear operator that corresponds to an approximation of the flow' s dynamics. Without going into details, instead of calculating the eigenvalues λ_j of the operator $\mathbf{A}$, the eigenvalues μ_j of the best fit linear operator $\tilde{\mathbf{A}}$ are determined, and the relation between them is:

$$\lambda_j = \frac{1}{\Delta t} log(\mu_j) \tag{3.1}$$

At this point the frequencies and the growth rates of the DMD modes can be obtained observing the real and imaginary parts of λ_j.
DMD's advantage is that it is possible to examine separately the different flow dynamics without making any a priori assumptions on them. The downside of this method is that the obtained modes are not ranked by relevance, so it may be difficult to decide which mode is important or not. Moreover, DMD may not be accurate when non-linear systems are considered.

Now that the data-based techniques have been shortly introduced, the same is done

for the operator-based methods. The focus here is put on the operator that describes the flow dynamics. The methods presented here are the *Koopman analysis*, the *global linear stability theory* and the *resolvent analysis*.

Koopman analysis is capable of giving a set of modes and a set of eigenfunctions of a non-linear dynamical system examining a linear, infinite-dimensional operator (called Koopman operator). The observability of the eigenfunctions produced by the method makes it a powerful tool for control techniques. A few more words can be found on Taira et al. [20].

About the global linear stability theory just a few words are spent here. Solving the eigenvalue problem gives us informations on the spectrum of the linearized Navier-Stokes for large times, so when $t \to \infty$. It is possible to adopt different methods to determine the spectrum of the Jacobian matrix (the linear operator) of the Navier-Stokes equations. The one used in this thesis is the *matrix-based approach*: the eigenvalue problem is solved by storing the matrices on memory. If the matrix is small in size, it is possible to determine it directly, while if the Jacobian matrix becomes too large to calculate, matrix-free approaches are implemented (the Krylov-Schur algorithm based on the Arnoldi method is one example).
A different approach is the *time stepping approach* where the Jacobian matrix is not directly determined. Further knowledge can be found in the review from Theofilis [22].
While the global stability analysis is a very powerful tool for determining the spectrum of eigenmodes, it is very important to remember that it has its limits: it needs as the base flow an exact solution of the N-S equations, and it is of course linear.

The Resolvent analysis is a completion of the global linear stability analysis, given that it gives the possibility to add external forcing to the equations, basically neglecting the hypothesis of small perturbations. The study focuses on the determination of the maximum amplification of the forcing and how the non-linear forcing itself relates to the velocity and pressure perturbations. The method gives in output the most amplified inputs or forcing modes.
The resolvent analysis can be applied using the mean flow as base state, even in the case of turbulent flows. Moreover, when turbulent flows are studied, the resolvent analysis considers the large coherent structures as modal solutions forced by a turbulent background. The downside of this method is that informations about the forcing term are required.

3.1.2 Non-modal analysis

It was said that evaluating the asymptotic behaviour of the flow may be a strong approximation of the flows' dynamics. While the modal analysis works in the assumption of normal-modes (making it possible to consider an exponential time dependence), it is important to remember that the Navier-Stokes operator is non-normal, making the short term evolution non-negligible. The time-asymptotic characteristics of the flow and the shape of the least stable mode could be irrelevant under real conditions. For example, the Couette flow studied using modal analysis appears to be stable for all Reynolds numbers, while we know from experiments that it is

unstable also for relatively low Reynolds.
In conclusion, the short term behaviour cannot be neglected.
As described by Schmid [21], the evolution of infinitesimal perturbations is influenced by the governing parameters (as for the asymptotic analysis), by the initial conditions and by the external forcing. In general two different approaches can be considered: the flow response to initial conditions and that to external forcing. Looking into the first approach, this is mostly interested in determining the instabilities in the flow, while the second approach is related to sensitivity analysis (and control theory).
Whenever the non-modal stability analysis is executed, it is important to choose an appropriate measure of the disturbance size. The most convenient choice is the energy E, with an appropriate integration weight.

The response to initial conditions is the first approach shortly described here. Considering the kinetic energy as the quantity to check, the aim of this approach is to find its maximum amplification when the initial conditions change. Schmid [21] defines the amplification factor as:

$$G(t) = \underset{\mathbf{q}_0}{max} \frac{||\mathbf{q}(t)||^2}{||\mathbf{q}_0||^2} \tag{3.2}$$

Evaluating the response to initial conditions, it is considered $t \to 0^+$.
It is then needed a quantity that describes the behaviour at this time, which is the *numerical abscissa*, defined as:

$$\underset{\mathbf{q}}{max} \frac{1}{||\mathbf{q}||^2} \left(\frac{d||\mathbf{q}||^2}{dt} \right)_{t=0^+} \tag{3.3}$$

The details are showed in Schmid [21]. The meaning of the numerical abscissa is the maximum protrusion in the unstable half-plane (the maximum energy growth at $t \to 0^+$).
One last quantity can be defined to evaluate the maximum energy amplification over time: as said in the review written by Schmid [21], the resolvent analysis (explained before) can be used to define the *Kreiss constant*, which is a lower estimate of the maximum extension in the unstable half-plane of the resolvent contours (obtained by evaluating its norm).
Using a picture also showed in Schmid [21] for the Poiseuille flow at $Re = 1000$ and $\alpha = 1$, we visualize the eigenspectrum in *Figure* 3.2.
In the picture the blue dots represent the eigenvalues of the asymptotic time. Please note that these point are located in the stable half plane. However, the red line representing the numerical abscissa and the black dot representing the Kreiss constant are located in the unstable half-plane, meaning that during the transient growth the flow is unstable.
It is a direct consequence of this transient growth behaviour of the perturbations that also the neutral curve will change for this flow, as showed in *Figure* 3.2, taken from Schmid [21] as well. It is important to highlight that in normal systems the critic Reynolds for transient growth and for asymptotic growth of the perturbations would coincide.

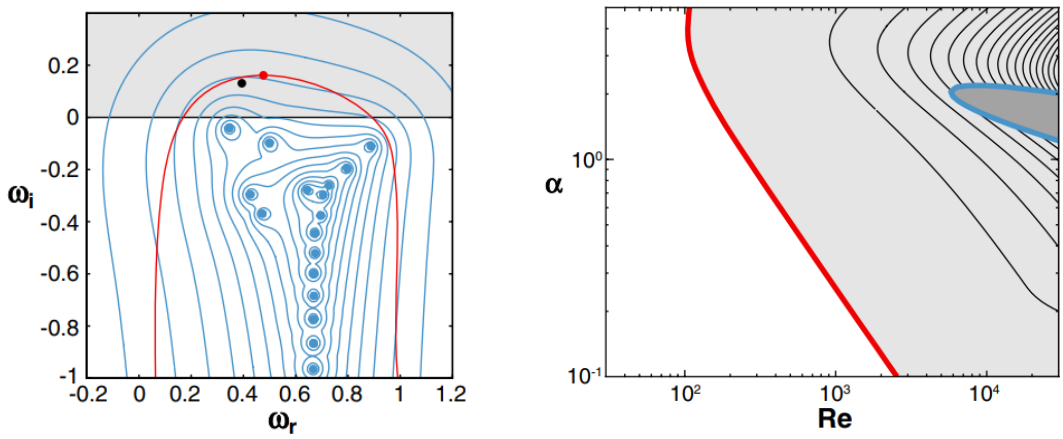

Figure 3.2: *Figures taken from Schmid [21]. (Left): a 2D Poiseuille flow at* $Re = 1000$ *and* $\alpha = 1$ *is studied using non-modal analysis. The blue lines are the contours of the resolvent, while the blue dots represent the asymptotic eigenvalues. As it can be seen, the eigenvalues are in the stable half-plane, so asymptotically this flow would result in a stable flow. However, the red line representing the numerical abscissa and the black dot representing the Kreiss constant are located in the unstable half-plane, meaning that during the transient growth the flow is unstable. (Right): neutral curve for the flow studied. We can distinguish a dark grey zone of the map (delimited with a blue curve) representing the unstable region in the asymptotic limit. The light-grey region is asymptotically stable, but sees a transient growth in the short term. In conclusion, the white region is the only one where the flow is always stable.*

The second approach that is considered in non-modal analysis is the response to external forcing. In the model considered by Schmid [21], the general solution of the Navier-Stokes equations sees the homogeneous solution, which represents the response to initial conditions, and the particular solutions which brings informations about the sensitivity to external forcing. In a similar fashion to what is done for the analysis of the response to initial conditions, it is possible to define a parameter for the maximum response to external forcing, namely $R(\omega)$ using Schmid notation, so that:

$$R(\omega) = \max_{\mathbf{q}_{in}} \frac{||\mathbf{q}_{out}(t)||^2}{||\mathbf{q}_{in}||^2} \tag{3.4}$$

where $\mathbf{q}_{in}$ represent the input forcing, $\mathbf{q}_{out}$ the output response, and ω the forcing frequency.
Many different methods exist to study the flow impulse response or the resonance frequency of the flow with external perturbations. The one we focus in this short paragraph, is the adjoint method.

As stated in the review from Luchini and Bottaro [23], the adjoint equations were first formulated to help reducing the order of any ordinary differential equation. They then became a useful tool to determine the sensitivity of global quantities (named *objective*) at the same computational cost of solving the direct problem.
The adjoint analysis is one of the three common methods to solve the stability of open flows, alternatively to full numerical simulations of the linearized/non-linear problem and quasi-parallel approximations of the linearized problem. The advantage of adjoint analysis is that compared to the others it permits to execute a parametric study of the perturbations.

The aim is to determine where and how it is possible to modify the flow structure in order to produce a great shifting of the unstable eigenvalues in the eigenspectrum obtained with the direct analysis. As told by Luchini and Bottaro [23] it is possible to identify a region in space where the oscillation is self-sustained and from which the instabilities are propagated to the rest of the flow: this region is called *wave maker*. This is the region where we desire to insert a control mechanism that alters the flow making it stable.

3.2 Influence of control parameters

Now that different methods adopted to execute stability analyses have been shortly introduced, it is important to focus on the control parameters that influence the flows' dynamics. We can identify the following:

- Perturbation's location;
- Perturbation's frequency;
- Mach number;
- Reynolds number;
- Boundary layer thickness;
- Aspect ratio.

Presenting different scientific articles and papers, the effect that these parameters have on the flow stability is discussed.

3.2.1 Influence of the perturbation's location

The perturbation's position is related to the definition of the optimal perturbation. This is very closely linked also to the sensitivity and receptivity study that has been introduced speaking of the non-modal analysis and adjoint method, given that it represents the basis of control theories.
Different studies have been conducted on open cavities looking for the optimal perturbation and identifying the most sensitive regions when a disturbance (or external forcing) is applied. We bring here the study conducted by Citro et al. [24] analysing the global modes of a square cavity and executing the sensitivity analysis in order to find the wavemaker and the best position for the initial perturbation.
The cavity studied in the scientific paper is schematically represented in *Figure* 3.3. The boundary conditions applied are of non-slip wall in the upstream, downstream and cavity surfaces, of velocity inlet for the inflow and stress-free condition for the outflow. The base flow is considered 2D, while the perturbation applied is three-dimensional. Symmetry b.c. are applied to the sides as the base flow is obtained.

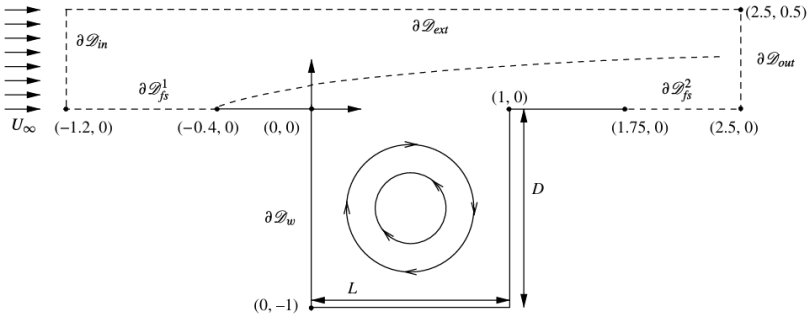

Figure 3.3: *Domain used by Citro et al. [24]. The square cavity is considered two-dimensional for the base flow determination, while the applied perturbation is three-dimensional. The applied boundary conditions are of non-slip wall at the upstream, downstream and cavity surfaces; the inflow applies a velocity inlet b.c. while at the outflow a stress-free condition is applied.*

In the paper a global stability analysis is conducted to determine the unstable two-dimensional modes and the first bifurcation for a flow at $Re = 4140$. As the different modes are obtained, the sensitivity analysis is executed on the most amplified one. The sensitivity analysis is obtained determining the product of the direct and adjoint fields. By plotting both the direct and adjoint eigenfunctions of the unstable modes found from the stability analysis, it is discovered that the point most receptive to external forcing is the leading edge of the cavity. By positioning the perturbation here, the instability is most efficiently triggered. For a graphic validation of what said, the contour plots of the absolute value of the direct and adjoint eigenfunctions of the four unstable modes are taken from Citro et al. [24] and represented in *Figure* 3.4.

In order to determine the wavemaker, it is necessary to determine the critic Reynolds and the first mode that becomes unstable. In Citro et al. [24] this mode correspond to a wavenumber $\alpha = 13.4$ and at the critic Reynolds $Re = 1370$. In this conditions it is possible to plot the sensitivity and observe the regions in the flow where a perturbation most alters the eigenvalue of this mode. What is determined in the study is that the wavemaker corresponds to a region inside the cavity, in particular to the closed streamline around the main vortex. Moreover, from this study it appears that the regions above the cavity (characterised by a strong shear) give a negligible contribute to the sensitivity. In *Figure* 3.5 the wavemaker identified by Citro et al. [24] is showed.

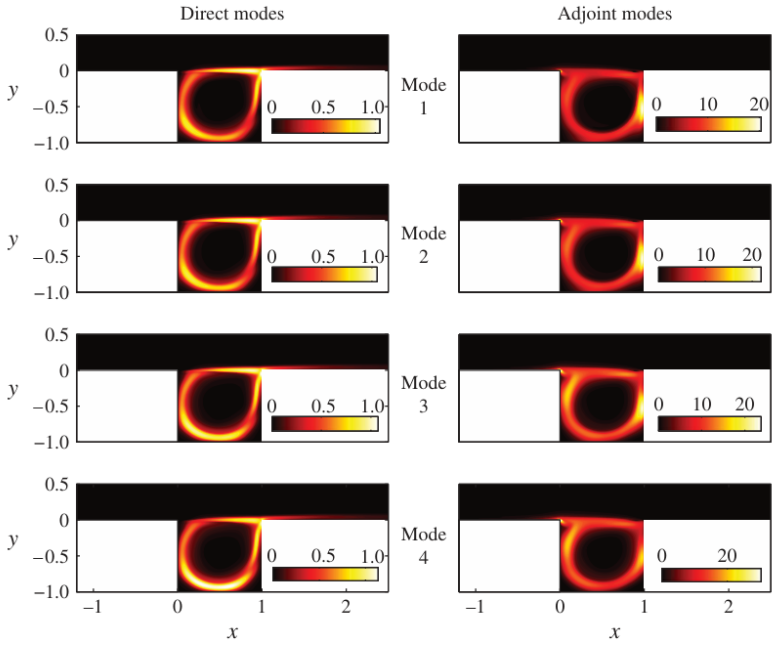

Figure 3.4: *Picture taken from Citro et al. [24]. The absolute value of the direct and adjoint eigenfunctions of the four unstable modes identified by the stability analysis are depicted here. From the adjoint fields we can see that the leading edge of the cavity is the most receptive to external forcing, so the instabilities are most efficiently triggered in this point.*

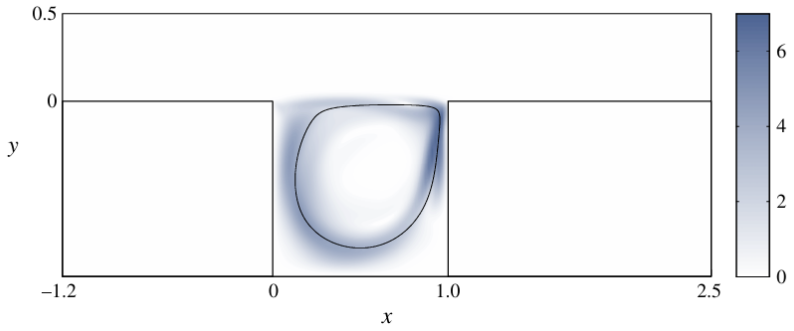

Figure 3.5: *Image taken from Citro et al. [24]. The sensitivity of the unstable mode identified by* $\alpha = 13.4$ *at* $Re = 1370$ *is showed. From the sensitivity calculation (the product of the direct and adjoint mode) it is possible to determine the regions of the flow where the perturbation most alters the eigenvalue. This region is also defined by Citro as the 'wavemaker', and for an open cavity flow it appears to be a closed streamline around the main vortex, and it is not influenced by the strong shear of the regions above.*

Summarizing, from the results shown in the paper by Citro et al. [24] we get the following informations:

- Perturbations in the free-stream do not influence the flow inside the cavity and on the cavity edges, which are the regions where the instabilities are triggered;
- A perturbation in the upstream, leading edge of the cavity most alters the flow stability. In the scenario of non-modal stability analysis, it is convenient to perturb the flow here to have the maximum effect on the instabilities;

- The region most triggered by the perturbations and where the perturbations are self-sustained (the wavemaker) is a closed streamline inside the cavity around the main vortex and is not influenced by the shear regions above. In the scenario where a control method has to be designed, it is reasonable to study this region.

From these informations the adjoint analysis also permits to think of control mechanism like suction and/or blowing to control the instabilities.

3.2.2 Influence of the perturbation's frequency

When a modal stability analysis is executed, it is not mandatory to define the initial perturbation frequency, given that we are only interested in the asymptotic limit looking for the dominant mode that will characterise the flow. In this thesis, for example, the perturbation is introduced as numerical perturbation inside the boundary layer, without imposing a pre-determined frequency to the initial perturbation. The modal analysis consists in the resolution of the eigenvalue problem, and from the study of the eigenvalues the natural frequencies of the dominant eigenmodes.
However, there are three scenarios where a well defined initial perturbation (meaning, its frequency) has to be applied to the base flow:

1. To examine the evolution of a modal mode;
2. To insert a forcing term;
3. To optimize a control mechanism.

In the first case it is quite obvious that we first need to define the base flow, then to determine the most amplified/least stable eigenmodes from the modal analysis, and to use the frequencies of the dominant modes (or the one whose evolution we want to track) as initial perturbations. In this way, executing a direct numerical simulation, we can evaluate the perturbation's evolution.
If we are forcing the system applying an external perturbation, then it is common practice to execute a resolvent analysis. A few words about this method have already been spent, but we refer to the article by Sun et al. [25], where a resolvent analysis is used to identify the flow response to external forcing on an open cavity flow with $\frac{L}{D} = 6$ at $Re = 502$ and $M = 0.6$, exactly the case studied in this thesis work. The resolvent analysis consists 'simply' on applying an external forcing to the governing equation for the perturbation, so that:

$$\frac{\partial \mathbf{q}'}{\partial t} = \tilde{L}(\overline{\mathbf{q}})\mathbf{q}' + \mathbf{f}' \tag{3.5}$$

where $\tilde{L}(\overline{\mathbf{q}})$ correspond to the Navier-Stokes linear operator, $\mathbf{q}'$ is the perturbation and $\mathbf{f}'$ the forcing term. Without going into details (explained in [25]) a new operator is defined, which is the *resolvent operator*. While studying the resolvent operator two set of modes can be found, called *response modes* and *forcing modes*. The link between these two is the *resolvent gain*, that basically defines the response to the external forcing. The gains are meant as energy norms, so that the higher the gain is, the higher the energy contained in the mode is. It is then possible to find the

frequencies related to the highest energy content of the modes. This way we can use the resolvent analysis to create initial perturbation that force a certain response in the system.
The same concept is used to design control methods, which is the third item that needs the initial perturbation's characteristics to give valuable results.

3.2.3 Influence of the Mach number

In this section we aim to give knowledge about the flow response when the Mach number is varied, specifically going from low Mach numbers (considering almost incompressible flows) to transonic and supersonic flows.
Different articles and research papers explore this topic, so we present here a short review of the most interesting results obtained.
Given the similar case study, we bring here the results obtained by Sun et al. [26] where different cavity geometries are studied for a Mach number range going from 0.1 to 1.4. First a global stability analysis is executed to determine the global instabilities on a 2D flow. Further details about the analyses can be found in [26]. It is interesting to examine the influence of Mach number on the case $\frac{L}{D} = 6$, which is the same aspect ratio studied in this thesis work. The Reynolds number is determined using the boundary layer momentum thickness as reference length, in particular the results in the paper are showed for $Re_\theta = 19$. Using the results obtained using IC3, the Reynolds number rescaled using the momentum thickness would be $Re_\theta = 21.4$, so we can consider the two cases comparable. Using the images proposed by Sun et al. [26], we can observe in *Figure* 3.6 the numerical schlieren, instantaneous vorticity contours and time averaged streamlines of the case studied. Please note that the average flow seems to change a lot with the Mach number, and apparently this behaviours differs from open cavity with a smaller aspect ratio. For low Mach numbers the shear layer mode dominates, generating a vortex close to the trailing edge of the cavity. Increasing the Mach number the instantaneous vorticity shows an even stronger oscillation of the flow, so we expect the flow to be more unstable. It is interesting that when we are close to a transonic regime, the flow gets more stable, and as the Mach number reaches $M = 1.2$ the instabilities disappear making the flow steady again.
As also reported by Mathias and Medeiros [27] the increasing effects of compressibility tend to enhance instabilities at first and stabilizing the flow for higher Mach values.
As it was said, this behaviour slightly differs from the one seen in cavities with smaller aspect ratios. Even though the general trend is the same, the stabilizing effect of compressibility at higher Mach numbers is greater for cavities with higher $\frac{L}{D}$ ratio. The explanation given by Sun et al. [26] is that the longer the cavity is, the higher is the possibility for the shear layer to amplify disturbances, making the stabilizing effect of compressibility at transonic Mach more evident.

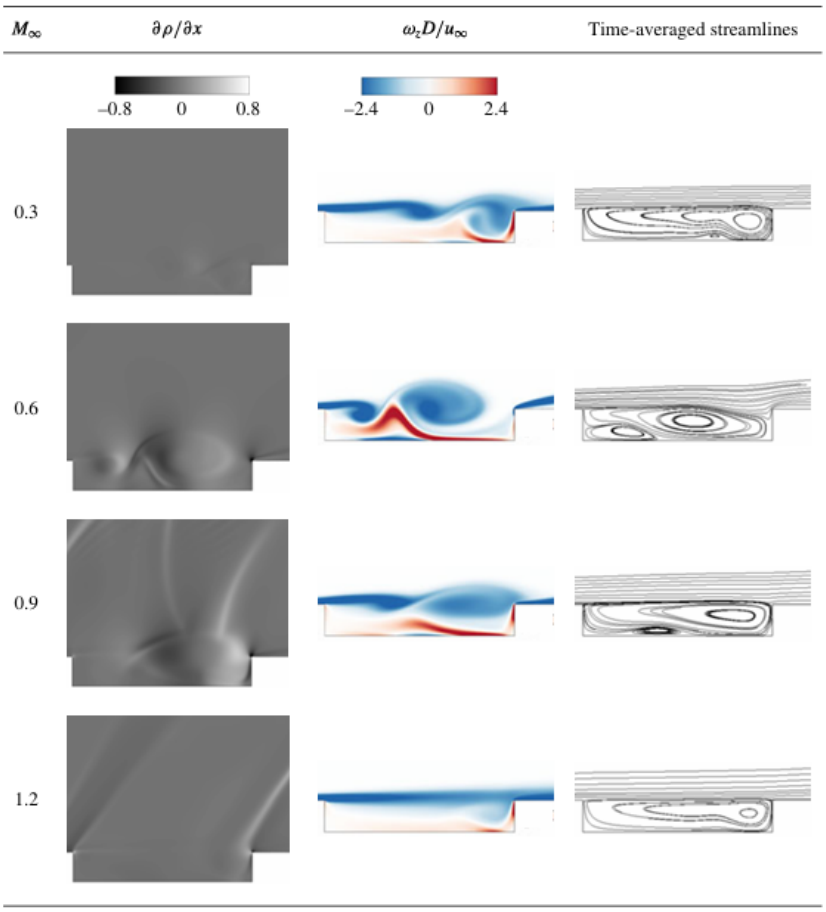

Figure 3.6: *Picture taken from Sun et al. [26]. In the image, the instantaneous numerical schlieren ($\frac{\partial\rho}{\partial x} \in [-0.8, 0.8]$), the instantaneous vorticity contours ($\frac{\omega_z D}{U_\infty} \in [-2.4, 2.4]$) and time averaged streamlines are shown for different Mach numbers ($[0.3, 1.2]$), aspect ratio $\frac{L}{D} = 6$ and $Re_\theta = 19$. It is possible to see compression waves leaving the leading and trailing edges of the cavity as the Mach number is grater than one. Also for the transonic case, the schlieren captures compression waves inside the domain.*

Looking at the different eigenmodes and eigenvalues from stability analysis, it is a direct consequence of what was observed in *Figure* 3.6 that the growth rates tend to decrease as we approach the transonic regime. The results of the global stability analysis executed by Sun et al. [26] are not showed here in details, but it is interesting to discuss briefly the results we obtain whenever three-dimensional modes are considered.
The last analysis run by Sun et al. [26] shows the influence of the Mach number on the three-dimensional eigenmodes. Confirming the results showed by Brès and Colonius [28], even if the increasing Mach number tends to stabilize the modes, it has much less influence than the spanwise structure of the flow. The study reported in the scientific paper are referred to different ratios $\frac{\lambda}{D}$, where λ is the spanwise wavelength of the instabilities (the distance between them) and D is the cavity depth. Apparently, the $\frac{\lambda}{D}$ ratio has much more influence on the flow stability than the Mach number, so in case three-dimensional flows are examined, it is better to evaluate the influence of this quantity.

In order to further investigate the influence of the compressibility in the incom-

pressible and transonic regimes, another work is reviewed here. Yamouni, Sipp, and Jacquin [29] have performed a global stability analysis on an open square cavity flow for $M = [0, 0.9]$, also studying the influence of the acoustic resonance mode on the flow response and the connections between the compressible and incompressible cases. In particular they determined the influence of compressibility on what they called the 'feedback aeroacoustic mechanism' and the acoustic resonance.
In the article, the domain showed in *Figure* 3.7 is used:

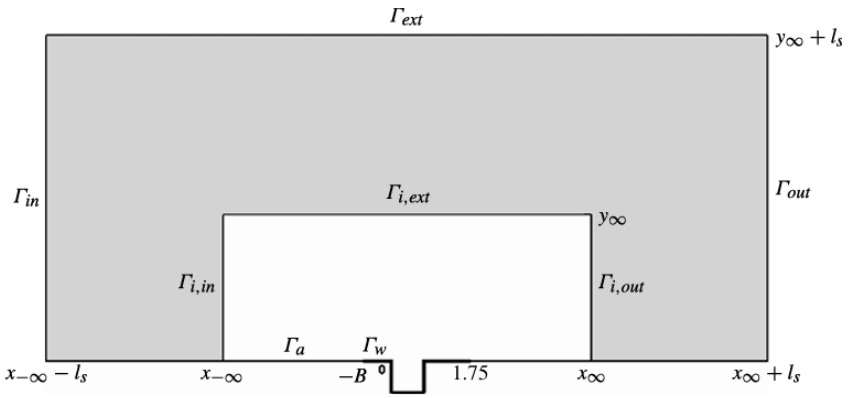

Figure 3.7: *Picture taken from Yamouni, Sipp, and Jacquin [29]. The domain used in the paper is showed. The white area represents the domain of interest, while the grey area is the sponge zone applied to reduce the acoustic reflections. The* Γ_w *thick line represents the non slip condition applied to the cavity walls, while* Γ_a *has a slip condition applied. The inlet condition is used to define the Reynolds number, based on the free stream velocity* U_∞ *and the cavity length* L*, resulting in* $Re = 7500$*.*

The domain of interest is the one depicted in white, as the grey area represents the sponge zone used to damp the acoustic reflections. The boundary conditions applied are the following: Γ_w is a non-slip condition that starts at $(-B, 0, 0)$, where B is fixed to 0.4 in the article; Γ_a on the contrary is a slip condition; the velocity inlet defines the free stream velocity which is used for the definition of the Reynolds number, scaled using U_∞ and L as reference length; in conclusion, a pressure outlet is applied at the outflow.
The base flow is determined for the incompressible case and used to identify the different modes running a global stability analysis. On the $M = 0$ case the influence of the boundary layer momentum thickness is considered, but the results will be brought to the reader's attention in the dedicated subsection of this chapter.
The first results from the cited paper brought here are the Strouhal-growth rate maps for different Mach numbers (*Figure* 3.8). Picture a) represents the global spectrum for different Mach numbers: $M = 0$ (black squares); $M = 0.1$ (diamonds); $M = 0.5$ (triangles) and $M = 0.9$ (circles). We can see that the general trend is again discovered: the growth rates of the different modes decrease as the Mach number reaches higher values. We can also see, however, that as the compressibility effects increase, the number of amplified modes increase as well. In picture b) the trajectories of three different modes with the Mach number is showed. It is evident that the modes have complex trajectories as the Mach increases, and we can also identify multiple local maxima of the growth rates. Again, whenever we reach high Mach numbers, the growth rates tend to decrease.

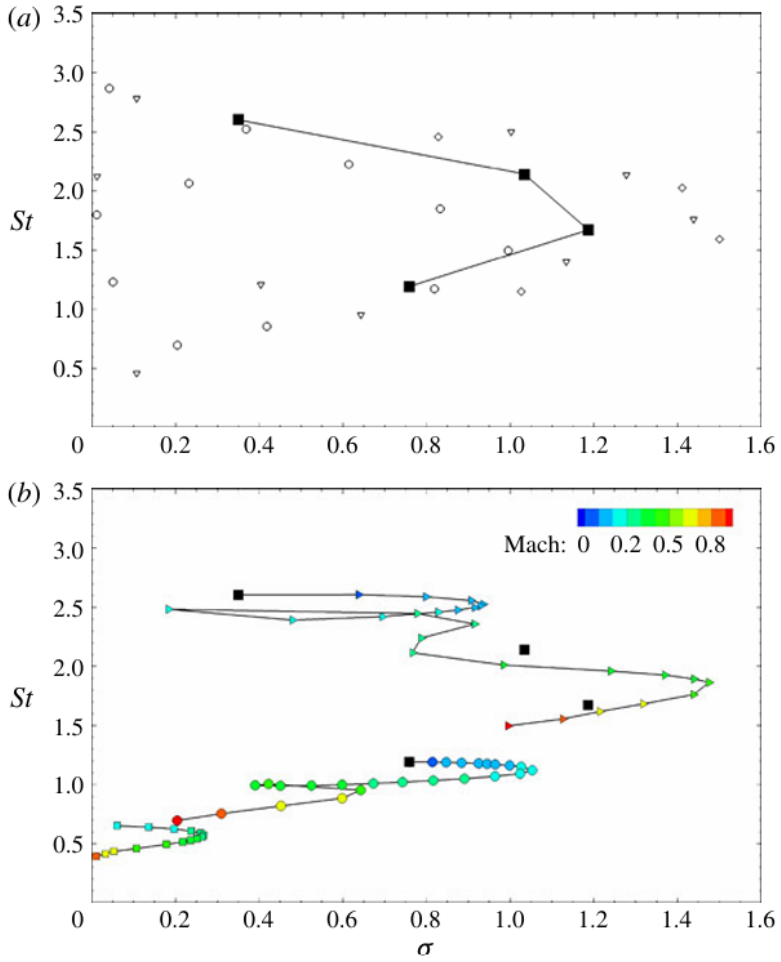

Figure 3.8: *Picture taken from Yamouni, Sipp, and Jacquin [29]. The $St - \sigma$ maps are represented here. Picture a) is the global spectrum obtained at $Re = 7500$ using different Mach numbers: $M = 0$ (■); $M = 0.1$ (◇); $M = 0.5$ (▽) and $M = 0.9$ (○). Please note that a similar trend to the one previously showed is represented here, with the growth rate decreasing as higher Mach values are reached. However, a new behaviour is showed here: although the growth rates are decreasing, there are new modes (stable at lower Mach) that are now unstable. In b) different trajectories of three modes are depicted for different Mach numbers. As we can see, the trajectories are not easily predictable.*

These complex trajectories are considered to be the result of the superposition of two different effects: the feedback aeroacoustic mechanism introduced by Rossiter and the acoustic resonance mechanism.
The feedback aeroacoustic mechanism is said to depend on the synchronization of the vortices in the shear layer and of the acoustic waves travelling backward towards the leading edge of the cavity.
The acoustic resonance mechanism occurs when the wavelengths of the acoustic waves originating at the trailing edge of the cavity is comparable to the cavity dimensions, either in length or depth. The paper aims to determine the contributes of these different mechanisms.
To do so, different branches for the different modes are determined. The branches, indicated with the letter k in Yamouni, Sipp, and Jacquin [29] differ in the number k of structures in the shear layer. Using the relation defined by Rossiter for the

feedback mechanism:

$$St = \frac{j}{\frac{1}{k} + M\left(1 + \frac{0.514}{L/D}\right)} \tag{3.6}$$

it is possible to represent the actual trajectories in a graph overlapping the theoretical curves for the Rossiter mechanism (*Figure* 3.9).

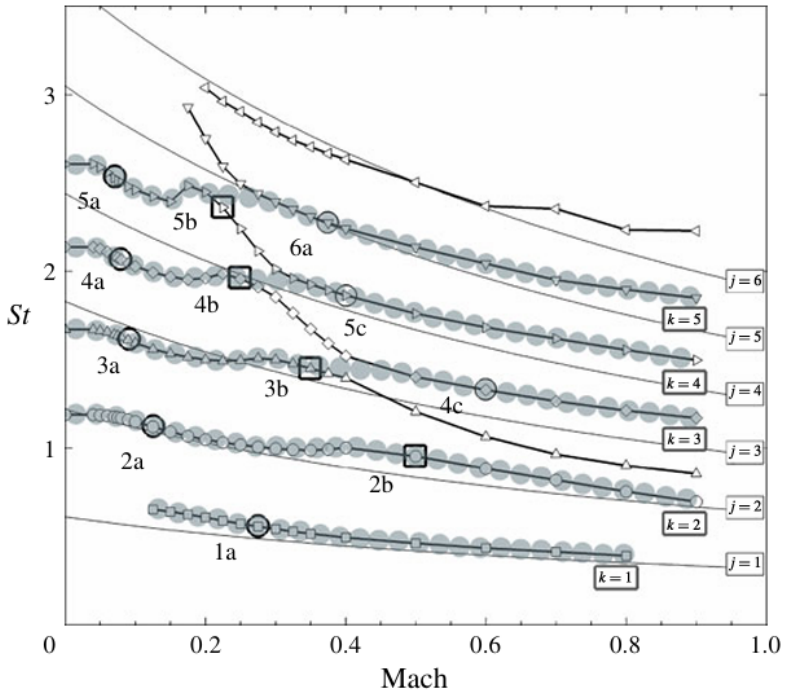

Figure 3.9: *Picture taken from Yamouni, Sipp, and Jacquin [29]. In the figure the unstable mode trajectories with a constant number of structures k are showed using grey shaded circles. The thick solid lines are the feedback aeroacoustic mechanism branches (obtained using the theoretical relation). The light grey lines are referred to the different Rossiter branches obtained varying the modes j with a constant $k = 0.61$. Note that for low compressibility effects (low Mach numbers) the grey circles and the theoretical branches overlap perfectly, so there is a dominance of the feedback aeroacoustic mechanism. Please note that the Rossiter mechanism is also valid in the incompressible regime ($M = 0$). As the number of structures in the shear layer increase we see a change of trajectory, meaning that the Rossiter mechanism isn't the dominant one any more and other effects have to be considered.*

In conclusion, the paper's authors show the evolution in time of the global modes of the branch $k = 3$, representing the pressure inside the cavity for three different Mach numbers, specifically $M = [0, 0.4, 0.8]$. This picture is helpful in finding the differences between the incompressible and compressible cases, so we propose again the results here (*Figure* 3.10). The pictures represents two different segments at $x = -1 : 1.9$, $y = 0$ and at $x = 0 : 1$, $y = -0.25$, respectively the left and right column. Four segments are defined, and their slopes represent the propagation speeds of the waves: positive slopes mean that the wave is propagating downstream, while negative slopes mean the propagation's direction is towards the upstream edge of the cavity. Considering the slopes of segments (2) and (4) we notice that they are nearly independent from the Mach number.

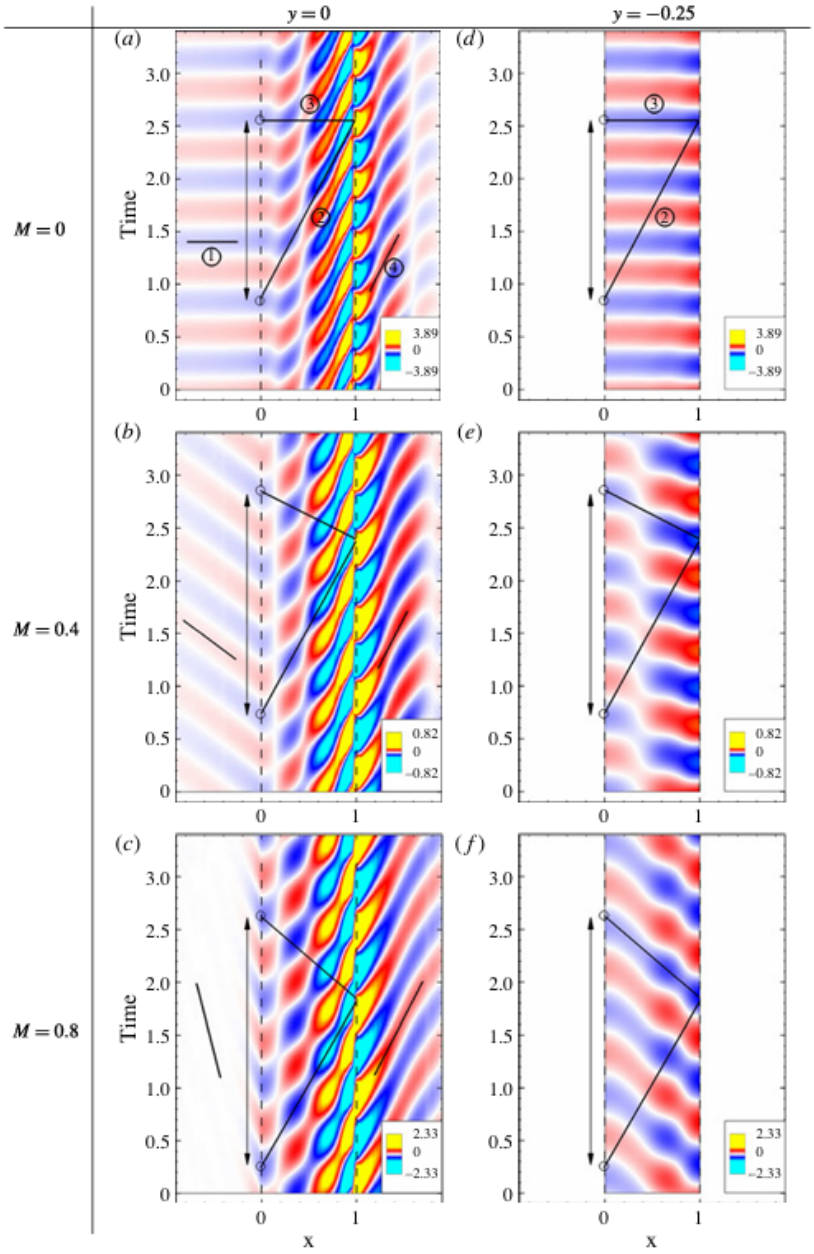

Figure 3.10: *Spatio-temporal evolution of the global modes of the branch $k = 3$ (taken from Yamouni, Sipp, and Jacquin [29]). The pressure is represented for two segments at $x = -1 : 1.9$, $y = 0$ and at $x = 0 : 1$, $y = -0.25$, so considering the cavity and the shear layer above it (left column) and a region just below the shear layer (right column). The slopes of the segments (1)−(4) represent the propagation speeds of the structures: if positive they propagate downstream, while negative slopes mean that the waves are propagating upstream. As the slope of the segments inside and outside the cavity (segments (2) and (4)) are not really influenced by the Mach number, the compressibility create reflecting waves leaving the trailing edge with different speeds (segment (3)). The same pattern is seen in the shear layer and below it. Also note that the acoustic waves are weaker than the main structures hitting the trailing edge of the cavity.*

The main difference between the incompressible and compressible cases stands in the reflection of the waves impacting the trailing edge of the cavity. Reflections propagate upstream with increasing speed depending on the Mach number. The same pattern is distinguished in the shear layer (left column) and slightly below it

(right column). On the dotted line for $x = 0$ it is possible to see two circles pointing at the starting end ending points of a wave, considering the reflection too. In conclusion, note that the reflected waves are less intense respect to the downstream propagating structures impacting the trailing edge.

In the work of Yamouni, Sipp, and Jacquin [29] the acoustic feedback produced by the trailing edge of the cavity is evaluated thanks to the compressible formulation used. However, it is possible to capture the acoustic pattern of cavity flows also considering the incompressible formulation, as it has been done by Bailey, Abbá, and Tordella [30]. In this article, the cavity is considered as an energy collector. The pressure transport and kinetic energy transport are considered evaluating the inflow and outflow from the cavity. This paper aims to link these quantities to pressure wave emission from the downstream edge of the cavity. A channel Poiseuille flow is considered here at different Reynolds number based on the bulk velocity and the semi-height of the channel. A cavity of aspect ratio $\frac{L}{D} = 4$ is then located in the channel. The Mach number defines the incompressible conditions, as it is equal to $M = 1e^{-3}$. The authors considered a numerical coefficient α to relate the pressure and the kinetic energy transport, so that:

$$pv = \alpha \rho E v \tag{3.7}$$

where E is the kinetic energy per unit mass, v the wall normal velocity component, p the pressure. The Reynolds number considered are in the range $Re = [25, 2900]$ so that the flow clearly goes from a laminar case to the turbulent one. Given that turbulence is obtained for $Re = 2900$, there will surely be acoustic waves production from the cavity. Although the incompressible formulation is used, for this Reynolds number the authors identify from the pressure field some high and low pressure spots that are a sign of acoustic emission (*Figure* 3.11).

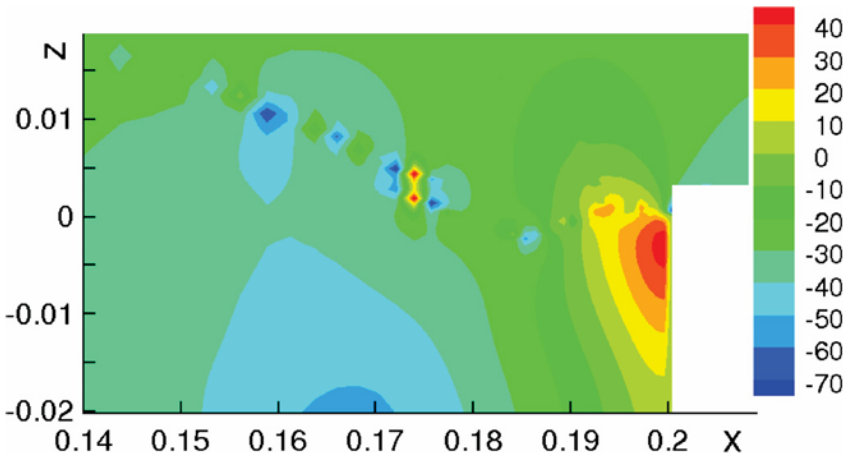

Figure 3.11: *Picture taken from Bailey, Abbá, and Tordella [30]. Pressure field inside the cavity, specifically close to the downstream edge, at Reynolds $Re = 2900$ and $M = 1e^{-3}$. Note that although the incompressible formulation is adopted in this study, we can still observe some high and low pressure spots leaving the downstream edge surface. These spots are considered to represent the acoustic waves generated from the impinging flow on the cavity edge.*

Bailey, Abbá, and Tordella [30] then have extrapolated informations about the Reynolds number corresponding to the first acoustic emission. The details about the analyses executed are showed in [30], but we find interesting that from an incompressible formulation, it is still possible to determine the range of Reynolds numbers where we expect the acoustic emission to occur. In this case, observing the dimensioned absolute values of the pressure and kinetic energy transport across the cavity mouth varying the Reynolds number, we can suppose that at $Re = 1000$ the unsteady features of the flow (so the instabilities) first occur (*Figure* 3.12).

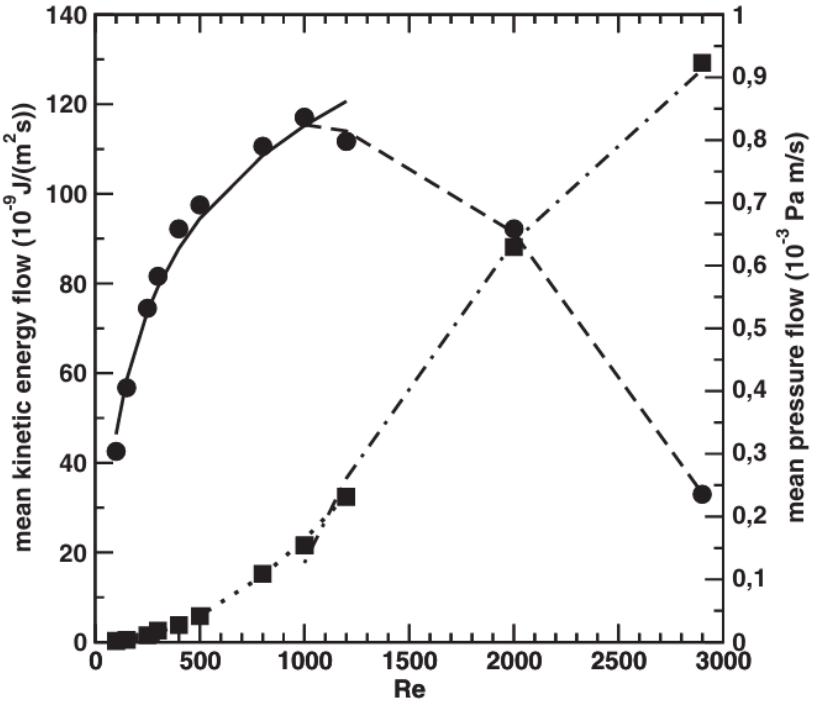

Figure 3.12: *Picture taken from Bailey, Abbá, and Tordella [30]. The dimensioned absolute values of the pressure and kinetic energy transport are showed for a cavity at* $M = 1e^{-3}$ *at different Reynolds numbers. The dots represent the pressure transport, while the squares the kinetic energy transport. We put the focus on the change in behaviour obtained after* $Re = 1000$*. It is in fact possible to distinguish a descending behaviour of the pressure transport interpolation curve (meaning pressure outflow from the cavity becomes greater than the inflow). This behaviour is considered to be a consequence of the generation of acoustic waves leaving the cavity. The kinetic energy transport also sees a change in the behaviour going from an exponential growth to a logarithmic one.* $Re = 1000$ *is then considered the first occurrence of unsteadiness (instabilities).*

We conclude that it is possible to gain informations about flow instabilities from an incompressible study.

3.2.4 Influence of the Reynolds number

The Reynolds number is of course one of the most influencing parameters, so that multiple papers have been written about its influence on the flow stability.
To discuss its impact on the eigenspectrum we briefly comment the results of Brès and Colonius [28] and Meseguer-Garrido et al. [31]. First, it is best to repeat that the influence of the different parameters is usually stronger on two-dimensional cases

compared to the three-dimensional ones. However, the general trend is always the same. Brès and Colonius [28] have executed one of the first and most complete studies on three-dimensional open cavity flows determining the influence of multiple parameters on the flow stability. Without commenting again the results obtained for each one of them, the behaviour of the flow with increasing Reynolds number is the same obtained in this thesis work: as the Reynolds increases, the growth rates tend to increase as well. There is a difference on the effect of the Reynolds number on the frequency of the modes depending if the flow is 2D or 3D. Specifically, in their work, where three-dimensional cavities are considered, the frequency tend to decrease slightly when the Reynolds number is increased, while in two-dimensional flows (as the one considered in this thesis) the frequency increases slightly. The important influence of the Reynolds number is a direct consequence of the change in viscosity, given that this last one has a stabilizing role on the flow.
Moreover, as explained in Meseguer-Garrido et al. [31], increasing the Reynolds number also means that there is an increase in the velocity gradient in the shear layer, which is one of the main mechanisms that brings energy to the smaller perturbations.
The Reynolds number also influences the flow reattachment to the cavity downstream wall when closed cavity flows are considered. As presented in Bailey, Abbá, and Tordella [30], when low Reynolds cases (laminar cavities) are considered, reattachment is expected approximately ten cavity depths downstream of the upstream edge. Of course this can vary depending on the Reynolds but also the aspect ratio of the cavity. For high Reynolds numbers (turbulent cavities) the reattachment is considered to be less dependent on the specific Re and is accepted to be around six cavity depths downstream of the upstream edge (again the aspect ratio can influence this behaviour). If the aspect ratio is small compared to the channel height or the cavity flow is open, then the reattachment is considered to be close to the trailing edge of the cavity without any particular dependence on the Reynolds number. As we have explained, in this case the Reynolds number influences the position of the main eddy, that moves towards the trailing edge as the Reynolds increases.

3.2.5 Influence of the boundary layer thickness

Again, as the boundary layer thickness is an important parameter controlling flow instabilities, many research papers have been published determining its influence. As it is briefly explained by Meseguer-Garrido et al. [31], the decrease of the boundary layer thickness has the same effect as increasing the Reynolds number: a thinner boundary layer leads to larger gradients in the shear layer, making the destabilization of the flow easier. Again, its effect on two-dimensional flows is greater than on three-dimensional cases, as introduced by Squire's theorem and partially verified through numerical and experimental works. The same conclusion has been obtained by Brès and Colonius [28], where a relation has been deducted from the numerical results:

$$\omega_r \propto \frac{D}{\theta_0} \tag{3.8}$$

where ω_r is the growth rate of the most amplified mode, D is the cavity depth and θ_0 corresponds to the boundary layer thickness. It is said by *Brès* that for constants values of Re_D, M and aspect ratio, this relation is qualitatively valid.

Again, the same is obtained by Mathias and Medeiros [27], where the influence of the Mach number and of the incoming boundary layer thickness is studied. As previously said, the authors prove again that if the boundary layer is thinner, then the leading eigenvalues have a grater growth rate. A final demonstration comes from the visualization of the eigenspectrum obtained by Yamouni, Sipp, and Jacquin [29] for a square cavity ($\frac{L}{D} = 1$) at $M \approx 0$ and $Re = 7500$ (*Figure* 3.13).

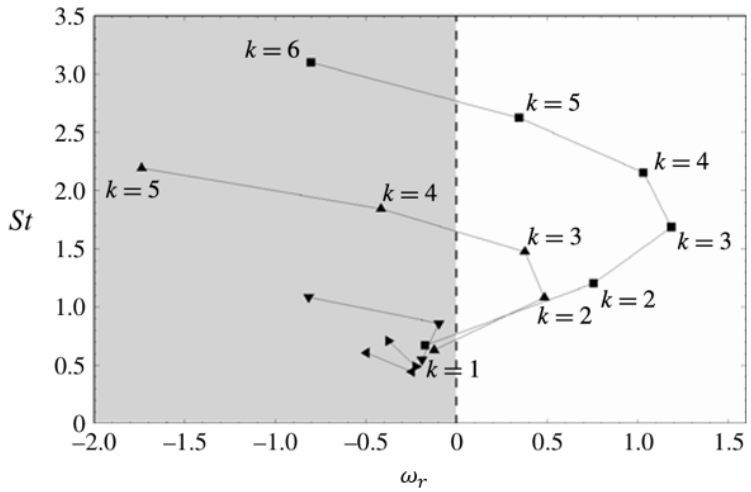

Figure 3.13: *Picture taken from Yamouni, Sipp, and Jacquin [29]. The eigenspectrum for a cavity with aspect ratio* $\frac{L}{D} = 1$, $M \approx 0$ *and* $Re = 7500$ *is showed for different ratios* $\frac{L}{\theta_0}$*:* $\frac{L}{\theta_0} = 231$ *(■);* $\frac{L}{\theta_0} = 110$ *(▲);* $\frac{L}{\theta_0} = 52.7$ *(▼);* $\frac{L}{\theta_0} = 38.9$ *(►),* $\frac{L}{\theta_0} = 34.2$ *(◄). As we can see, as the thickness is increased the growth rate decreases and the frequency slightly changes. The number k is related to the number of coherent structure in the shear layer.*

The behaviour is coherent with what expected. Using different ratios of $\frac{L}{\theta_0}$ we can see that as the thickness increases the growth rates decrease. The frequency slightly decreases as well, and this behaviour is also expected given that as the thickness increases the convection speed of the vortices in the shear layer decreases too.

3.2.6 Influence of the aspect ratio

To conclude this chapter we highlight one last time the influence of the aspect ratio of the cavity.
Citing what explained by Meseguer-Garrido et al. [31], when the aspect ratio is close to $\frac{L}{D} = 1$ the size of the perturbation is constrained by the one of the cavity. This tends to stabilize the flow given that the cavity walls limit the growth of the perturbations inside the cavity itself. On the contrary, when the length-to-depth ratio increases, the main vortex is not bounded by the walls, making space for other perturbations to grow inside the cavity. Moreover the increase in the cavity's length makes the shear layer able to amplify the disturbances even more, as written also in Sun et al. [26].
The results obtained by Meseguer-Garrido et al. [31] for the influence of the aspect ratio are showed in *Figure* 3.14.

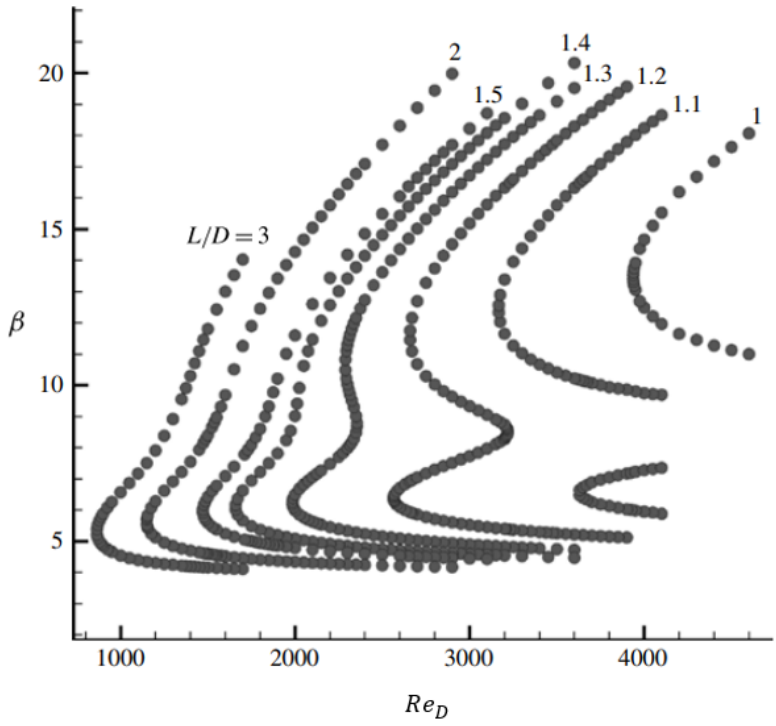

Figure 3.14: *Image taken from Meseguer-Garrido et al. [31]. The neutral curve of an open cavity flow is showed for different aspect ratios. As the aspect ratio is increased, the unstable region increases in size, meaning that the critic Reynolds occurs at lower values. We can see how this parameter has a huge influence on the flow stability.*

In the light of the reviewed studies, the following case presented in *Chapter 4* was designed to explore the stability behaviour of an open cavity flow with Re = 502 and M = 0.6, parameters consistent with the literature's critical ranges.
In this thesis we will also study the influence of the Reynolds number and of the Mach number our cavity geometry, without exploring deeply the other parameters cited above.

Chapter 4

Analysis of a cavity invested by a flow at $Re = 502$ and $M = 0.6$

Now that the theory behind this master thesis' work is explained, it is possible to introduce the actual case study taken in consideration for the stability analysis.
As explained in the introduction of this report, the goal is to validate and confirm the IC3 solvers' capability of solve global stability analysis problems, checking the boundary conditions imposed in the different simulations. In order to achieve such a goal, an article published by Sun et al. [11] in 2017 is examined and considered to have a qualitative comparison of the results, looking how the boundary conditions influenced the solutions.

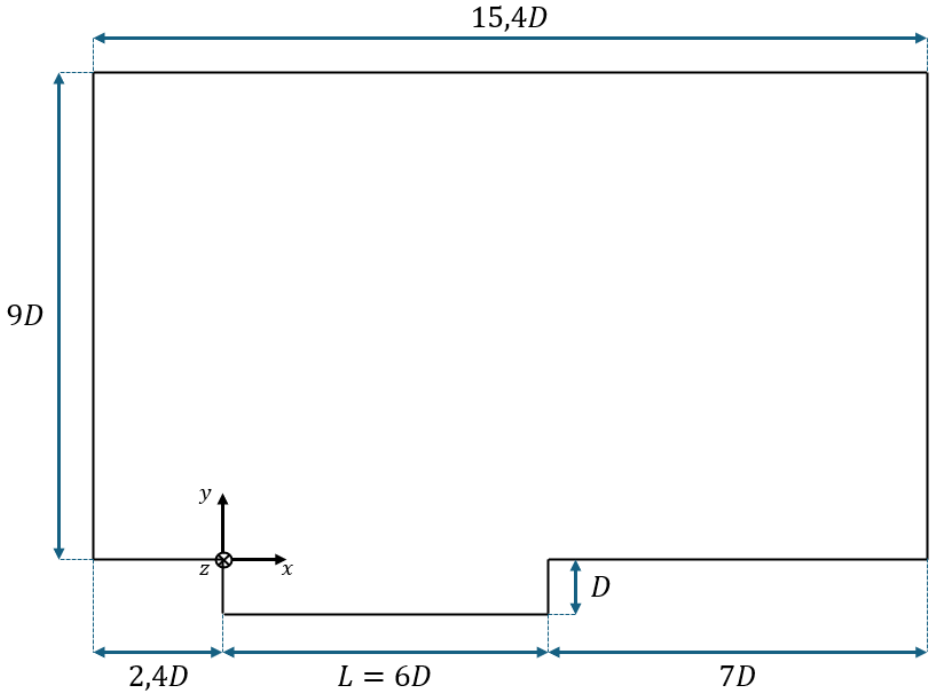

Figure 4.1: *Schematic representation of the fluid domain. The dimensions are given as $n \cdot D$, where D represents the cavity depth which is also considered as the characteristic length of the system. The different sizes' lengths are taken from Sun et al. [11] in order to obtain comparable results. The origin of the reference system is positioned in the upstream edge of the cavity.*

4.1 Physical domain

The physical domain is created based on the geometry used in the article of *Sun et al.*
Even if the simulation considers a bi-dimensional cavity, the domain has to be created as a three-dimensional geometry to make IC3 execute the code. No initial condition are imposed in the z direction, so in the following paragraphs this coordinate will be neglected, but it is necessary to know that very thin 3D grid elements have to be used to run simulations.
The geometry is then represented in *Figure* 4.1.

The reference frame has its origin positioned exactly in the upstream edge of the cavity, as depicted in the picture. The different sizes are given as a function of the cavity depth D, which is here considered the characteristic length of the system. Given that this work is completely numerical, a cavity depth of 1 meter has been considered, in order to have a grid size that does not require excessive resolution and computational power to be resolved.
The fluid flows along the x direction, from now on called *streamwise direction.*

4.1.1 Boundary conditions

With the assumption of the flow moving along the streamwise direction, the fluid regions are set as it follows (*Figure* 4.2):

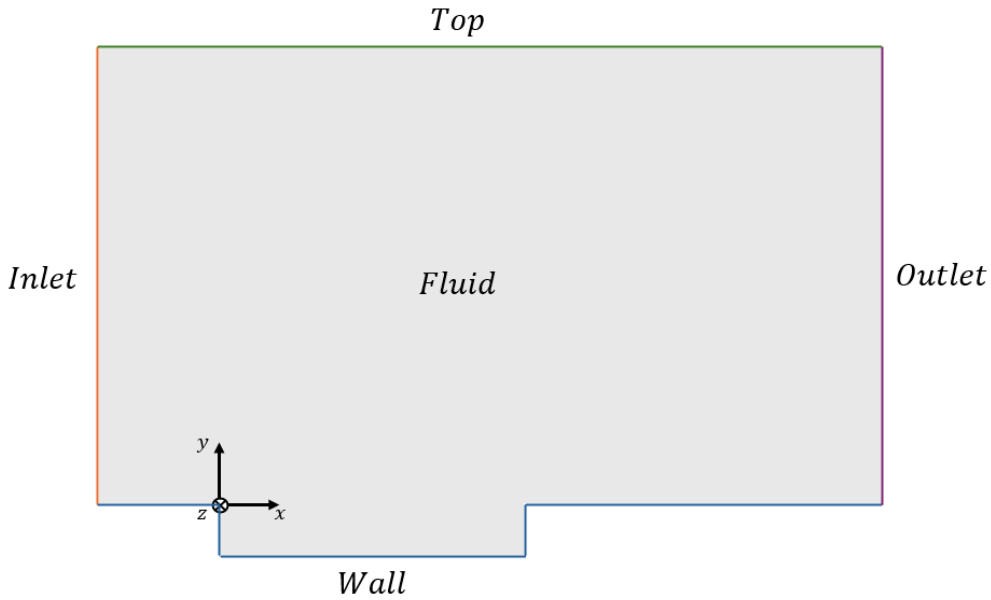

Figure 4.2: *With the hypothesis of the fluid flowing along the x direction, the boundaries are associated with the terms showed in the picture.*

One of the goals of this thesis work is to validate different boundary conditions implemented in IC3 and to evaluate any differences in the results. In particular, the focus is put on the upper surfaces boundary condition: usually at this surface a *porous boundary condition* is applied, which defines the static temperature and pressure and the undisturbed flow' s velocity. This condition is valid when we

consider to be in the farfield.
However, the *top* surface during the simulations may see different fluctuations in the flow, resulting in some perturbations carrying the flow outside/inside the domain, making the usual free stream condition no more adequate (*Figure* 4.3 case (a)).
In order to cancel this possible issue and to compare the obtained results, a different domain geometry is built, using a slightly inclined top surface. In particular, a 2° angle is applied. Even if the angle is small, it is considered sufficient to contain every possible fluctuation of the flow (*Figure* 4.3 case (b)). Of course the boundary condition applied to the new inclined top surface is no longer of porous surface, but it becomes a *velocity inlet* bc.

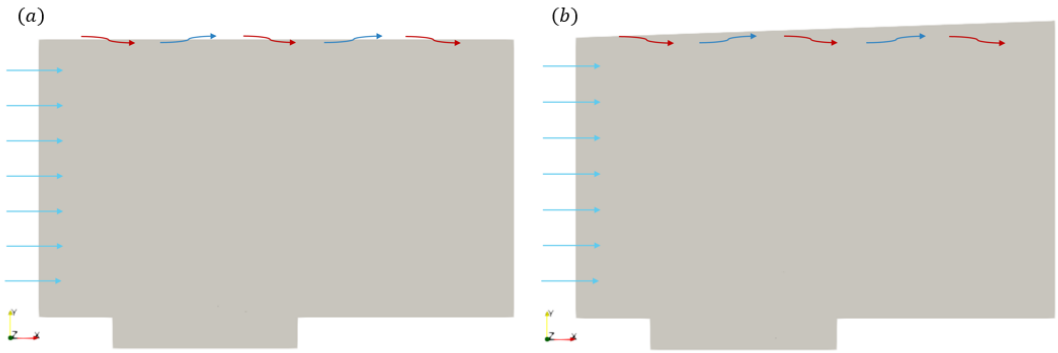

Figure 4.3: *Schematic representations of the fluctuations that could occur at the upper (top) surface. In (a) the flat surface has a porous boundary condition applied i.e. we suppose that we already are in the undisturbed farfield with the flow parallel to the (fictitious) surface. In this configurations, eventually, some oscillations could occur causing the flow to exit/enter the fluid domain, making the porous bc obsolete. In (b) the slightly inclined top surface is created in order to contain every eventual fluctuation of the flow. In this case the applied boundary condition is that of velocity inlet.*

The remaining surfaces maintain the same boundary condition in both the two cases. The applied bcs are resumed in *Figure* 4.4:

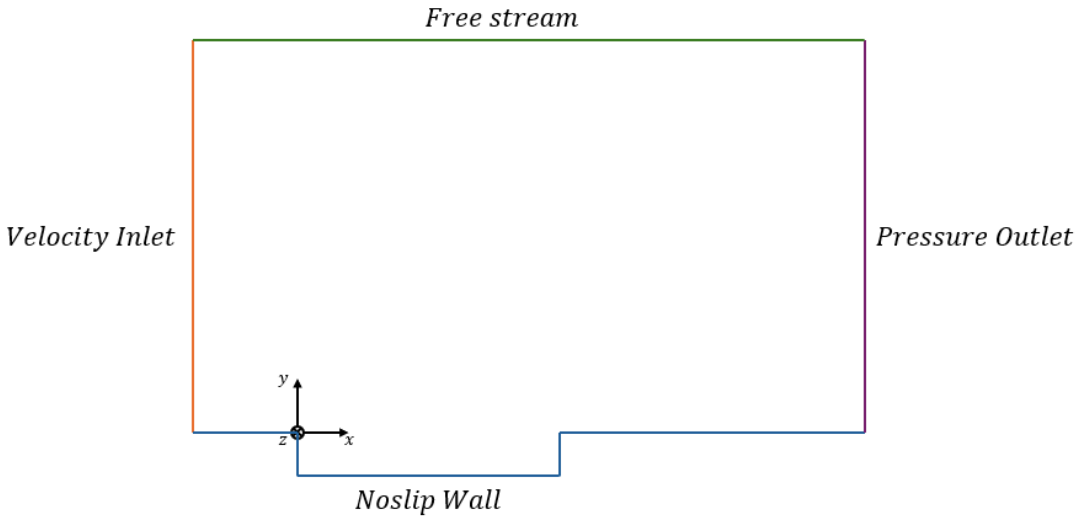

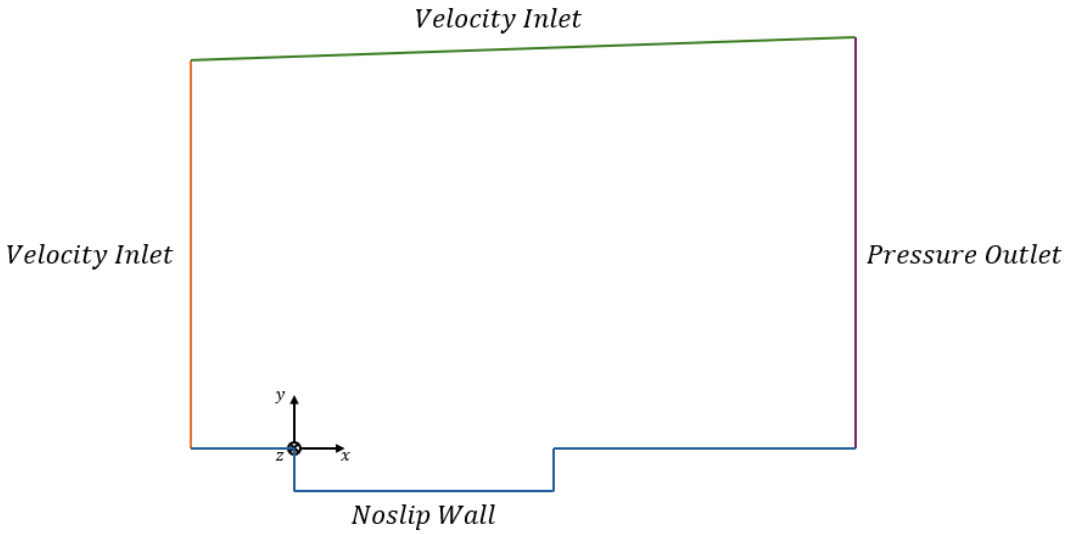

Figure 4.4: *Schematic representations of the boundary conditions applied to the fluid domain: the two different configurations have the same boundary conditions apart from the top surface, whose differences between the two cases has been already well discussed.*

From a practical point of view, the inlet boundary conditions applied to the fluid regions are based on the solving of a Riemann problem between a left state containing the informations provided by the user and a right state being the first fluid cells of the boundary condition; the pressure outlet is defined by imposing the static pressure on the subsonic boundary; the wall condition is considered to be adiabatic and the solver impose automatically a no-slip condition.
Please note that the domain is built as a three-dimensional space. In order to make it bi-dimensional for the solver periodic boundary conditions are set to the *fluid* region (given by the extrusion of the bi-dimensional geometry, schematically represented in *Figure* 4.2) so that the domain becomes an infinite extruded domain and can be considered two dimensional.

4.1.2 Initial conditions

The initial conditions are determined in order to simulate a flow in the same conditions as Sun et al.
In the article it is said that the Reynolds number is $Re = 502$ and the Mach $M = 0.6$. In order to obtain these same non-dimensional values the fluid dynamic similarity is used, given that no experimental counterpart of the future analysis will be executed. The initial condition and reference physics quantities are defined as in *Table* 4.1:

$Re = 502;\ M = 0.6$				
$U_x\ [\frac{m}{s}]$	$P\ [Pa]$	$T\ [K]$	$\rho_{ref}\ [\frac{kg}{m^3}]$	$\mu_{ref}\ [Pa \cdot s]$
204.23	101325	288.15	1.225	0.49837

Table 4.1: *Table containing the initial condition values and reference physics values imposed in the simulation for a flow at* $Re = 502$ *an* $M = 0.6$.

Both in Sun et al.' s article and here, the boundary layer develops from the beginning

of the fluid domain, for $x = -2.4$ $[m]$ following the reference system from *Figure* 4.1.

4.1.3 Mesh

Different meshes are created in order to capture precisely the phenomena happening inside the cavity and in the shear layer. The mesh is executed using an external software, ICEM CFD. Using this simple mesher it is possible to build the geometry and create adequate meshes. Simple quad elements are used to build the non-uniform grid, although varying the numbers in order to detect any difference in the results. The goal is to achieve a sufficient grid resolution inside the cavity and close to the wall, while increasing the cell sizes going towards the farfield. The first mesh used to run DNS simulations contains 379000 elements (*Figure* 4.5):

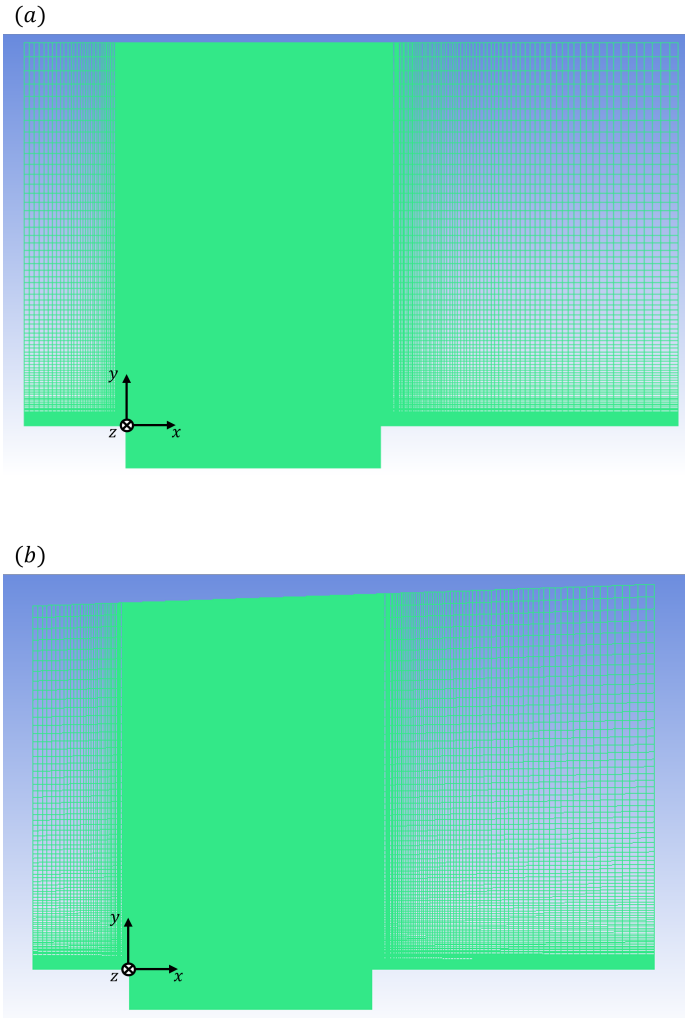

Figure 4.5: *First meshes actually used to run simulations. This meshes contained 379000 elements which was later discovered to be an unnecessarily amount. The grids were realized using the software ICEM CFD. In the picture both the flat top* (*a*) *and inclined top* (*b*) *geometries and grids are showed.*

Running some DNS simulations using these two meshes some acoustic reflections are discovered inside the cavity just from the visualization of the pressure (*Figure* 4.6).

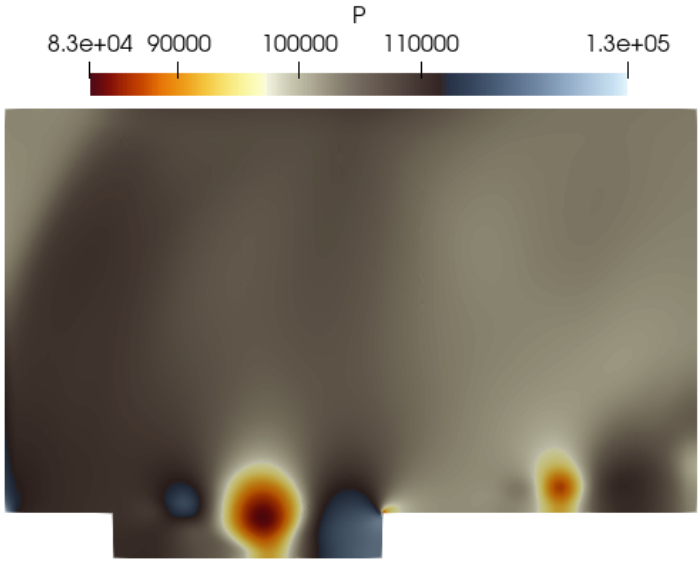

Figure 4.6: *Looking at the visualization of the pressure in the fluid domain using the mesh depicted in Figure 4.5 it is possible to see pressure fluctuations in the farfield, probably caused by acoustic reflections from the outlet boundary.*

In order to avoid these fluctuations the grid is modified. If such corrections are not made, the acoustics phenomena happening inside the cavity would be mixed with the reflections from the outer boundary compromising the results of the simulations.

The grid is modified introducing a *sponge zone* towards the outer boundary to mitigate the reflections (*Figure* 4.7).

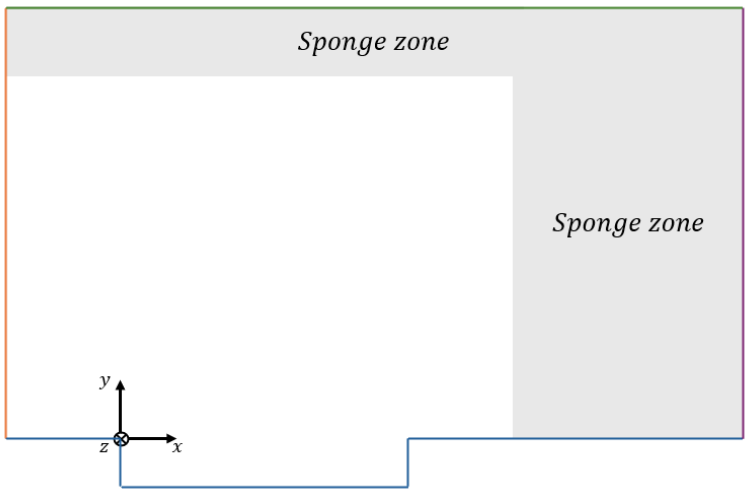

Figure 4.7: *Schematic representation of the sponge zone inside the fluid domain. The sizes of the sponge zones here represented are not to scale, they are just meant to show their position.*

The sponge zones are implemented using two different techniques:

- Implementing in the code a sponge zone that automatically mitigates the reflections (acting as a filter) without modifying the mesh;

- Changing the grid towards the boundary increasing the cell size such that numerical dissipation mitigates the fluctuations

Both the two methods are achieved and used, but given the simplicity of the analyses, the second (easier) method is the one applied giving optimal results. Moreover, in this way the number of grid elements is reduced without losing quality in the results. The final meshes with the application of the sponge zones (as gradient in the grid elements' size towards the outlet) are showed in *Figure* 4.8:

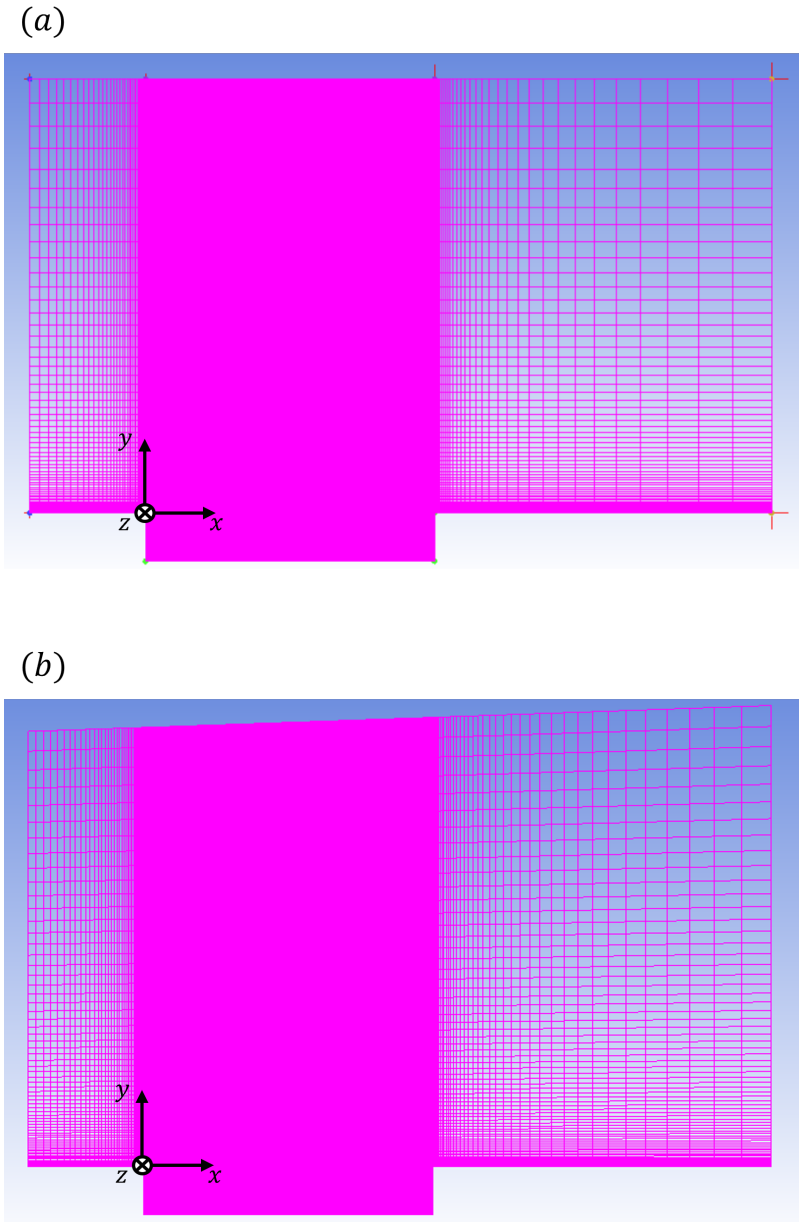

Figure 4.8: *Final meshes used for the following analyses for the flat top geometry* (*a*) *and the inclined top geometry* (*b*). *Both the meshes have around 127000 grid elements.*

4.2 Numerical Methods

Talking about the mesh it was told that simulations are run in order to evaluate the best grid configuration possible. Any information about the numerical methods

implemented in IC3 to run the analyses was until now ignored. This paragraph aims to give the reader some knowledge about the numerical methods applied.

The IC3 solver can solve CFD problems using two spatial numerical schemes:

- *Finite volumes*: the solution is determined as mean value in each cell and it is associated to the center of each element (*Figure* 4.9);

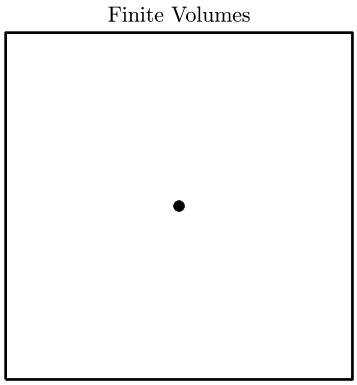

Figure 4.9: *Schematic representation of a grid element in which the solution has been determined implementing finite volumes method. In this case the solution is defined as mean value of the solution in the grid element and the value is associated to the element's center.*

- *Spectral methods*: the values of the flow quantities is determined by the interpolation of an $n-degree$ polynomial in different points inside the grid element , the so-called *solution points* (*Figure* 4.10). Given that the number of solution points is higher than finite volumes, it is possible to use coarser grids without reducing the total number of degrees of freedom of the mesh. The downside is that the method is computationally more requiring.

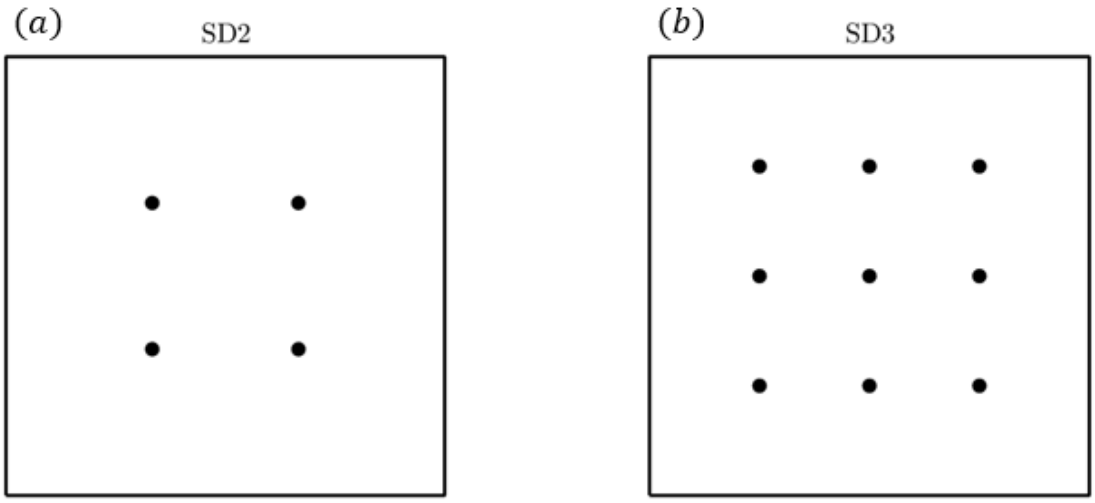

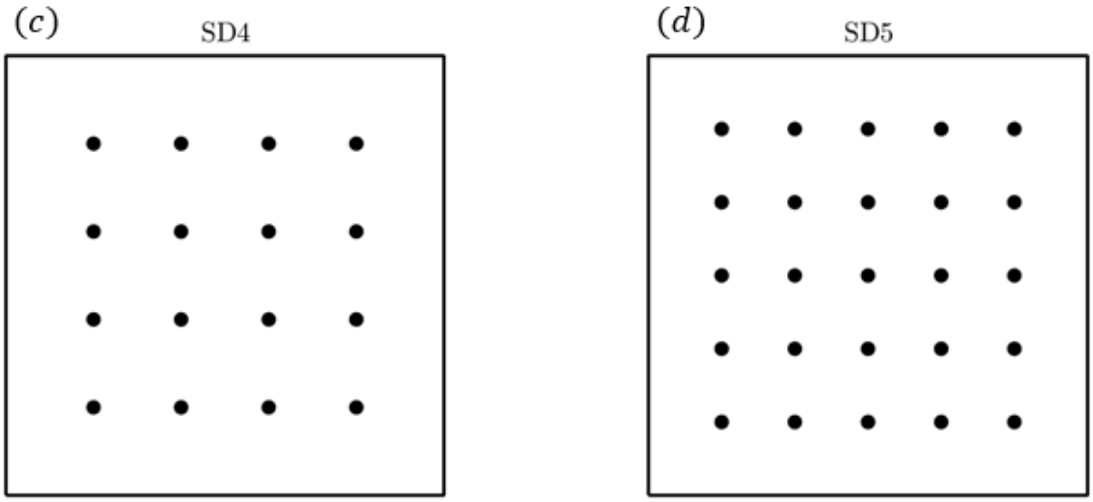

Figure 4.10: *Schematic representation on how spectral methods evaluate the solution inside the single grid element. Depending on the polynomial's degree chosen, different numbers of solution points are allocated inside the element. The solution is determined by the interpolation of the polynomial of the values in correspondence of the solution points.*

Both these two different methods are applied in order to verify that the obtained results are the same.
For what concerns the time integration method, a third order, three stages Runge-Kutta method is implemented, which is an explicit method commonly used in CFD problems. Further knowledge about the Runge-Kutta time stepping method can be found in Butcher [32].

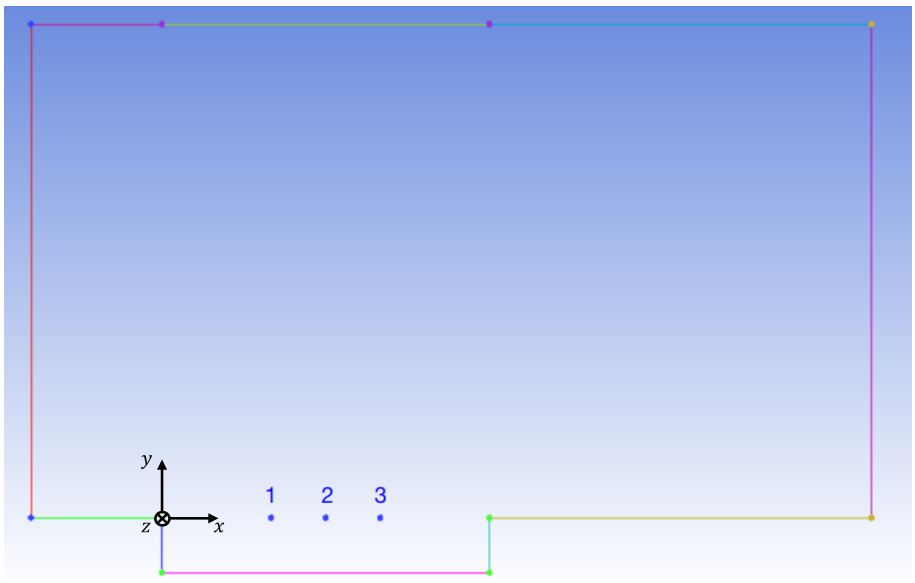

Figure 4.11: *Three different probes are located inside the shear layer in order to determine the shedding frequency. In particular, the goal is to obtain the same shedding frequency that Sun et al. determined evaluating the shear layer in* $(3, 0, 0)$ $[m]$*, i.e. the middle of the cavity.*

4.3 Frequency spectrum

Once the simulations setup is ready, the first goal of the analyses is to determine the frequency of the shedding phenomena that distinguishes the cavity flow under the conditions $Re = 502$ and $M = 0.6$, as underlined in [11]. In order to capture the shedding of the vortices in the shear layer, different (fictitious) probes are inserted inside the fluid domain (*Figure* 4.11).
The three probes are used to capture the velocity along the x direction U_x of the cavity, in order to subsequently use the *Fast Fourier Transform* to determine the frequency spectrum of the cavity. Even if we expect the shedding frequency to be small, given the high computational power an acquisition frequency of $f_s = 10\ kHz$ is used.

4.3.1 Fast Fourier Transform

The *Fast Fourier Transform (FFT)* is adopted to determine the frequency spectrum of the cavity flow studied. The FFT is an algorithm whose purpose is to compute *Discrete Fourier Transform (DFT)* efficiently. It is then mandatory to introduce the DFT before approaching the FFT.
The DFT of a time-based continuous signal using N samples (depending on the acquisition frequency) produces a frequency range representation with the same number of samples N. If we call $f(t)$ the continuous time signal that represents the source of the data and $f[0], f[1], f[2], ..., f[N-1]$ the N samples that we obtain from the probes, we have:

$$F(j\omega) = \int_{-\infty}^{\infty} f(t)e^{-j\omega t}\,dt \tag{4.1}$$

Which is the Fourier Transform of the original temporal signal. We could consider each sample $f[k]$ as an impulse having area $f[k]$.
Then, since the integrand exists only at the sample points:

$$\begin{aligned} F(j\omega) &= \int_{0}^{(N-1)T} f(t)e^{-j\omega t}\,dt \\ &= f[0]e^{-j0} + f[1]e^{-j\omega T} + \cdots + f[k]e^{-j\omega kT} + \cdots + f(N-1)e^{-j\omega(N-1)T} \end{aligned}$$

That is equal to:

$$F(j\omega) = \sum_{k=0}^{N-1} f[k]e^{-j\omega kT} \tag{4.2}$$

Moreover, if the signal is periodic, the expression can be considered as:

$$F[n] = \sum_{k=0}^{N-1} f[k]e^{-j\frac{2\pi}{N}nk}, \quad (n = 0 : N-1) \tag{4.3}$$

The results are the frequency range representation of the temporal signal. Moreover, if Δt is the time interval between the samples the resulting frequency interval will be:

$$\Delta f = \frac{1}{N\Delta t} = \frac{f_s}{N} \tag{4.4}$$

The cost of the Discrete Fourier Transform is quite high, given that it requires $N \times N$ operations that are time and memory intensive.
Here comes the usage of different algorithms that reduce the cost of the DFT. In particular, the Fast Fourier transform reduces the total number of complex operation to $N \cdot log_2 N$, which gives a great saving. Basically the Fast Fourier Transform divides the signals in two halfs recursively, recreating the complete spectrum solving each smaller problem.

4.3.2 Results

Two different methods were used to determine the FFT. Firstly, the FFT is applied on the streamwise velocity signal U_x that is sensed by the fictitious probes inside the shear layer. The FFT is calculated using the MATLAB function *fft* and it is normalized by the velocity magnitude. As in [11] the spectrum is determined as a function of the non-dimensional frequency, i.e. the Strouhal number. The obtained spectrum is the one showed in *Figure* 4.12:

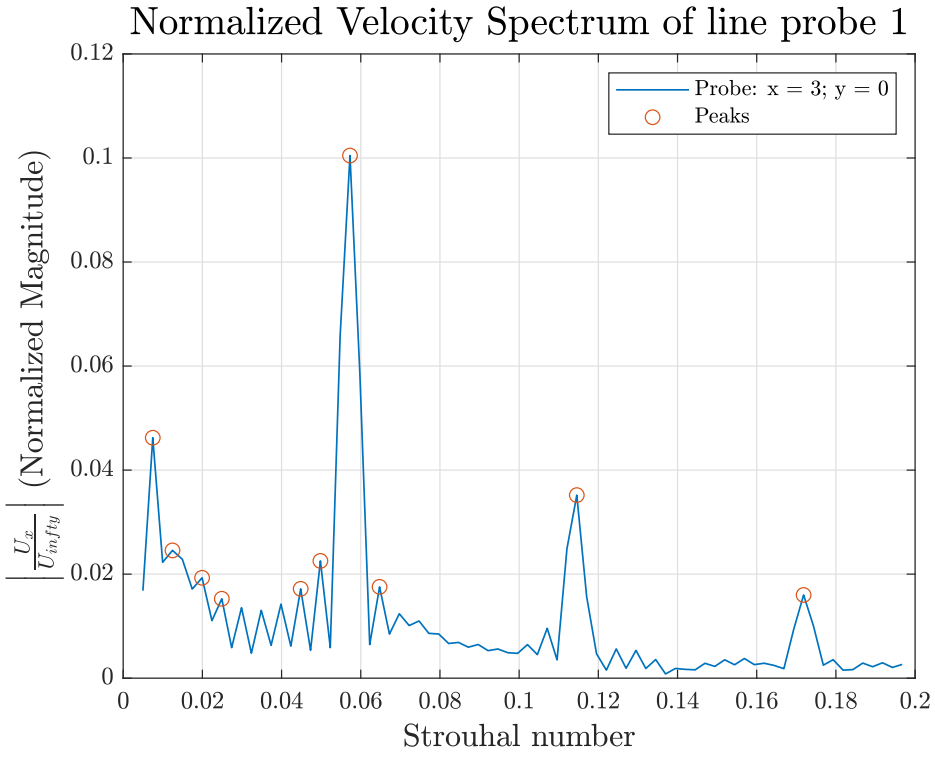

Figure 4.12: *FFT spectrum of the normalized streamwise velocity of a fictitious probe locted in the middle of the cavity. The aim of the FFT is to determine the frequency (here non-dimensional as the Strouhal number) of the periodic shedding phenomena that distinguish a cavity flow under the conditions $Re = 502$ and $M = 0.6$. The spectrum is determined using a MATLAB script that included a high-pass filter to select the desired data and a function for peaks determination.*

As it can be seen from *Figure* 4.12, the first peak is considered to be indicative of the vortex shedding, and the other peaks are located for discrete multiples of the frequencies, representing the harmonics. From the FFT, a Strouhal number of

$St = 0.05728$ was identified for the shedding periodic instability. Please note that we do not know (given the analyses run until now) the critic Reynolds neither when the Hopf bifurcation happens.

At this point the spectrum is compared with the one obtained by Sun et al. [11] (*Figure* 4.13).

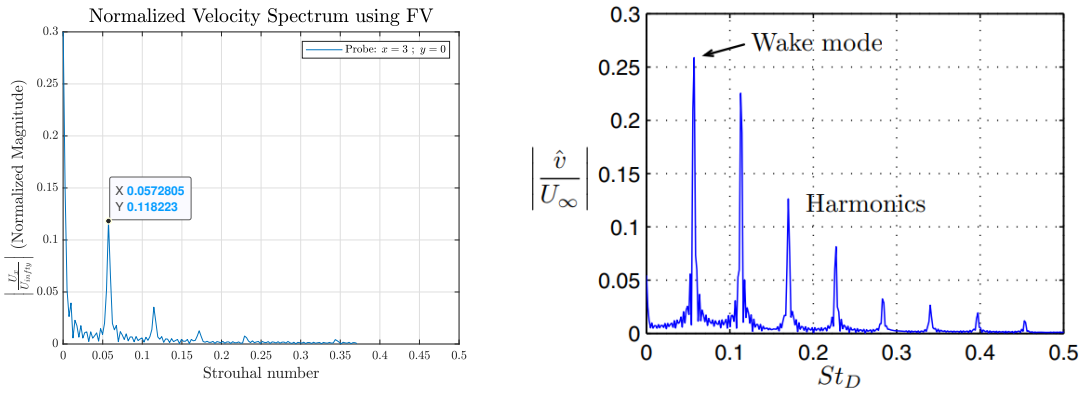

Figure 4.13: *FFT spectrum comparison between the one obtained using the IC3 solver (on the left) and the one obtained by Sun et al. [11] (on the right). It is possible to see the the Strouhal number that identifies the first harmonic is the same, although the magnitude changes. A possible cause could be a different way to perform the normalization of the spectra.*

As it is possible to see in the figure above and read in the article, the Strouhal number obtained for the shedding mode (from Sun called 'wake mode') is exactly $St = 0.0572$ which is very similar to the result obtained performing the FFT using IC3.

In order to have another confirmation of the results apart from the comparison with the paper, another script is written and used in order to determine the FFT on the whole domain, considering a weighting on the grid elements (*Figure* 4.14).
The script still determines the FFT but taking the U_x data of the whole field. As the first script does, the local average is removed in order to have a clearer peak finding. The difference here is that a volume weighting factor is applied to the FFT for each cell. This is useful considering that the mesh is not uniform: when the goal is to determine the magnitude of the FFT spectrum in the whole field it is mandatory to take into account the different elements sizes. The first script ignores this process because using the point probes inside the cavity there is no significant meaning in weighting the cells' contribution.

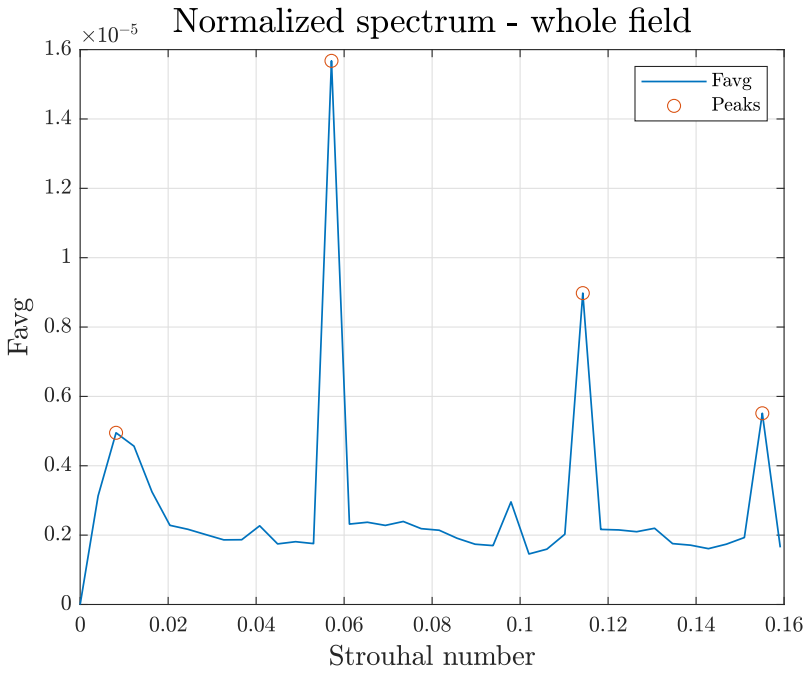

Figure 4.14: *FFT spectrum obtained using the data from the whole domain instead of a single point inside the cavity. In this case the magnitude of the frequency signal is weighted considering the volume of each mesh element.*

Using both scripts the results have not changed, and the first three harmonics are found at these values (*Table* 4.2):

$Re = 502;\ M = 0.6$		
Harmonics	$St\ [/]$	$f\ [Hz]$
I	0.05728	11.6983
II	0.114561	23.3968
III	0.17184	35.09529

Table 4.2: *Table containing the first three harmonics' Strouhal number and frequency in the FFT spectrum for a flow at $Re = 502$ and $M = 0.6$.*

The spectrum showed in this paragraph is determined using the flat top geometry, but it is discovered that the exact same result is obtained using the inclined top geometry (*Figure* 4.15). This means that the different boundary conditions do not alter the results, hence we are sufficiently far from the wall that the boundary conditions do not alter the system dynamics.

One of the goals of the study is to determine if there were any differences in the results applying the finite volumes method and the spectral differences. So different DNS simulations are run using the two numerical schemes, specifically using different degrees for the spectral differences interpolating polynomial.

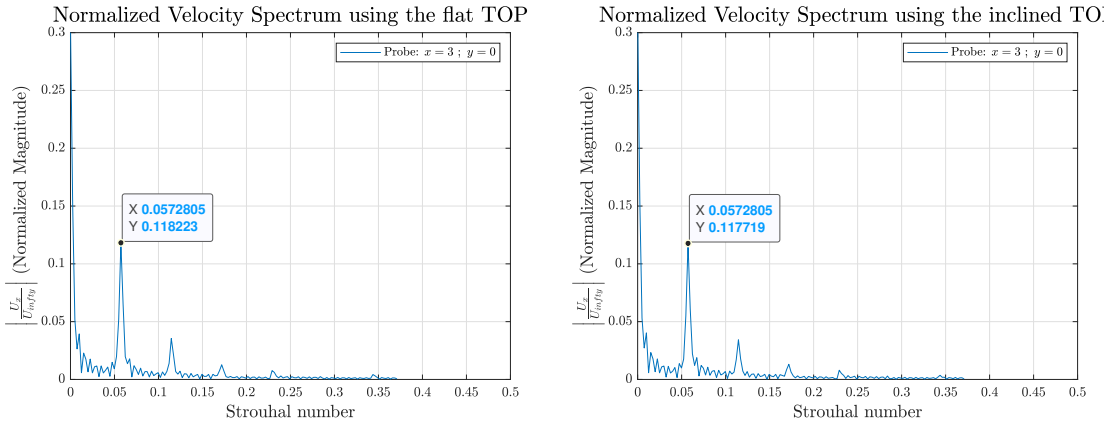

Figure 4.15: *FFT spectrum comparison between the one obtained using the flat TOP surface and the inclined one. As it is possible to see, there is no difference in the results obtained for the shedding frequency, hence we can consider the top surface to be as far as needed to not be influenced by the boundary condition applied.*

For the study to be valid it is mandatory to modify the grid in order to have the same amount of degrees of freedom. The dofs when using the spectral differences are associated to the number of solution points inside the single quad element, so it is necessary to create different meshes as the interpolating polynomial (equals to the solution point) changes.
The results are showed for the SD2 method, so using two interpolation point in each element. This configuration appeares to be the less performing giving the worst results between the different cases that is studied. The mesh adopted is the one showed in *Figure* 4.16.

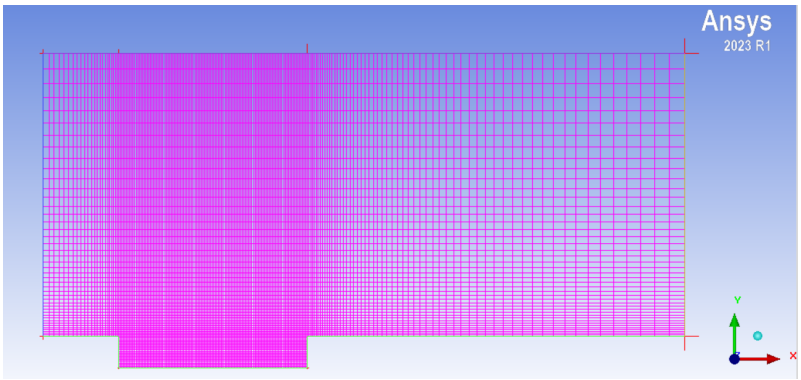

Figure 4.16: *Mesh used for the comparison between the SD2 method and finite volumes. The new mesh is necessary to have the same amount of degrees of freedom of the mesh created to apply finite volumes. The degrees of freedom are associated to the solution points inside the single elements, so comparing FV and SD2 elements there is a ratio of dofs of 1:4.*

The results are showed in *Figure* 4.17. Here we can notice some small differences in the shedding frequency. The one depicted on the right in the picture is the SD2 method, the one that gave the worst results. Considering that this is the worst case scenario showing the biggest difference in the obtained shedding frequency, we can still be satisfied.

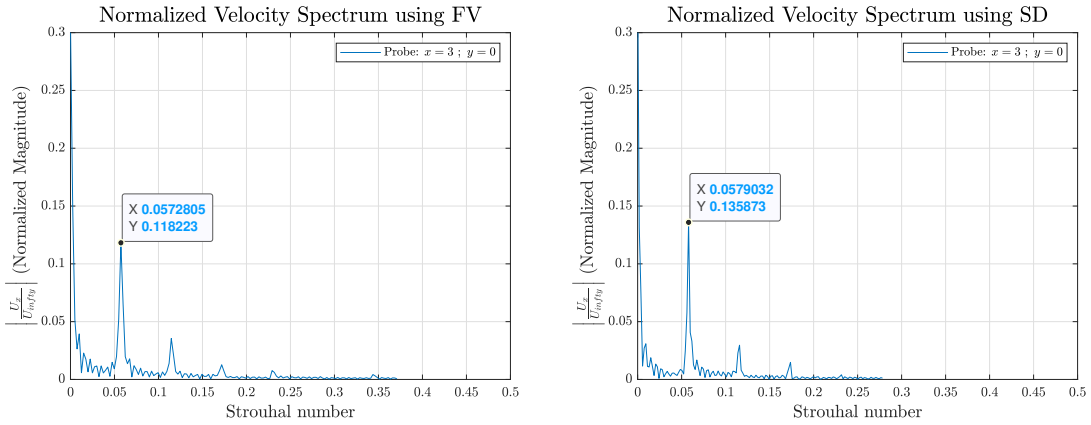

Figure 4.17: *FFT spectrum comparison between the one obtained using the finite volumes method and the spectral differences SD2. As we can see in this case we have some small differences in the results of the order of $\Delta St_D = 6e^{-4}$. This difference is reduced by increasing the order of the interpolating polynomial of the spectral difference method from SD2 to SD5. Please remember that applying the spectral difference method is convenient in cases where high numerical robustness is needed, but in terms of simulation time it is not. Even if we will bring this comparison further, there is a neat convenience of applying the finite volume method in this study.*

The difference is of the order of $\Delta St_D = 6e^{-4}$.

It is fundamental to know the shedding frequency for executing the stability analysis, whose aim is to identify the mode responsible for this phenomena.

4.4 Stability analysis

As deeply explained, the goal of this thesis' work is to execute a global stability analysis on an open cavity flow at $Re = 502$ and $M = 0.6$.
Repeating in a more detailed fashion, we aspire to execute a modal analysis (considering a stationary base flow and finding the modes that will amplify/damp the perturbations inside it for $t \to \infty$) without considering any symmetry in the flow i.e. performing a tri-global stability analysis.
We apply the small perturbation theory so that (as explained in details in *Chapter* 2):

$$\mathbf{q} = \mathbf{Q} + \epsilon \mathbf{q}' \tag{4.5}$$

where $\mathbf{Q} = Q(\mathbf{x})$ is the state vector representing the stationary base flow, ϵ represent the (small) amplitude of the perturbation $\mathbf{q}'$.
Given that we perform a global stability analysis the perturbation form simply is:

$$\mathbf{q}' = \mathbf{q}'(\mathbf{x}, t) = \mathbf{q}'(x, y, t) = \hat{\mathbf{q}}(\mathbf{x})e^{\omega t} = \hat{\mathbf{q}}(x, y)e^{\omega t} \tag{4.6}$$

where the exponential temporal evolution of the perturbation is possible due to the assumption of modal analysis. Note that ω is complex.
To determine the modes that make the base flow stable or unstable, we solve the eigenvalue problem:

$$\omega_j \hat{\mathbf{q}}(\mathbf{x}) = \mathcal{L}\hat{\mathbf{q}}(\mathbf{x}) \tag{4.7}$$

It was explained that determining the eigenvalues of the linear operator can be expensive, so the matrix-free techniques (Krylov-Schur in particular) are applied to find the eigenvalues of the matrix propagator $\mathcal{M}$.

Please note that we do not suppose the presence of symmetries in the flow, hence it doesn't really make sense to talk about a dispersion relation. For the sake of the completeness of the following analyses, we also do a step backwards to a pseudo-local approach determining the dispersion relation and studying the medium to determine if is either dispersive or non-dispersive.
Subsequently we determine the limit cycle to visually examine whether we are close to the threshold that corresponds to the primary mode or not.

4.4.1 Base flow determination using SFD

The first step to achieve to run a full stability analysis is to obtain the steady base flow.
Until now, the DNS were performed to discover the shedding frequency, which is the phenomena that disturb the base flow making it unstable.
The goal of this paragraph is to explain how the base state $\mathbf{Q}$ is determined. What it is done, is basically applying a low-pass filter to the flow. This technique is called *Selective Frequency Damping (SFD)* (Åkervik et al. [33], Casacuberta et al. [34]).
As stated in [33], if we consider a generic non-linear system:

$$\dot{\mathbf{q}} = f(q) \tag{4.8}$$

where the $\dot{}$ denotes the derivative with respect to time and $f(q)$ is an operator, then the steady state q_s is given by $\dot{q_s} = f(q_s) = 0$. If the operator is unstable, then any $q \neq q_s$ will depart from the base state quite quickly. The method used to stabilize the system is to apply a regularization technique, basically adding a linear term to the right-hand side of 4.8 forcing the system towards a *target solution* w. The linear term is:

$$-\chi(q - w) \tag{4.9}$$

where χ is the so-called *control coefficient*, in the future also called *gain*.
The target solution is of course the steady state solution q_s, but as we previously said this is not known a priori. The chosen target solution is then a modified q with a reduction in the temporal fluctuations. At this point, the low pass filter is applied, and the new target solution is:

$$w = T * q \tag{4.10}$$

that is, the convolution between the temporal filter T and the state q:

$$(T * q)(t) = \int_{-\infty}^{\infty} T(t - \tau)\ q(\tau) d\tau \tag{4.11}$$

For the method to converge to the steady solution, the filter cutoff frequency should be lower than that of the instabilities. Here is why it is fundamental to define the frequency of the shedding instability from the frequency spectrum.
As in [33], the modified system becomes:

$$\dot{q} = f(q) - \chi(I - T) * q \tag{4.12}$$

where I is the identity operator. For further explanations the reader is redirected to [33].

It is now in our interest to apply this technique to our fluid dynamic case. As stated in Åkervik et al. [33] and Rolandi [13], when a temporal filter is applied in the NS equations the system becomes:

$$\begin{aligned} \frac{\partial \mathbf{q}}{\partial t} &= \mathcal{N}(\mathbf{q}) - \chi(\mathbf{q} - \bar{\mathbf{q}}) \\ \frac{\partial \bar{\mathbf{q}}}{\partial t} &= \frac{\mathbf{q} - \bar{\mathbf{q}}}{\Delta} \end{aligned} \tag{4.13}$$

where this time we define $\bar{\mathbf{q}}$ as the approximation of the unknown steady state solution, while χ and Δ are respectively the *gain* and the *filter's width*. The target solution is the exact steady state solution $\bar{\mathbf{q}}_0$ (so that $\mathcal{N}(\bar{\mathbf{q}}_0) = 0$), towards which $\mathbf{q}$ and $\bar{\mathbf{q}}$ converge. The convergence towards the steady state is determined by the choice of the two parameters Δ and χ. The steady state is obtained when the most unstable eigenvalue of the modified system 4.13 is stable, so when its real part is negative. Again, in Åkervik et al. [33] it is possible to see how the most unstable eigenvalue is related to the two parameters Δ and χ, whose choice is fundamental for convergence. Basically the SFD method determines an approximation of the most unstable eigenvalue. Some criteria for the first choice of these parameters are showed by Akervik. First it is necessary to determine the cutoff frequency of the unstable disturbances:

$$f_c = \frac{1}{\Delta} \leq f_n \tag{4.14}$$

where f_c is the cutoff frequency that should be equal or smaller than the *natural frequency* of the instability.
For what concerns the gain parameter, Åkervik et al. [33] state that it should be at least:

$$\chi > \Re(\omega) \tag{4.15}$$

It has to be said that Akervik was one of the first to propose the Selective Frequency Damping method, and many other studies have been conducted to determine the best fit for these two parameters but without discovering any general (and at the same time accurate) criteria.
The parameters that are chosen as input for the IC3 solver are the ones in *Table* 4.3:

Cutoff frequency f_c $[Hz]$	Δ $[s]$	χ $[Hz]$
11.6983	0.085602	20

Table 4.3: *Table containing the values of the parameters χ and Δ of the SFD method. The gain (χ) is the parameter that turns the approximated most unstable eigenvalue stable, while Δ is the filter width.*

Until now the convergence criteria was not defined. In order to determine if the steady state had been found, the *residuals* are monitored. Residuals are indicators of the numerical error between the left and right hand sides of the equations. This

is usually called the *imbalance* of the equations. The residuals are automatically determined by the solver for the mass balance equation (density Rho), the continuity equation along the three axis ($RhoU_x$, $RhoU_y$, $RhoU_z$) and the energy equation ($RhoE$). When the absolute residuals (without any form of normalization) reach a value of $\approx 10^{-8}$ or lower, convergenc is obtained (and the steady state consequently). As showed in *Figure* 4.18 using the SFD parameters defined in *Table* 4.3 convergence is reached:

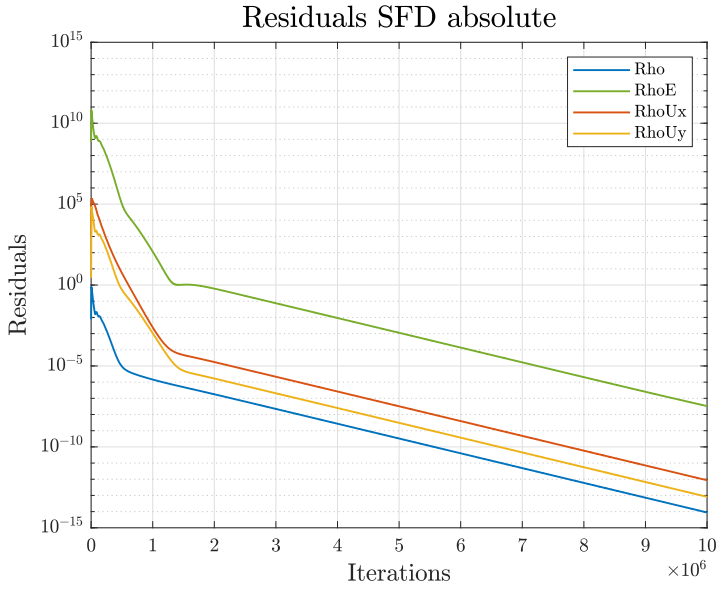

Figure 4.18: *Absolute residuals of the SFD analysis run. Given that the residuals have reached a value of* $\approx 10^{-8}$ *or lower, the base state is considered obtained.*

For a visual, further confirm that the base state had been achieved, the streamlines of the base flow are plotted and qualitatively compared to the base flow found by Sun (*Figure* 4.19):

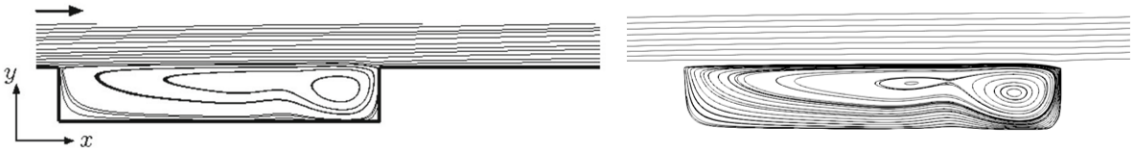

Figure 4.19: *Qualitative comparison between the velocity streamlines obtained for the base flow by Sun et al. [11] (left) and obtained applying the SFD using the parameters in Table 4.3 in the IC3 solver (right).*

Please note that the base flow also represents the fixed point of the system, so in the phase space it would be defined by a point. The perturbations are applied to this fixed point.

The study of the differences in the results using the finite volumes method and the spectral differences is carried on to this point. To examine the differences in the results, the semi-logarithmic plot of the streamwise velocity U_x, the density ρ and the total energy E were obtained (*Figure* 4.20).

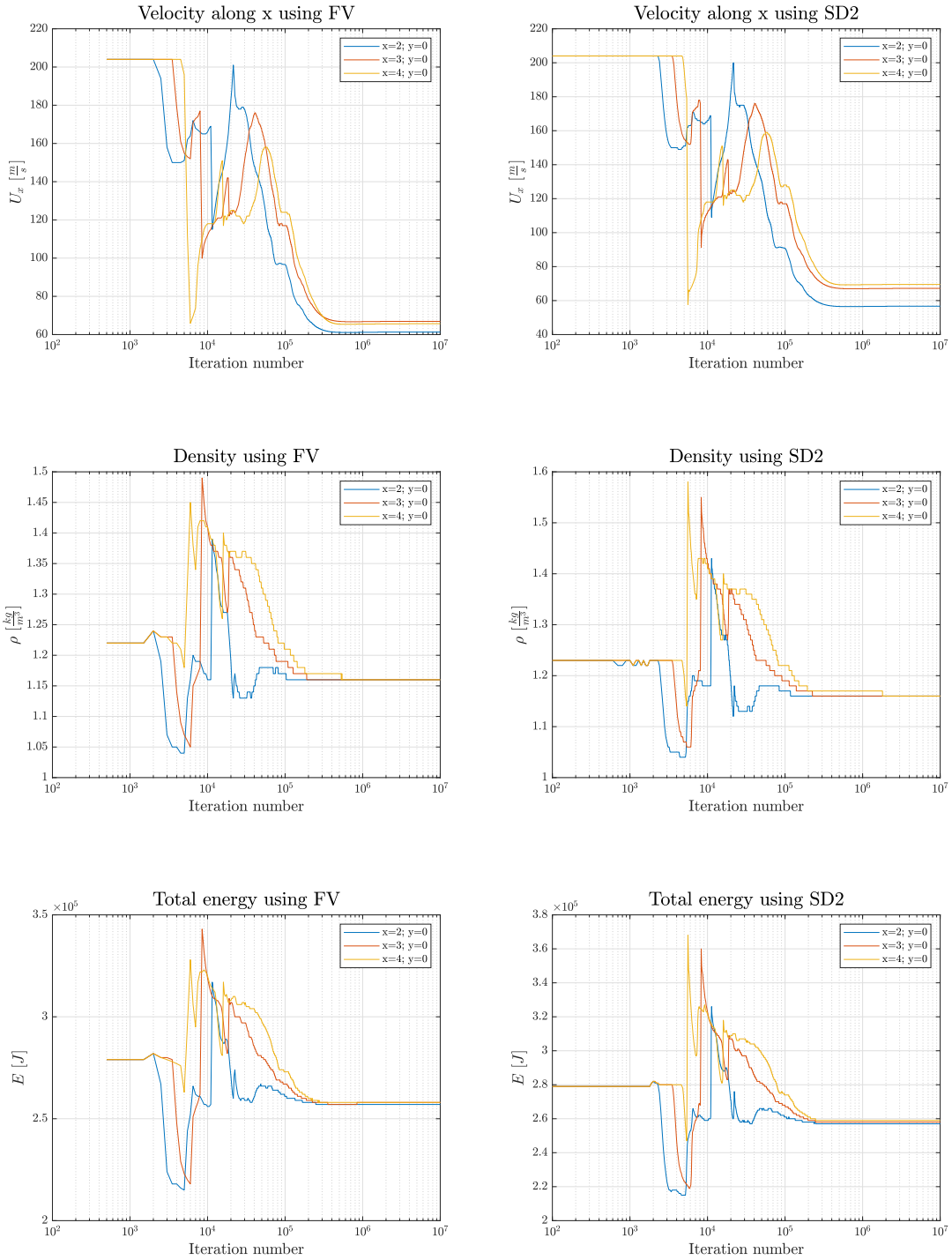

Figure 4.20: *Semi-logarithmic plot of the streamwise velocity U_x, the density ρ and the total energy E using finite volumes and spectral differences to obtain the base flow. It is possible to see that there are some slight differences, probably due to the differences in the input files of the simulations. The base flow is obtained using the selective frequency damping and imposing a cutoff frequency, equals to $f_{cutoff} = 11.6\ Hz$ for the FV case and equal to $f_{cutoff} = 12\ Hz$ for the SD2 one. Even considering the small differences, we obtain convergence approximately after the same amount of iterations and to very similar values.*

We can notice that there are a few differences in the plots, probably given by the differences in the input files. In fact, the study that is conducted using the FV

adopted a cutoff frequency to use in the selective frequency damping method equal to $f_{cutoff} = 11.6\ Hz$, while the SD case adopted $f_{cutoff} = 12\ Hz$. Even considering these differences, the convergence is obtained after nearly the same amount of iterations ($\approx 5e^6$) and the maximum differences collected on U_x, ρ and E are respectively $\Delta U_x = 1.5\ \frac{m}{s}$, $\Delta\rho = 1e^{-4}\ \frac{kg}{m^3}$ and $\Delta E = 0\ J$ after this number of iterations.

4.4.2 Perturbation around the base flow

Once the base state is obtained, it is possible to use it as the fixed point around which the perturbation is applied. It was well explained how the stability analysis is performed without directly finding the eigenvalues of the linear operator, but applying the Krylov-Schur algorithm to determine the eigenvalues of the exponential propagator $\mathcal{M} = e^{\mathcal{L}t}$. From the analytic solution we have:

$$\mathbf{q}'(\tau) = \mathcal{M}\mathbf{q}'(0) \tag{4.16}$$

where the product $\mathcal{M}\mathbf{q}'$ corresponds to the perturbation at a certain time $t = \tau$. The IC3 solver uses Chiba's method, in which the product $\mathcal{M}\mathbf{q}'$ is approximated by:

$$\mathcal{M}\mathbf{q}' = \frac{\mathbf{q}_+^\tau - \mathbf{q}_-^\tau}{2\epsilon} \tag{4.17}$$

where $\mathbf{q}_+^\tau$ and $\mathbf{q}_-^\tau$ are the DNS solutions that correspond to the initial conditions $(\mathbf{Q} + \epsilon\mathbf{q}')$ and $(\mathbf{Q} - \epsilon\mathbf{q}')$ integrated until the time τ. In conclusion, as explained in a detailed fashion in paragraph 2.4.5, a Floquet analysis using time stepping exponential transformation is used here. The IC3 solver implements this type of analysis, having in this case to set two different parameters that are ϵ and τ. The first one (ϵ) is the finite difference parameter used in Chiba's method, and has to be large enough to avoid numerical round-off errors but not too large to prevent non-linear effects. As suggested by Fosas De Pando, Sipp, and Schmid [35], $\epsilon \in [10^{-8}; 10^{-5}]$. Running different tests, the value of $\epsilon = 10^{-7}$ turns out to be appropriate.
For what concerns the parameter τ, it represents (conceptually) the time that the perturbation would need to be convected out of the domain. It is usually better to use a fraction of the oscillation period of the primary instability mode, and in this case it is tuned to be $\tau = 0.008\ [s]$.

Running the analysis the solver automatically creates a MATLAB script where the propagator eigenvalues (μ) are showed. Using the relation between the linear operator and the propagator we have:

$$\hat{\mathbf{q}}_{\mathcal{L}} = \hat{\mathbf{q}}_{\mathcal{M}} \tag{4.18}$$

and the eigenvalues of the linearized operator are simply obtained as:

$$\omega = \frac{\log|\mu| + i\ arg(\mu)}{\tau} \tag{4.19}$$

For the sake of simplicity we define:

$$\omega = \Re(\omega) + i\Im(\omega) = \omega_r + i\omega_i \tag{4.20}$$

where, for the perturbation form adopted in 4.6, ω_r represents the temporal growth rate and ω_i the frequency. In the following, the eigenvalues are made non-dimensional:

$$\omega_r^* = \frac{\omega_r \cdot D}{U_\infty} \tag{4.21}$$

$$\omega_i^* = St_D \tag{4.22}$$

Running the IC3 solver the stability analysis is performed and the spectra is obtained (*Figure* 4.21):

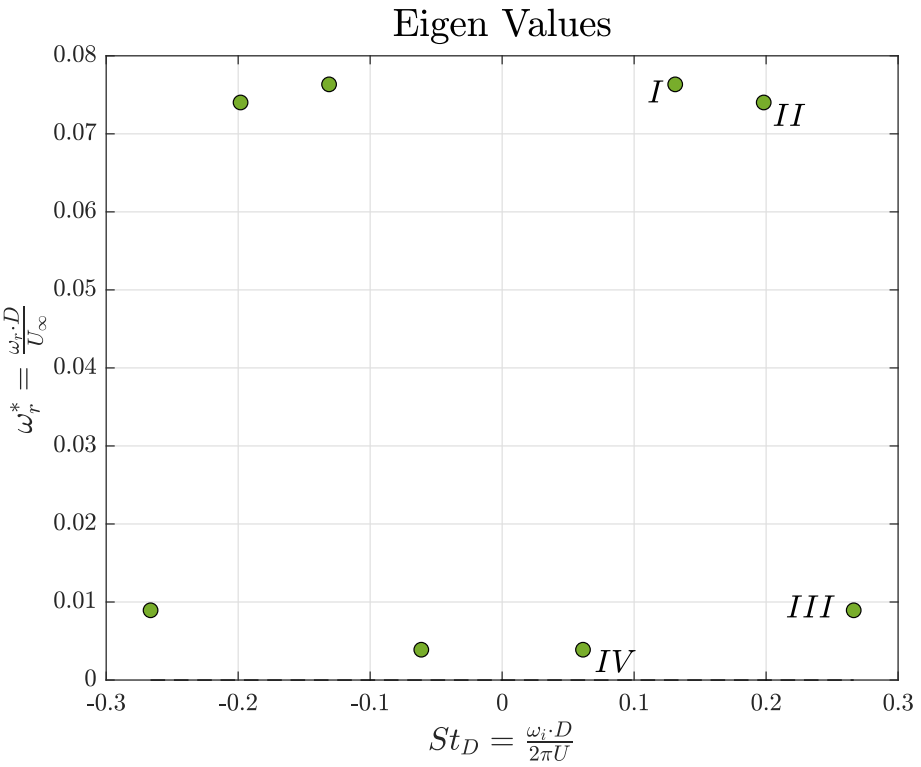

Figure 4.21: *Eigenvalues determined by the IC3 solver using the Chiba method. It is possible to determine the most amplified mode looking at the growth rate (ω_r^*) of the different eigenvalues. The most amplified mode is the one referred to the shedding instability.*

Showing the values determined for each mode (named from I to IV from the most to the least amplified), it is reasonable to do the comparison with the modes obtained by Sun et al. [11] (*Table* 4.4 and *Figure* 4.22):

$(\omega_r D/U_\infty) + i\ St_D$		
Mode	**Sun et al.**	**IC3 solver**
I	$+0.0808 + 0.1307i$	$+0.0763 + 0.1311i$
II	$+0.0685 + 0.1959i$	$+0.0740 + 0.1982i$
III	$-0.0049 + 0.2624i$	$+0.0089 + 0.2663i$
IV	$-0.0002 + 0.0636i$	$+0.0039 + 0.0613i$

Table 4.4: *Table showing the comparison between the eigenvalues determined by Sun et al. and the ones determined doing a stability analysis on IC3 perturbing the base flow. The eigenvalues are listed from I to IV going from the most amplified mode (that represents the shedding mode) to the least amplified one. It is possible to see that there are some differences in the results. These can be related to a slight difference in the boundary layer momentum thickness θ.*

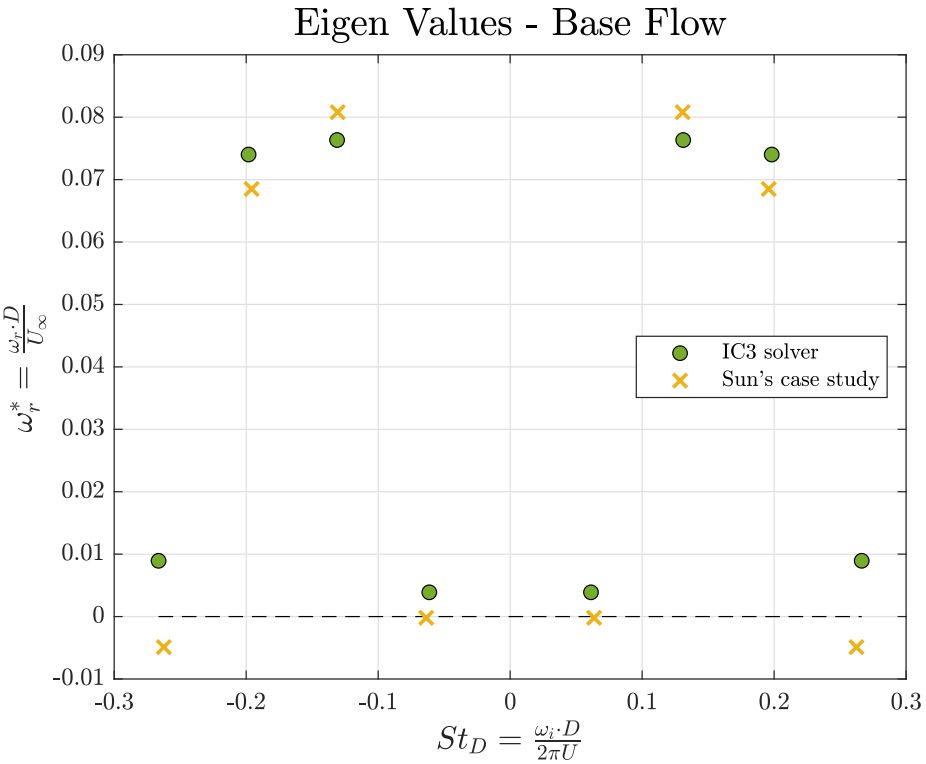

Figure 4.22: *Figure showing the comparison between the eigenvalues determined by the IC3 solver (green dots) and the ones determined by Sun et al. (yellow crosses). It is possible to see that there is a slight difference in growth rates, probably caused by a difference in the boundary layer momentum thickness θ.*

It is evident that there are some differences in the growth rates. In particular, using the IC3 solver it appears that every mode is amplified given that $\omega_r^* > 0$ for each one of them. In order to explain this differences some further examinations are executed.

Firstly, a validation of the results obtained by the IC3 solver is investigated. A DNS simulation is run using the base flow as the input state for the flow. Although no initial perturbation is imposed, given that the base flow is unstable (as there is at least an amplified mode), some numerical errors automatically disturb the flow

and act as initial perturbation. It is then possible to visualize the evolution of the perturbation until the non-linear interactions become significant and the perturbation reaches its saturation. The results of the DNS simulation is showed in *Figure* 4.23:

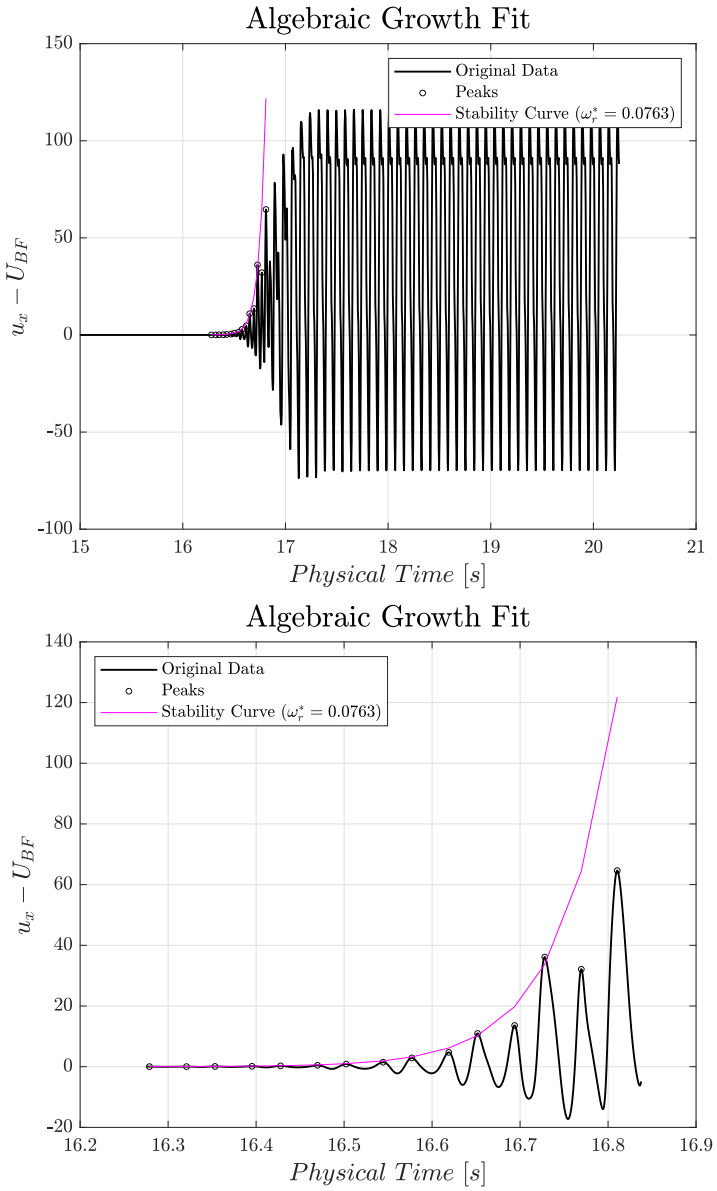

Figure 4.23: *Representation of the algebraic growth valid for the linear behaviour of the perturbations. The aim of this study is to validate the results obtained from the stability analysis. In this case, an exponential fit curve of the type $e^{\omega_r^* t}$ (coloured in magenta in the pictures) is superimposed on the signal in order to see if the growth rate of the most amplified mode is capturing the evolution efficiently: the results seem valid.*

Using in this case an exponential fit curve (in magenta) that interpolated the peaks in the signal, a growth rate of $\omega_r^* = 0.0763$ is obtained, confirming the value found in the spectrum (look at *Table* 4.4) for the most amplified mode. Once the coherence in the results obtained using IC3 is confirmed, a further analysis on the possible reason that causes the differences between our case and Sun et al.' s one is conducted.
Checking the parameters from the beginning of the study, it is discovered a difference

in the momentum boundary layer thickness θ, probably due to differences in the wall model. Between the growth rate of the most amplified mode and the momentum boundary layer thickness exists a relation (Brès and Colonius [28]):

$$\omega_r \propto \frac{U}{\theta} \tag{4.23}$$

In Sun et al.'s work [11] it is said that the ratio $\frac{D}{\theta} = 26.4$ at the leading edge of the cavity. Using some fictitious probes to analyse in better details the boundary layer at the upstream edge of the cavity, it is possible to determine this ratio, equal to $\frac{D}{\theta} = 23.4546$, causing the growth rate to be lower than in Sun case (*Figure* 4.24).

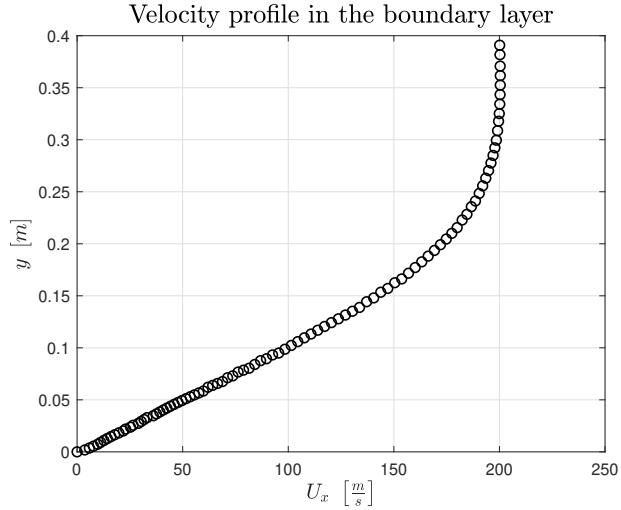

Figure 4.24: *Graph showing the velocity profile U_x in correspondence of the upstream edge of the cavity. In order to determine the momentum boundary layer thickness, the integral quantity is determined considering the end of the boundary layer as the y coordinate where $U_x = 0.99U_\infty$.*

In the end, as proposed by Sun et al., the visualization of the modes (I, II, IV) of the real part of $\hat{U}_x$ is represented for a symmetric interval, bringing a visual comparison of the modes (*Figure* 4.25):

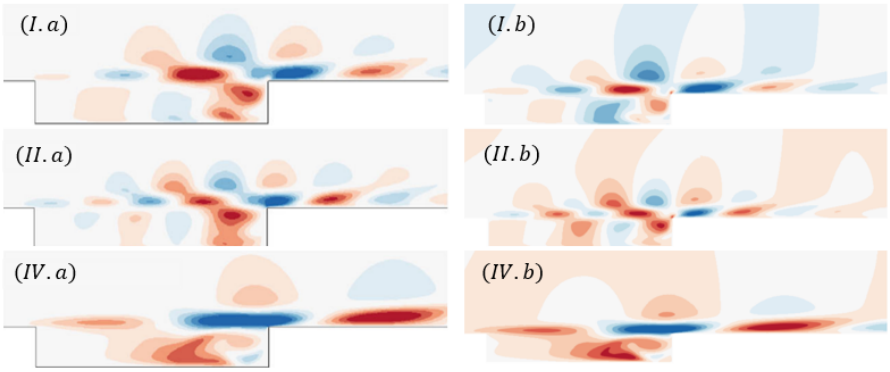

Figure 4.25: *Contours of the real part of $\hat{U}_x$ of the eigenvectors of the modes I, II, IV. In particular the contours of $\frac{\hat{U}_x}{U_\infty} \in [-0.008, 0.008]$ are showed for Sun et al.'s results $(I(a), II(a), IV(a))$ [11] and the IC3 ones $(I(b), II(b), IV(b))$.*

As it is possible to see, the mode representation is very similar between the paper's and the IC3 results.

Again, the results are the same for the two geometries of the domain, underlying that the two different boundary conditions are not influencing the results and that the top boundary is sufficiently far from the cavity.

4.4.3 Dispersion relation

As it has been said multiple times in the course of this report, the goal of the thesis work is to execute a global stability analysis on an open cavity flow, without assuming any symmetry in the flow, i.e. considering a flow without homogeneity directions. In this case the perturbation form is the one in 4.6.
However, it is considered interesting to do a step back and evaluate whether the medium is dispersive or not, executing a fictitious local analysis. We repeat that in a dispersive medium the waves speed depends on their frequency. In order to do this analysis, the four modes determined are used. From the visualizations also proposed in *Figure* 4.25, the values along a line in the shear layer are considered, determining how $\Re(\hat{U}_x)$ changes on this line (*Figure* 4.26).

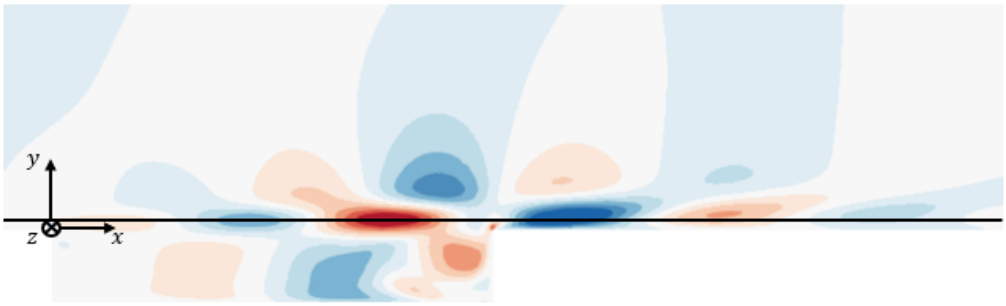

Figure 4.26: *Scheme of the line along the streamwise direction that is used to determine the wave numbers of the four different modes.*

Given that the spatial periodicity is quite evident in the visualization of $\Re(\hat{U}_x)$, it is considered a great choice to use this quantity in particular.
A spatial FFT is performed on the signal to determine the dominant wave number, which is the one corresponding to the greatest peak in the FFT (*Figure* 4.27).

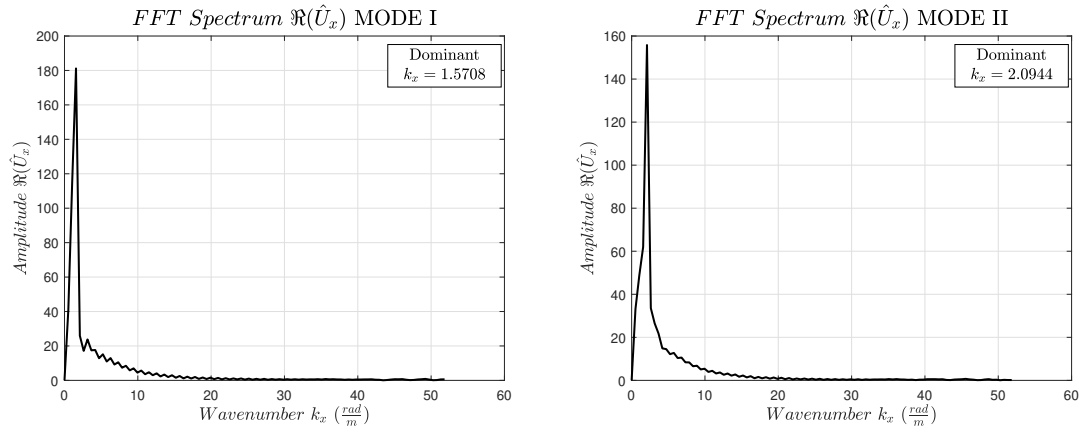

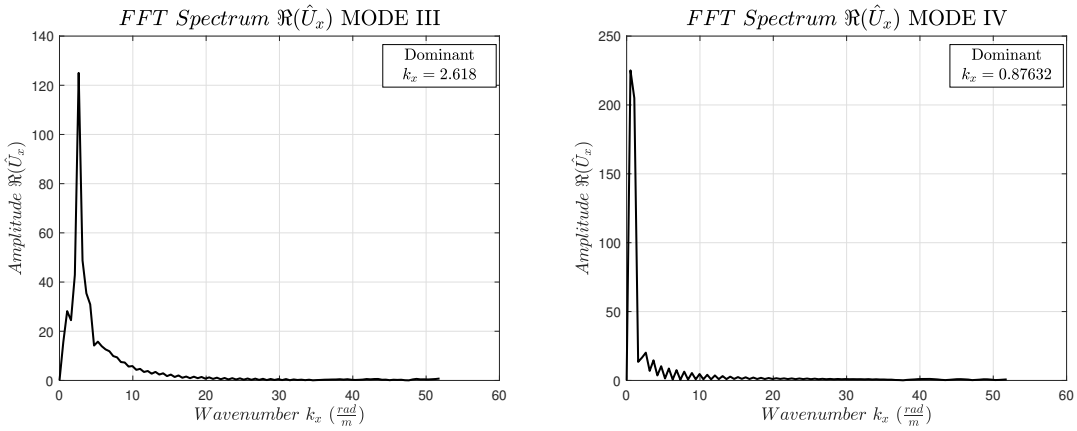

Figure 4.27: *The spatial FFT is executed on the real part of $\hat{U}_x$ to determine the dominant α of the four modes. The different wave numbers are collected in Table 4.5.*

From the analysis of the wave it is possible to determine the wave numbers of the modes, and of course the different wave lengths.
The results obtained for the wave numbers and wave lengths are written in *Table* 4.5:

Mode	**Wave number** α $\left[\frac{rad}{m}\right]$	**Wave length** λ $[m]$
I	1.57080	4.0
II	2.09440	3.0
III	2.61800	2.4
IV	0.87632	7.2

Table 4.5: *Table containing the dominant wave numbers and wave lengths for the four modes. They are determined applying a spatial FFT to the signal over a line inside the shear layer along the x direction.*

To have a qualitative validation of the wave numbers (and wave lengths) obtained, on the visualizations showed in *Figure* 4.25 a simple ruler is positioned and the wave lengths are obtained (*Figure* 4.28):

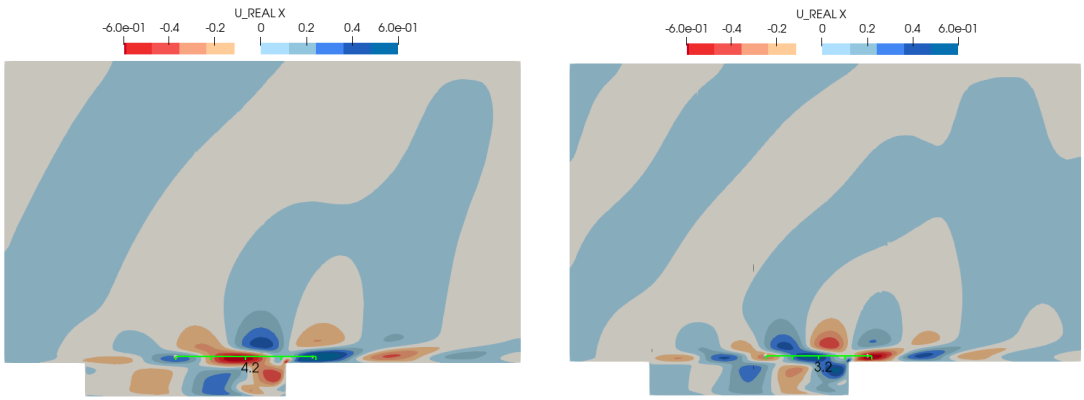

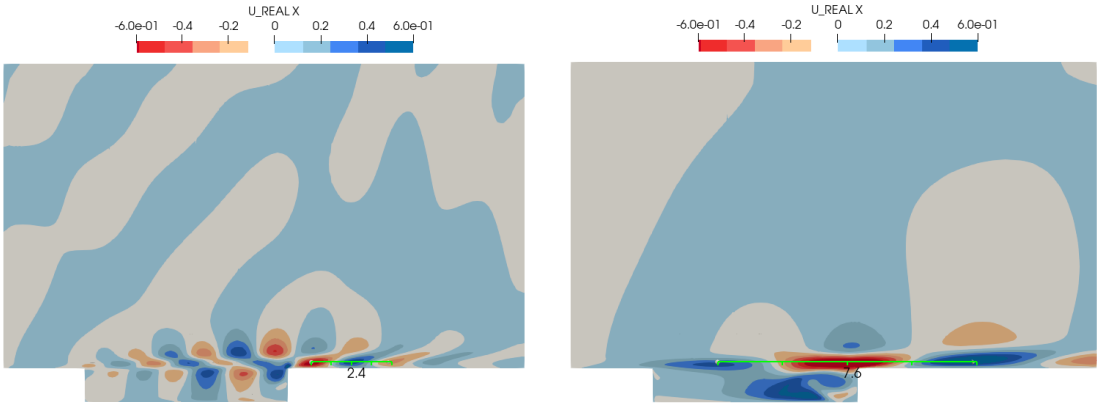

Figure 4.28: *Virtual rulers used to qualitatively visualize the wave lengths of the four modes.*

Note that the wave lengths determined qualitatively on the visualizations are very similar to the results of the FFT.

In order to further validate the results obtained here, the wavelengths have been compared to literature. First, the wavelengths obtained by Sun are again determined from the visualisations in *Figure* 4.25 by simply applying a virtual ruler on the images from [11] (*Figure* 4.29).

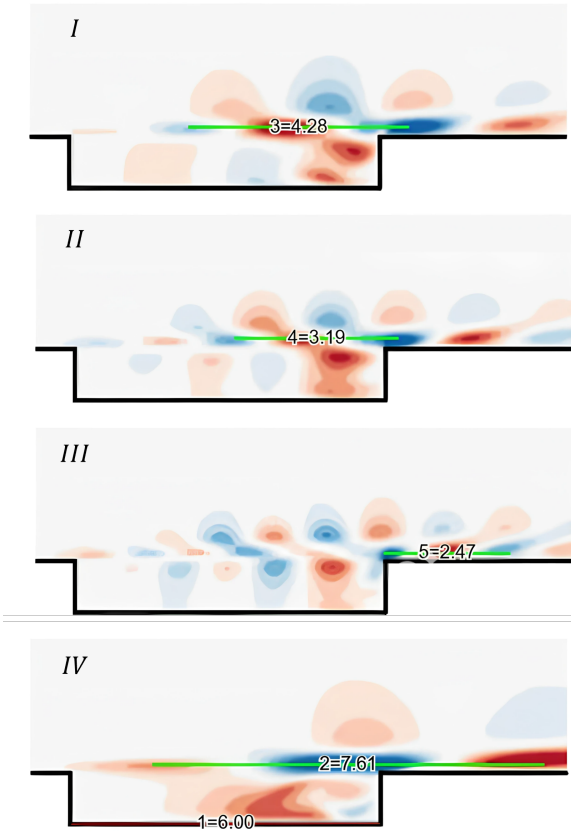

Figure 4.29: *Virtual ruler applied on the four most amplified modes from Sun et al. [11]. As we can see, the wavelengths are similar to the one identified in Figure 4.28. This is an additional validation of the results obtained.*

The results are also represented in *Table* 4.6:

Mode	**Wavelength** λ_{IC3} $[m]$	**Wave length** λ_{Sun} $[m]$
I	4.0	4.28
II	3.0	3.19
III	2.4	2.47
IV	7.2	7.61

Table 4.6: *Table containing the dominant wavelengths for the four modes obtained using IC3 and using a virtual ruler on Sun et al. [11] visualizations.*

The differences may be related to the low accuracy of the virtual ruler, given that it is difficult to identify the peaks in the visualizations. We still consider the results satisfactory.
A different comparison is done using the results obtained by Bailey, Abbá, and Tordella [30]. We are interested in visualizing the differences in the wavelengths when the control parameters change.
As previously stated, changing the parameters alters the dynamics of the flow. The comparison of the present work and the article is then done qualitatively. In particular, the parameters that change between the two studies are briefly summarized in *Table* 4.7:

Parameter	**Bailey, Abbá, and Tordella [30]**	**Present work**
Re	2900	800
M	$1e^{-3}$	0.6
$\frac{L}{D}$	4	6
$Topology$	$Confined\ flow$	$Open\ flow$

Table 4.7: *Table containing the parameters applied by Bailey, Abbá, and Tordella [30] for the evaluation of the acoustic standing wave and the parameters used in the present work. Please note that the Reynolds number is defined using the half height of the cavity in Bailey's work (equal to $2D$) while in the present work it is considered D as reference measure. Comparing the Reynolds numbers, this is the most similar case studied in this thesis to compare with Bailey's results.*

As presented in *Chapter* 3, Bailey, Abbá, and Tordella [30] determine the pressure field inside the cavity using an incompressible formulation fro the turbulent case at $Re = 2900$. In the article they demonstrate that using the incompressible formulation it is still possible to recognize a pattern resembling an acoustic wave generated by the impingement of the flow on the trailing edge of the cavity. Our case differs in terms of parameters and base flow. In particular we suppose that the greater aspect ratio and the fact that the flow is unconfined will make a great difference in the results. However, the acoustic wave caused by the impingement of the asymptotically dominant mode on the cavity wall can still be recognized qualitatively. The visual comparison is represented in *Figure* 4.30. A different colour map than usual is used to highlight the pressure peaks. Using a virtual ruler the wavelength is obtained.

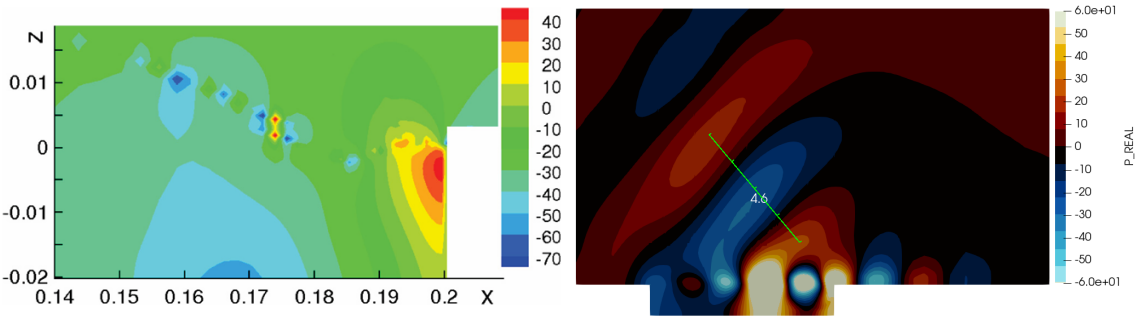

Figure 4.30: *Comparison between the acoustic wave visualizations obtained by Bailey, Abbá, and Tordella [30] (left) and using IC3 (right). The colour map is chosen to highlight the pressure spots. While Bailey et al. found a wavelength approximately equal to $\frac{1}{8}D$ the one obtained in IC3 is equal to $4.6D$. As we can see the differences are definitely not negligible. Due to the different aspect ratio, the perturbations in the present work have more time to be amplified by the shear layer, which has a great influence on the flow structures. Moreover, as an unconfined flow, the feedback acoustic mechanism altering the flow dynamics and the consequent acoustic footprint happens more slowly than in a confined flow, so we expect the wavelength to be greater. We can still see a similar direction of propagation and phenomena occurring.*

It is easily noticeable that the wavelengths differ greatly. As Bailey, Abbá, and Tordella [30] obtained a wavelength of the acoustic standing wave equal to $\frac{1}{8}D$ using IC3 this is equal to $4.6D$. This huge difference is considered to be a consequence of the different configurations: the Reynolds used from Bailey represents a turbulent case, while we are not sure that with the Reynolds obtained here the flow will transition to turbulence; the aspect ratio differs from $\frac{L}{D} = 4$ in [30] to $\frac{L}{D} = 6$ in the present work, making the flow more unstable and making it possible for the perturbations to amplify more; the flow is unconfined in the case studied here, so there is not the effect of the upper wall that accelerate the feedback aeroacoustic loop, resulting in a greater wavelength. Moreover, we are considering a two dimensional flow, thus neglecting the influence of three-dimensionality that, as we have explained, has a great influence on the flow dynamics. In conclusion, we may observe a difference in the angle of the acoustic wave compared to the one from Bailey, Abbá, and Tordella [30]: in the present work the reflection has an angle of approximately 130° while in the article it makes a 150° with the x-axis. This difference can be again related to the topology of the flow which is unconfined, and to compressibility.
A few words are spent on the Mach influence on the acoustic wave. Following the *Morkovin hypothesis* we may consider low effect on compressibility on boundary layers. In particular we may account for the differences between compressible turbulent boundary layers and incompressible boundary layers by incorporating the variations of mean fluid quantities, given that the dilatation effects are negligible. This hypothesis are said to be true when the Mach number is smaller than $M = 0.5$. Even if in the present work we do not have necessarily a turbulent flow, we may consider low effects of compressibility, although we will see in *Chapter* 5 that the eigenspectrum will change. In the meantime we consider this hypothesis to be valuable, so we represent also the visualization for $Re = 502$ and $M = 0.4$ (*Figure* 4.31).

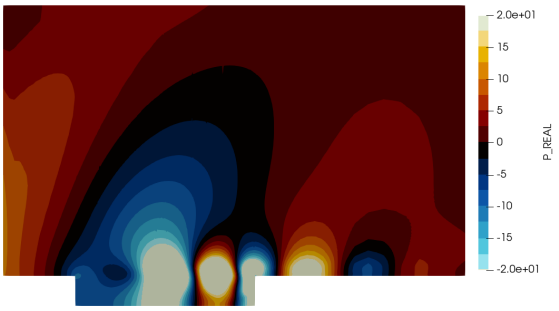

Figure 4.31: *Visualization of the pressure field of the dominant mode for the case at* $Re = 502$ *and* $M = 0.4$*. Although the acoustic wave is not so evident here, the angle appears to be greater compared to the one discovered for the* $Re = 800$ *and* $M = 0.6$ *case. This could be a consequence of compressibility.*

We can notice here that the angle of the backward moving acoustic wave (although not clearly visible) is greater then the one discovered for the $Re = 800$ and $M = 0.6$ case. This effect could be given by the lower effect of compressibility, in accordance to the Morkovin hypothesis.
We conclude this brief analysis of the acoustic wave's wavelength saying that the results show qualitative similarities to the one obtained by Sun et al. [26] and represented in *Figure 12* of their paper. Please keep in mind that in the present work the focus is on the hydrodynamic modes and not on the acoustic features of the cavity.

Once the wave number and wavelengths are obtained, the graphs of the real and imaginary parts of ω as functions of α (the wave number) are realized:

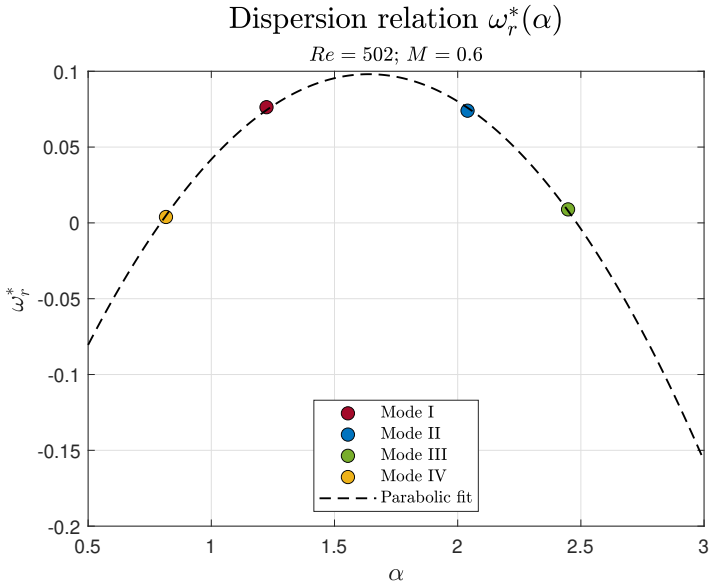

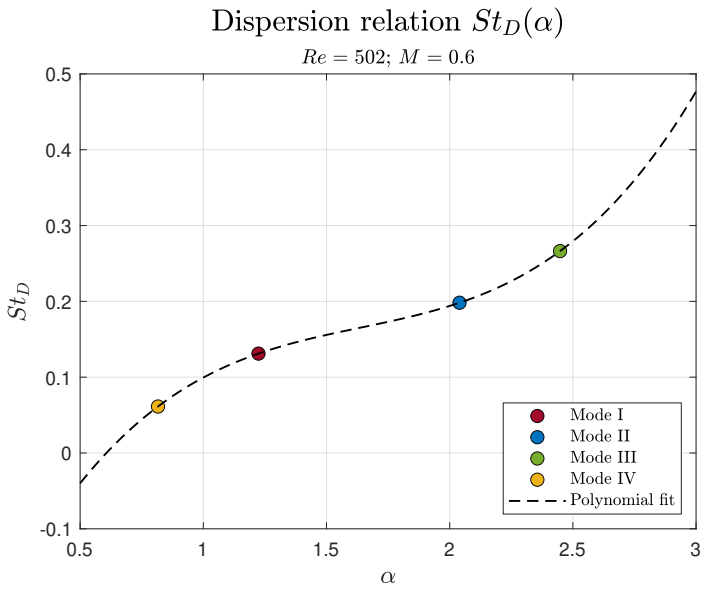

Figure 4.32: *Graphs representing the behaviour of the real and imaginary part of ω for different wave numbers. The four points represents the four modes found during the stability analysis, and the fit is added in order to find out whether the medium is dispersive or not. As it was explained in Paragraph 2.3.2, given that the imaginary part of ω shows a non-linear trend, we can already tell that the medium is dispersive.*

It is possible to compare the behaviour of the real part of ω to literature (Nastro et al. [36]) to consider the parabolic trend reasonable. Moreover, it is already possible to state that the medium is dispersive, given that the non-linear trend of $\Im(\omega)$ necessarily means that $v_\phi \neq v_g$.

4.4.4 Phase velocity

The subsequent part of the analyses aims to determine the phase velocities of the modes and show graphically the differences between them.
Firstly the phase velocities are determined as (*Table* 4.8):

$$v_\phi = \frac{\omega_i}{\alpha} = \frac{2\pi U_\infty St_D}{D\alpha} \tag{4.24}$$

Mode	$\omega_i \left[\frac{rad}{s}\right]$	$\alpha \left[\frac{rad}{m}\right]$	$v_\phi \left[\frac{m}{s}\right]$
I	168.2295	1.5708	107.0979
II	254.3332	2.0944	121.4349
III	341.7201	2.6180	130.5272
IV	78.6611	0.8763	89.7630

Table 4.8: *Phase velocities determined for the most amplified modes. It is evident that these four velocities are not equal, so the medium is dispersive as already stated.*

In order to display graphically the differences, a sinusoidal wave is used for each mode identified. For the sake of simplicity it is not considered the temporal growth,

given that the goal is to show the different phase velocities. Each wave represented is defined by the dominant wave number found for the corresponding mode, and the $\Im(\omega)$ is included using the phase velocities:

$$U' = A \cdot sin(\alpha x - \alpha v_\phi t) \tag{4.25}$$

where A is a constant amplitude applied in this simplified representation of the waves. Note that the phase velocities are scaled using mode one's phase velocity in order to appreciate in a better fashion the differences in the plots.
Starting from $t = 0$ we get (*Figure* 4.33):

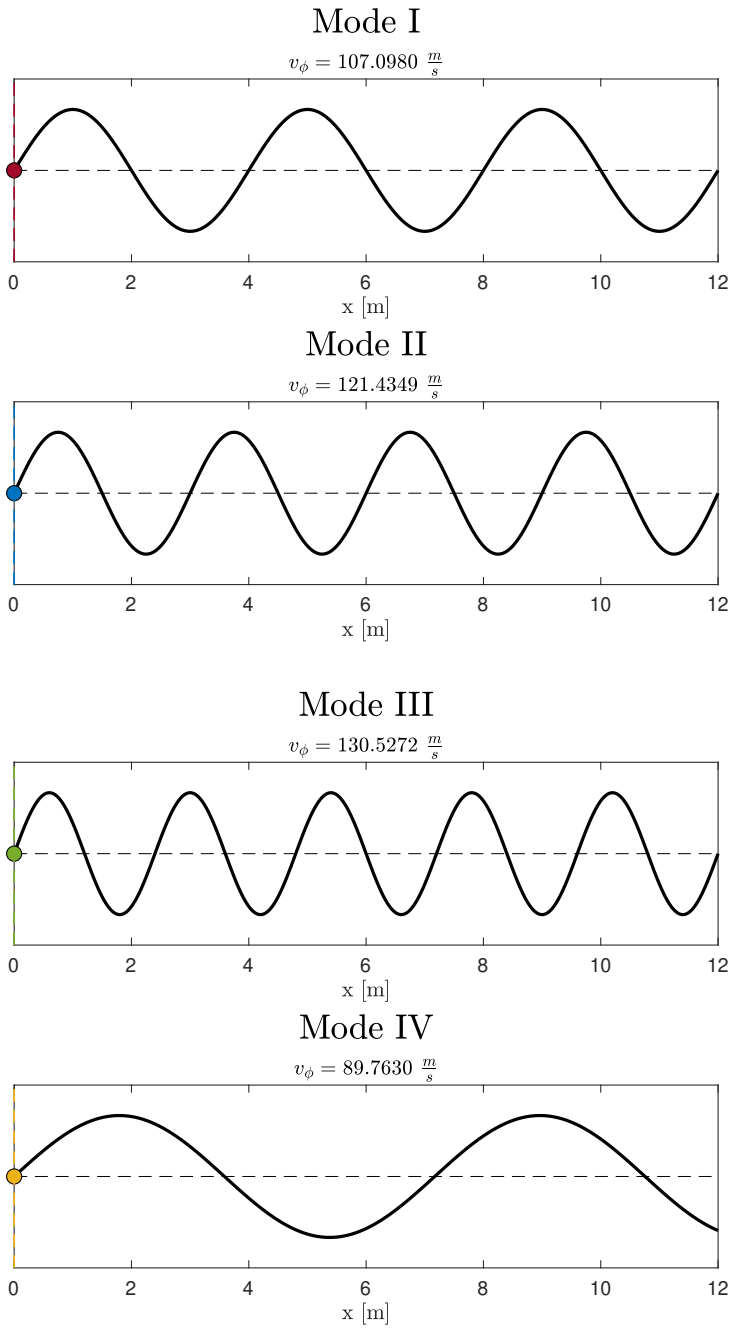

Figure 4.33: *Qualitative plots in order to see the differences in the phase velocities for the four unstable modes identified. Here it is represented a time $t = 0$.*

Where we can already appreciate the differences in the wave lengths of each mode. Looking at the situation after a certain time t_f we get (*Figure* 4.34):

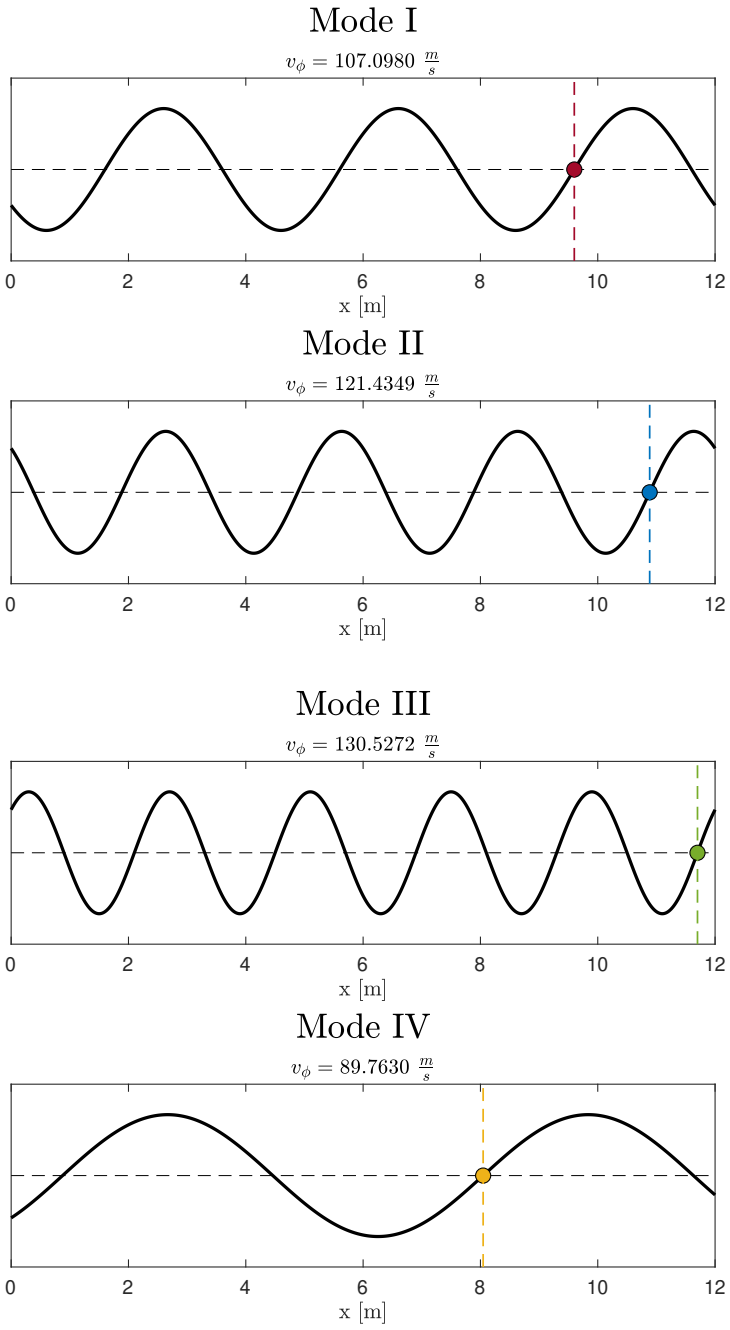

Figure 4.34: *Qualitative plots in order to see the differences in the phase velocities for the four unstable modes identified. Here it is represented a time $t = t_f$. Note that, as expected from the observation of Figure 4.32, the medium is dispersive given that the phase velocities are different from one another.*

A summarizing representation of the phase velocity and dispersion relation is presented in *Figure* 4.35:

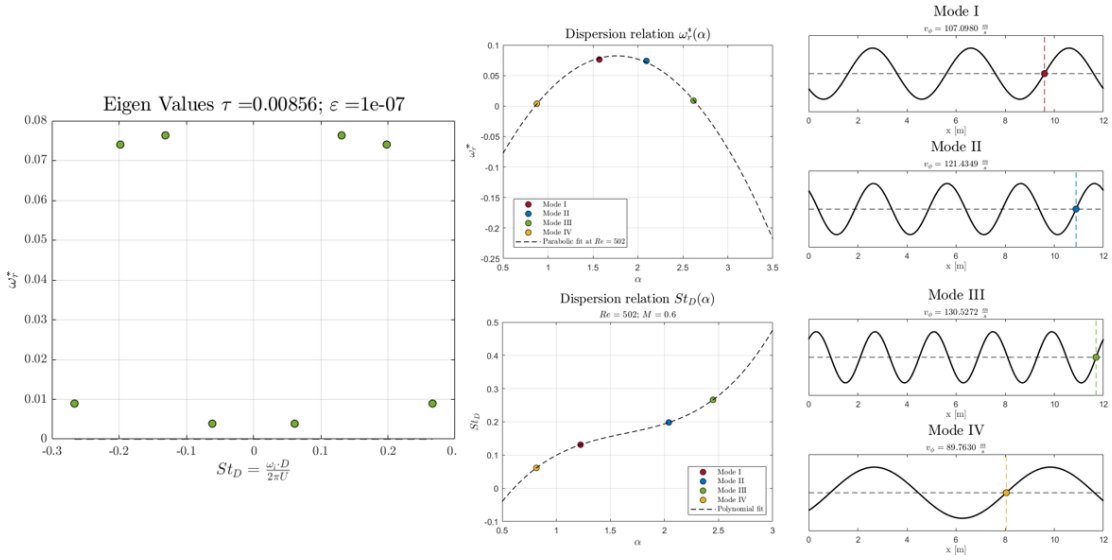

Figure 4.35: *Summarizing representation of the eigenspectrum (left), the relations $\omega_r^*(\alpha)$ and $St_D(\alpha)$ and the phase velocities of the different waves (right).*

4.4.5 Limit cycle

Going back to the study of global instabilities, it was explained in *paragraph* 2.4.2 that when a stable stationary system evolves to a periodic state due to a primary instability (as it happens for the wake behind a cylinder and the cavity analysed here), then a Hopf bifurcation has occurred. Even if until now we cannot determine the critic Reynolds at which the bifurcation occurs, if we section the phase plane $(\mathbf{q}, \dot{\mathbf{q}})$ for a determined Reynolds number ($Re = 502$ in this case), we can observe a stationary fixed point and a trajectory that brings us to the limit cycle. As it was said during the course of this thesis, both the fixed point and the limit cycle represent two attractors for the system i.e. two different equilibrium states.

It is then represented the limit cycle in the phase plane, specifically in the three-dimensional plane for the velocity signal u_x, so in the plane $(u, \dot{u}, \ddot{u})$. Again, the base flow is used as the input for a DNS simulation, where no perturbation other then the naturally present numerical one is added to the flow. Given that the base flow is unstable, even a numerical perturbation of amplitude $> 10^{-15}$ causes the instabilities to grow. After the perturbation reaches its saturation, that is, when the non-linear effects are not negligible any more and the growth is stopped, the trajectory starts to define the limit cycle, represented in *Figure* 4.36.
It is possible already to see that the limit cycle is far from a perfect ellipsoid, this meaning that we are far from the threshold of the marginal stability (the Re_{crit} has been surpassed already). This is further appreciable looking at the graph in the plane $(u, \dot{u})$ (*Figure* 4.37):

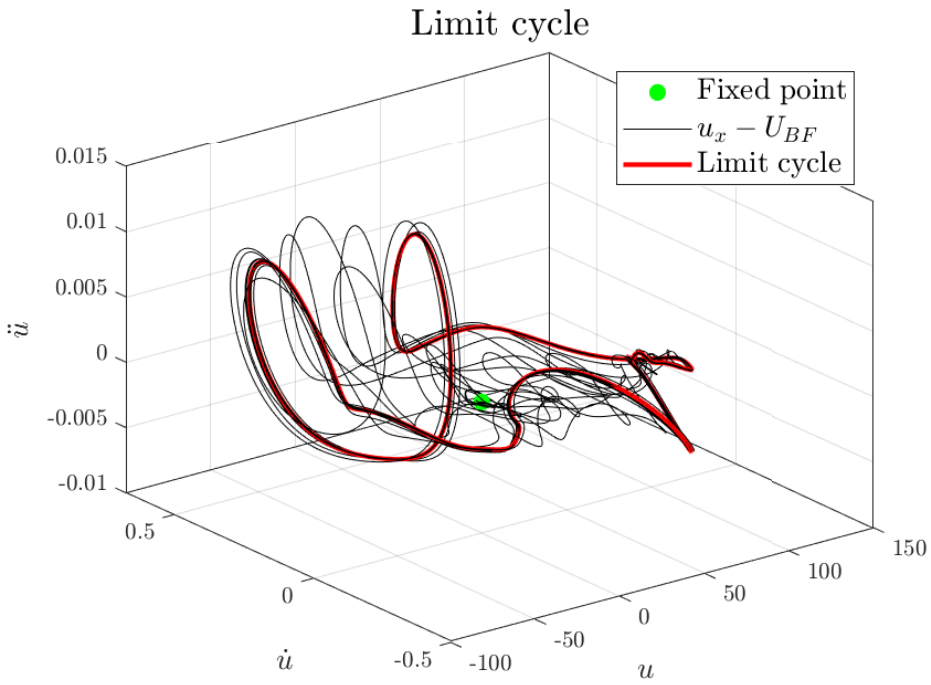

Figure 4.36: *Representation on the phase plane of the limit cycle, obtained perturbing the base flow (fixed point represented in green) until the perturbation reaches its saturation, and the non-linear effects become not negligible. In particular, it is considered the velocity signal u_x gotten from a virtual probe located in the middle of the cavity ($x = 3\ m$), to whom the base flow velocity is subtracted. When the perturbation's saturation is reached, then the limit cycle become evident (in red in the picture).*

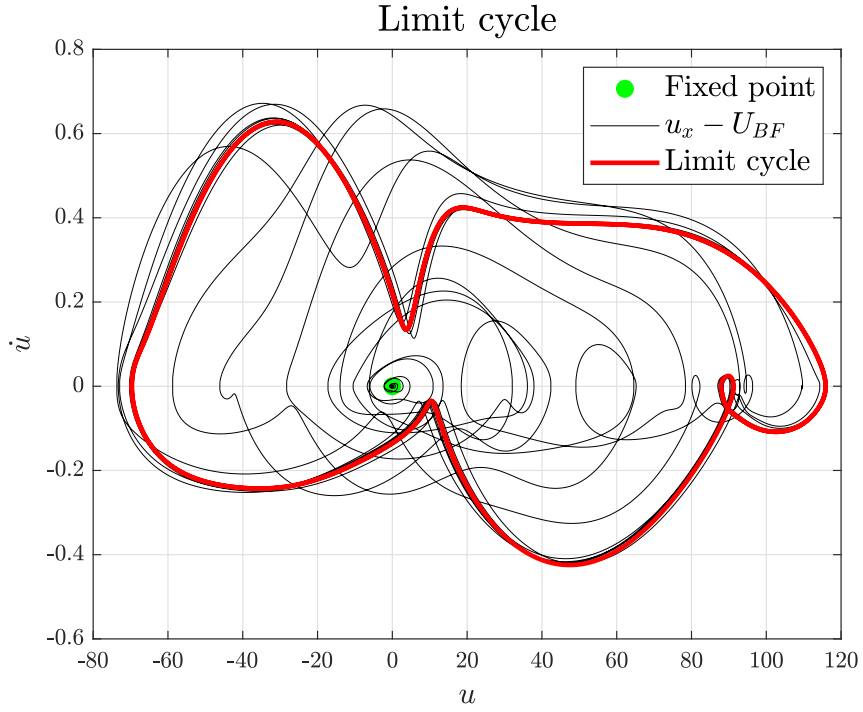

Figure 4.37: *Looking at the graph in the plane $(u, \dot{u})$ it is further appreciable that the limit cycle is far from a perfect ellipsoid. This means that the critic Reynolds number has been surpassed.*

Chapter 5

Influence of the Reynolds and Mach numbers

There are many articles and papers discussing the influence of specific parameters on open cavity flows (Brès and Colonius [28], Mathias and Medeiros [37], Rowley and Williams [2]), in particular exploring the results obtained varying the cavity aspect ratio, the momentum boundary layer thickness and the Reynolds and Mach numbers. It is considered interesting and intriguing to use different parameters on the IC3 solver and to examine the results. It is decided to change the Reynolds and Mach number only, given that an analysis considering every parameter would take a long time, which is not available.
The same cavity's geometry as before is used, without modifying the domain nor the mesh.
The influence of the momentum boundary layer thickness should also be considered, but it is neglected in this thesis work, hence the flow properties are examined for constant Reynolds/Mach while varying respectively the Mach/Reynolds numbers and the momentum thickness.

5.1 Influence of the Reynolds number

Firstly, the Reynolds number's influence on the flow characteristics is investigated. Thanks to the many works cited above, we do know what to expect from these analyses, so it is easy to examine the results and to determine their validity. Again, in order to change the Reynolds number, and applying the fluid dynamic similarity, the viscosity is varied in order to obtain the desired flow non-dimensional parameters. The investigated Reynolds numbers are presented in *Table* 5.1. The interest is to determine the Reynolds interval where the first bifurcation occurs (find a range where the Re_{crit} is contained), and to consider higher Reynolds to determine the phenomena occurring.

Following what stated by Brès and Colonius [28], changing the Reynolds number has a direct influence on the growth rate of the most amplified mode, so it has a direct effect on the instabilities development in the flow structure. Increasing the Reynolds number usually tends to increase the growth rate and to slightly decrease the oscillation frequency of the modes.
Considering that we are not fixing the momentum boundary layer thickness, it is

Reynolds
200
250
350
400
450
502
650
800

Table 5.1: *Reynolds numbers used for studying its influence on the development of the instabilities. The interest is to define a range of Reynolds number containing the critical value to which the first bifurcation occurs, and to see the phenomena occurring to higher Reynolds numbers.*

mandatory for us to consider the influence of the Reynolds number on θ to also evaluate its influence on the flow. In general, approximating our case with a Blasius boundary layer profile (even if we are considering a compressible flow), we have a dependence of the momentum boundary layer thickness with the Reynolds number. In particular, following Blasius it would be:

$$\begin{cases} \theta \propto Re^{-\frac{1}{2}} \text{ for laminar boundary layers} \\ \theta \propto Re^{-\frac{1}{5}} \text{ for turbulent boundary layers} \end{cases} \tag{5.1}$$

Even if the solver works in the compressible regime, we consider the momentum thickness to decrease while increasing the Reynolds number. This approximation is used also by Yiyang Sun et al. [38]. Consequently, as showed previously, the growth rate will again increase.
The whole analysis presented in *Chapter* 4 is again executed to see the influence of the Reynolds number on the flow' s stability. The same mesh is used in order to have the least amount of differences between the cases.
Initially the flow inside the cavity is studied using the Fast Fourier Transform to extrapolate the shedding frequency inside the shear layer. In *Figure* 5.1 it is possible to see how, by increasing the Reynolds number, the Strouhal number relative to the shedding phenomena occurring in the cavity increases too.

Reynolds	**Strouhal**	Δ $[s]$	χ
200	/	0.080	15
250	/	0.080	15
350	0.0542	0.085	20
400	0.0551	0.085	20
450	0.0570	0.090	20
502	0.0572	0.090	20
650	0.0591	0.120	40
800	0.0616	0.150	60

Table 5.2: *In the table the different Strouhal numbers obtained from the FFT are showed for each different Reynolds number. It is again possible to see how the shedding frequency increases as the Reynolds does. In the last two columns the parameters used for the SFD are listed. As the Reynolds number is increased, it is necessary to increase the gain parameter to obtain the convergence of the residuals.*

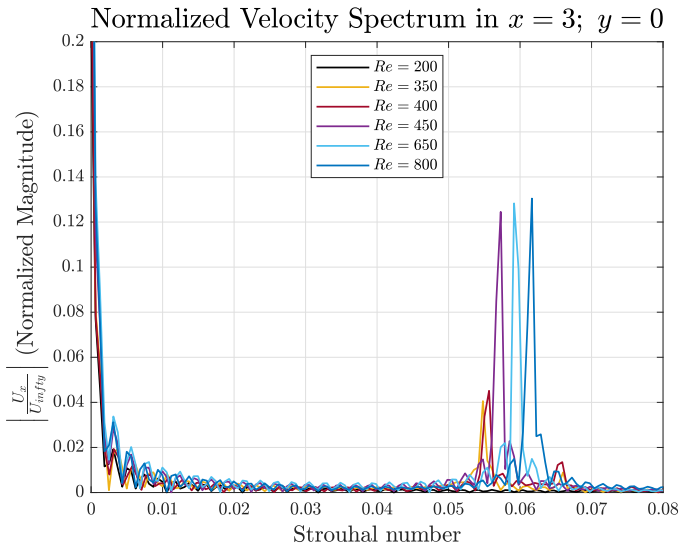

Figure 5.1: *FFT of the signal inside the cavity, specifically in the position $x = 3$, $y = 0$. It is possible to see that the Strouhal number relative to the shedding phenomena occurring in the shear layer increases as the Reynolds does. Without putting too much attention on the peaks' magnitudes, it is still possible to observe the expected trend. Please note that for $Re = 200$ no evident peak is observed, suggesting that the flow is stable under this condition.*

From the FFT it is possible to define the parameters that are used in the Selective Frequency Damping. In order to find the stationary base flow is in fact necessary to cut out the instabilities by imposing a low pass filter on the flow. The parameters that have to be chosen using the SFD are the Δ, which is the filter's width, and the gain χ, that determines the convergence's speed (*Table* 5.2).
The base flow is then determined for every different Reynolds number. Looking at the streamlines of the velocity magnitude U it is possible to appreciate the differences between the different cases (*Figure* 5.2). In the picture, going from (a) to (h) the Reynolds numbers listed in *Table* 5.1 are used. While for the first two cases (corresponding to $Re = 200$ (a) and $Re = 250$ (b)) the DNS simulation is sufficient

to obtain the fixed point directly, in the other cases the Selective Frequency Damping had to be applied in order to achieve the base flows. As the Reynolds number is increased, the main eddy tends to grow in size, and a stretched secondary eddy appears in the cavity (cases $(c) - (f)$). Continuing to increase the Reynolds number a recirculation bubble develops at the bottom of the cavity (case (g)), and its size grows further increasing the non-dimensional parameter as showed in case (h).

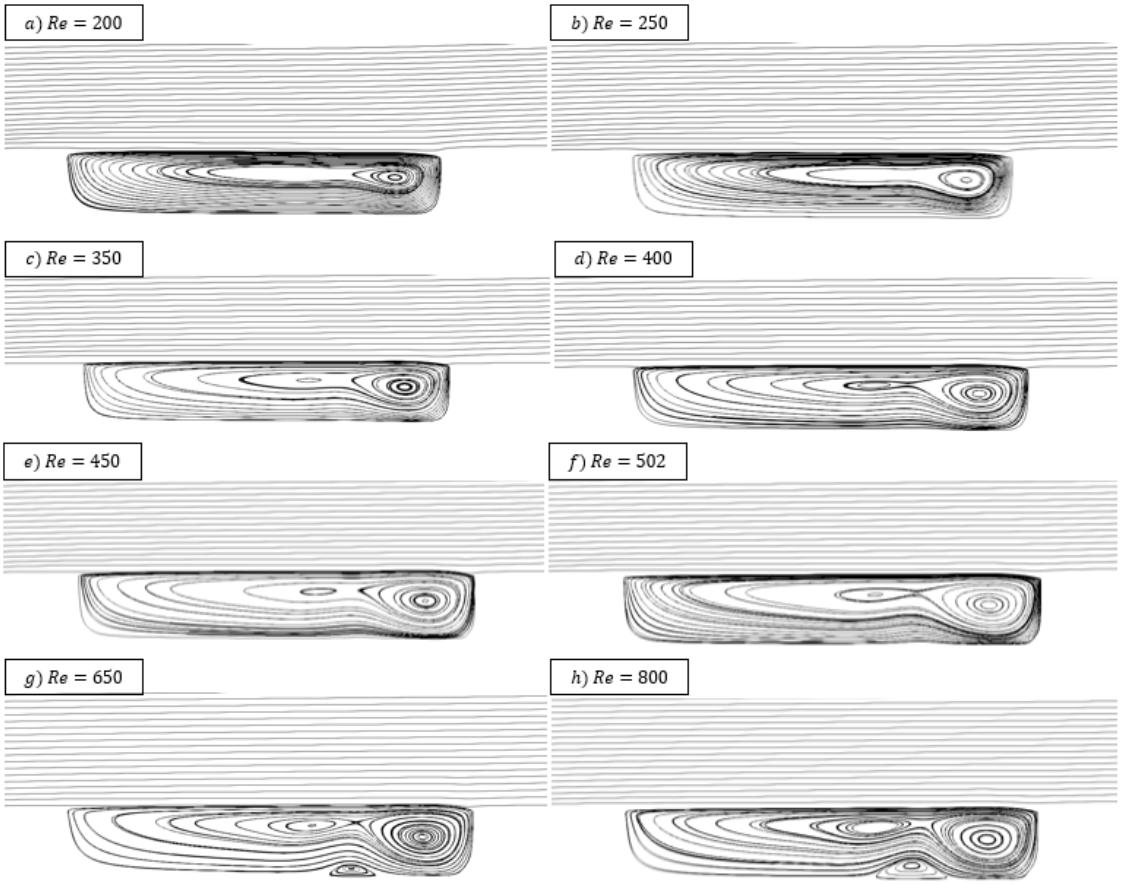

Figure 5.2: *Different base flows used for the stability analyses. From (a) to (h) the pictures correspond to the Reynolds numbers listed in Table 5.2. Cases (a) and (b) correspond to globally stable cases, so it is not necessary to apply the selective frequency dumping technique to obtain the fixed points. Increasing the Reynolds number (cases (e) and (f)) it is evident that a secondary eddy starts to develop while the main eddy tends to grow in size. When higher Reynolds are reached as in (g), a small recirculation bubble develops on the bottom surface of the cavity, and its size continues to grow until case (h) is obtained.*

At this point the global stability analysis is conducted for all the different cases.
The parameters ϵ and τ that define the Chiba method are chosen so that $\epsilon = 1e^{-7}$ for each different Reynolds number and $\tau = \frac{1}{10} \cdot \Delta$, where Δ is the time parameter that is already used for setting the SFD.
Twenty eigenvalues are requested to the solver, so in order to set the Krylov-Schur method the subspace's dimension is set to $m = 100$, given that $m > k$ 'wanted' eigenvalues for the definition of the Arnoldi factorization.
The resulting eigenspectra is showed in *Figure* 5.3.

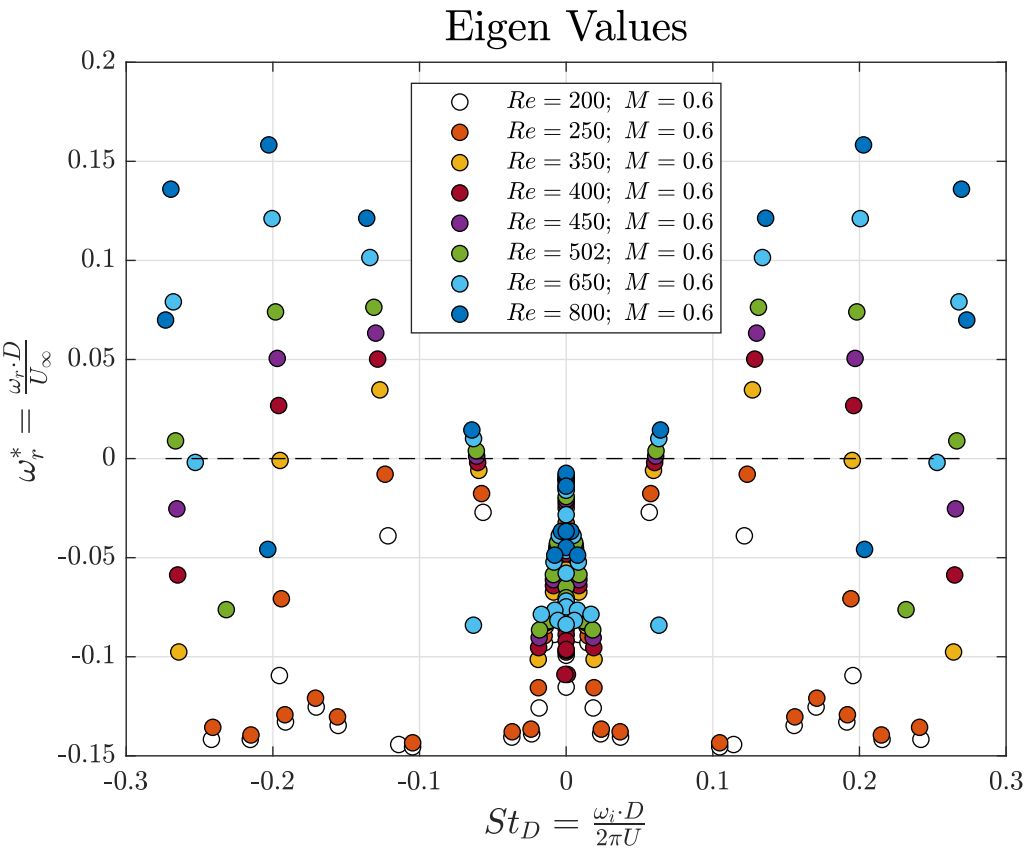

Figure 5.3: *Eigenspectra showing the Reynolds influence on the global modes. Please remember that the momentum boundary layer thickness is not fixed, so we can suppose that it has an influence on the results. It is evident how the growth rate increases as the Reynolds number increases, so that the base flow tends to become more unstable. More detailed comments will be executed soon about each mode.*

Given that is is evident how the hierarchy of the different modes changes while increasing the Reynolds number, we identify the different modes using the different wave number they are related to.
As it was explained in *Chapter* 4, in order to determine the wave numbers of the modes a spatial FFT is executed on the x-component of the real part of the velocity, $\Re(\hat{U}_x)$. The obtained wave number are the same previously determined (*Table* 5.3).

Mode	**Wave number** α $\left[\frac{rad}{m}\right]$
$mode_{1.57}$	1.57080
$mode_{2.09}$	2.09440
$mode_{2.62}$	2.61800
$mode_{0.88}$	0.87632

Table 5.3: *Table containing the dominant wave numbers for the four modes denoting the shedding phenomena. They are determined applying a spatial FFT to the signal over a line inside the shear layer along the x direction.*

It is then possible to study the evolution of each mode as the Reynolds increases (*Figure* 5.4):

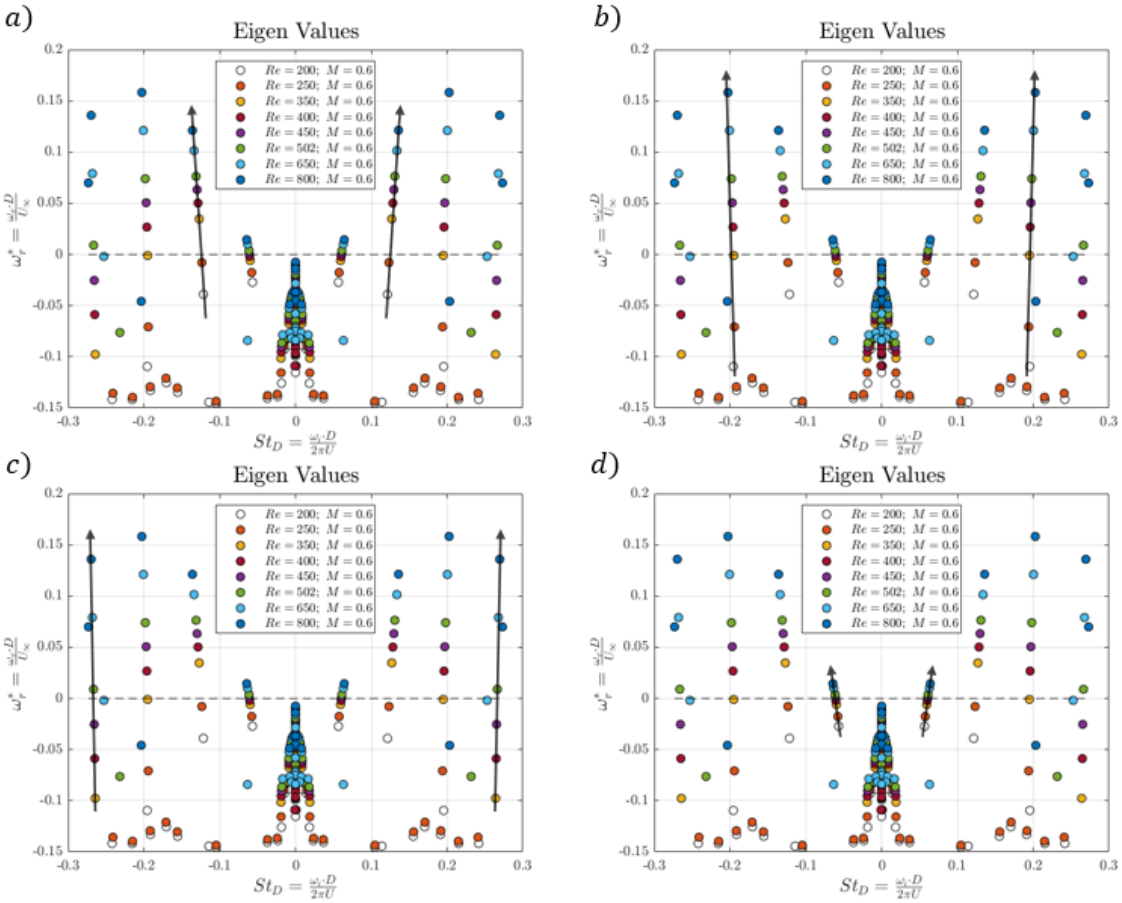

Figure 5.4: *Again, the influence of the Reynolds number on the eigenspectra is showed. The four pictures represents the modes with the same wave numbers listed in Table 4.5. The black arrows aim to put in evidence how each mode evolves with the Reynolds number. It is possible to see how the general trend is for the frequency to slightly increase, and for the growth rate to evidently increase as well. The hierarchy of the different modes changes: the* $mode_{1.57}$ *(a) is the most amplified mode at lower Reynolds, while it leaves its place to the* $mode_{2.09}$ *as the Reynolds reaches values of* $Re = 650 - 800$*. Moreover,* $mode_{0.88}$ *becomes the least stable mode at* $Re = 200$*, as it is possible to see in picture (d). In conclusion, we can see that some modes are not present any more when the Reynolds decreases: specifically in picture (c) note that* $mode_{2.62}$ *disappears as the Reynolds is lower than* $Re = 350$*.*

Looking at the different pictures it is possible to see how the hierarchy of the different modes changes. In subplot (a) the $mode_{1.57}$ is the most amplified/least stable from $Re = 250$ to $Re = 502$, while going to higher Reynolds number it is possible to see how the most amplified mode becomes $mode_{2.09}$, whose evolution is well represented in subplot (b). Please note that $mode_{2.62}$ (subplot (c)) is not present for Reynolds number lower than $Re = 350$. In conclusion, $mode_{0.88}$ become the least stable mode when the Reynolds number reaches value around $Re = 250$ or lower.

From this study it is also possible to determine the critic Reynolds for this configuration of the cavity. Looking at *Figure* 5.4 it is evident that for Reynolds lower than $Re = 250$ there are not any amplified modes, so the base flow is stable. In order to determine qualitatively the critic Reynolds Re_{crit} it is possible to analyse the dominant mode in the eigenspectra, which in this case is $mode_{1.57}$, for the two Reynolds numbers $Re = 250$ and $Re = 350$.

Considering a linear evolution of the eigenvalue in the plot, it is possible to execute a simple calculation to obtain an approximation of the Re_{crit}, in particular, weighting the contributions of the growth rates of the modes at the different Reynolds numbers:

$$Re_{crit} = \frac{\Delta Re}{\left(\frac{|\omega^*_{r,Re=350}|}{|\omega^*_{r,Re=250}|}\right) + 1} + Re_{250} \tag{5.2}$$

Using this technique (maintaining a certain degree of simplification), the critic Reynolds is (*Figure* 5.5):

$$Re_{crit} = 268.54 \tag{5.3}$$

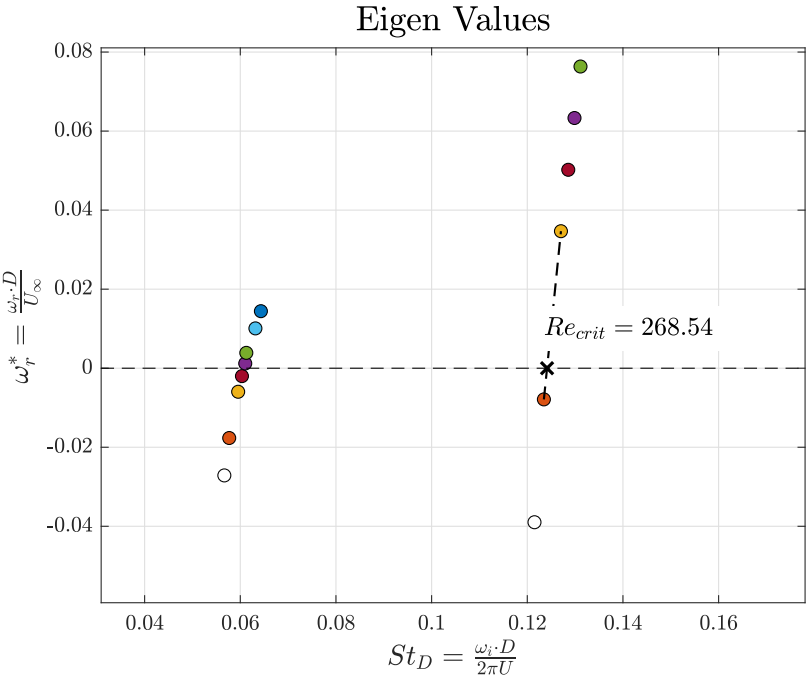

Figure 5.5: *Evaluation of the critic Reynolds by weighting the growth rates of the dominant mode (which is mode$_{1.57}$). By considering a linear behaviour between the two values, it is possible to define a critic Reynolds equal to $Re = 268.54$. This result surely is an approximation that could be improved by executing analyses for Reynolds numbers intermediate to the two adopted here.*

Looking at the eigenspectra in *Figure* 5.3, some final observations can be made. When a higher Reynolds number is studied, new modes appears in the spectra. Particularly from $Re = 502$ to $Re = 800$ two new non-negligible modes are present (*Figure* 5.6):

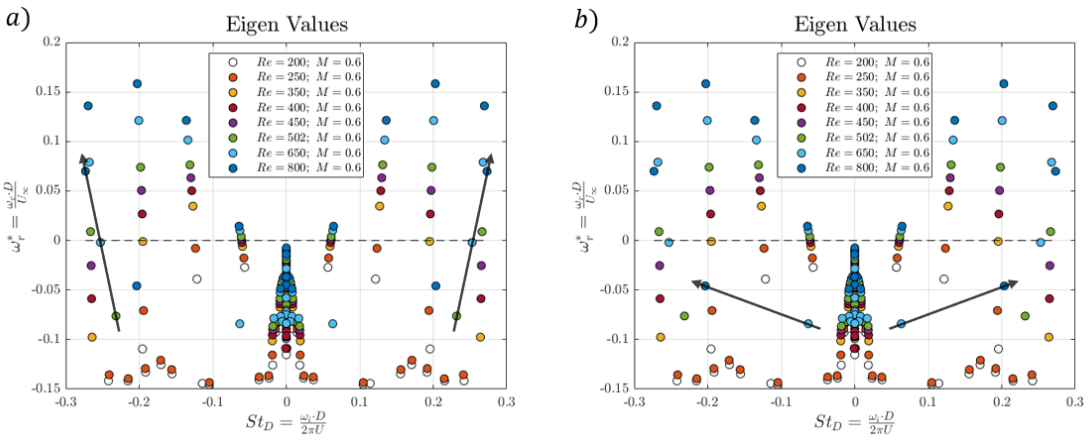

Figure 5.6: *Two different modes appear when the Reynolds number is increased towards higher values. It is evident that the frequency of these modes changes in a greater fashion then for the shedding modes. No further studies are executed on these two modes, but we can suppose that they are a direct consequence of a new destabilizing phenomena.*

These two different modes have a different behaviour compared to the four shedding modes analysed before: the frequency is in fact increasing with the Reynolds number, especially the mode represented in (*b*). The phenomena that generates these modes is not further investigated, but as shown in Brès and Colonius [28] we can suppose these modes refers to centrifugal instabilities occurring in the cavity.

To complete the study about the influence of the Reynolds number on the global modes of the cavity, the fictitious local stability analysis is performed in order to see how the dispersion relation changes. In particular, the study is conducted on the first four modes listed in *Table* 5.3. Applying again a spatial Fast Fourier Transform on the velocity signal $\Re(\hat{U}_x)$ for each mode, the dominant wave number is extrapolated. As expected, the wave number is the same already discovered, so we can use this first study as a check for the results previously obtained.
Following the procedure explained in *Chapter* 4, as the wave number are calculated again, it is possible to plot the dispersion relation as $\omega_r^*(\alpha)$ and $St_D(\alpha)$.
The two plots are represented in *Figure* 5.7.
Looking at the $\omega_r^*(\alpha)$ graph, it is again evident how the hierarchy of the different modes changes, as previously explained in details. It would be possible to extrapolate the critic Reynolds from this plot instead of using the same method applied to the eigenspectra. Again we can see that we have a parabolic behaviour coherent with bibliography (Nastro et al. [36]).
Similar comments may be done about the $St_D(\alpha)$ graph. Please note that a generic polynomial curve has been fitted with the values obtained. The fit curve is probably not representative of the real behaviour of the Strouhal number, but it is important to note that the behaviour is most certainly not linear, given that different phase velocities are obtained for the modes and that the medium is definitely dispersive.

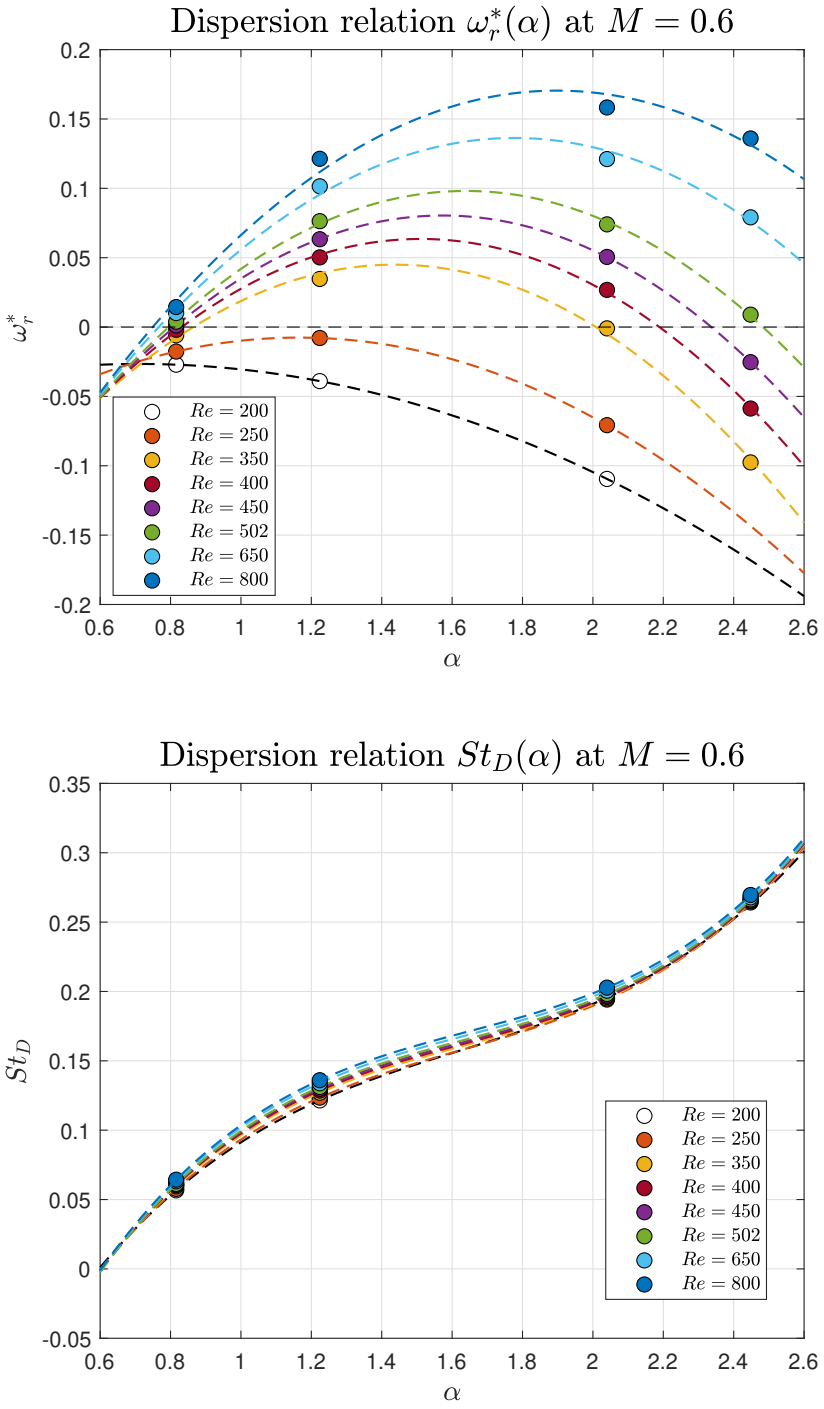

Figure 5.7: *The two plots represent the influence of the Reynolds number on $\omega_r^*(\alpha)$ and $St_D(\alpha)$ for a fixed Mach number $M = 0.6$. Looking at the plot representing $\omega_r^*(\alpha)$ it is possible to again appreciate the changes in the hierarchy of the different modes: while $mode_{0.88}$ is dominant (it is the least amplified mode) for low Reynolds number, $mode_{1.57}$ is the most influencing for intermediate Reynolds number and $mode_{2.09}$ becomes the most amplified at $Re = 650 - 800$. From this graph the critic Reynolds can be obtained applying the method previously shown. From the $St_D(\alpha)$ graph, we again get the information about the medium, clearly dispersive as the general trend is not linear. Please note that the polynomial fit used to interpolate the results on this graph is not necessarily the real trend of $St_D(\alpha)$, but it is used to put in evidence the non-linear behaviour of the frequency.*

5.2 Influence of the Mach number

After the study about the Reynolds' influence on the global modes of the cavity, as it was said during the introduction of this chapter, the Mach number's influence is investigated.
As well as for the Reynolds' influence analyses, the boundary layer momentum thickness is let a free parameter, so we can consider again an influence of this parameter on the results. The Reynolds number was this time fixed to $Re = 502$, as in the original case also proposed by Sun et al. [11].
The fluid dynamic similarity is again introduced in order to obtain the desired non-dimensional parameters for the flow. Basically, the fluid velocity and the dynamic viscosity are modified to change the Mach number. A list of the adopted Mach numbers is showed in *Table* 5.4.

Mach
0.3
0.4
0.5
0.6
0.7

Table 5.4: *Mach numbers used for studying its influence on the development of the instabilities. The interest is to define a range of Mach number vast enough to compare the general trend of the different modes with the one suggested from bibliography.*

Following what stated by Yamouni, Sipp, and Jacquin [29], Mathias and Medeiros [37], changing the Mach number has a direct influence again on the growth rate ω_r^*, that sees different behaviours as the Mach increases. At lower Mach numbers, the compressibility effects are still negligible, and the most amplified modes are connected to the incompressible shear layer modes, with a destabilizing effect of the Mach number. As we increase the Mach number, once the compressibility effect starts acting on the boundary layer, there appears to be a stabilizing effect. As told by Mathias and Medeiros [37], we should then see a peak in the growth rate for a certain intermediate Mach number.
The frequency is told by Brès and Colonius [28] to not be influenced by the Mach numbers, especially when low compressibility effects are taken into consideration. Going towards higher values of M though, we will note a slight change in the Strouhal number: this may be a consequence of using higher Mach numbers where the compressibility effects cannot be neglected.
It was said that the boundary layer momentum thickness is not fixed to a constant value. As a consequence, we expect it to decrease as the Mach increases: as the compressibility effects are not negligible any more, they tend to make the boundary layer thinner. The momentum thickness decreases influencing the growth rates of the different global modes as previously described: given that $\omega_r \propto \frac{U}{\theta}$, we can suppose that there is a slight destabilizing effect of the momentum thickness on the results.

The analyses executed changing the Mach number were realized on the first mesh produced characterized by 127000 elements. The residuals are constantly monitored

to verify that the mesh is suitable for the different cases.
Firstly the velocity signal U_x is analysed in the middle of the cavity ($x = 3;\ y = 0$) to get the characteristic frequency of the shedding phenomena (*Figure* 5.8).

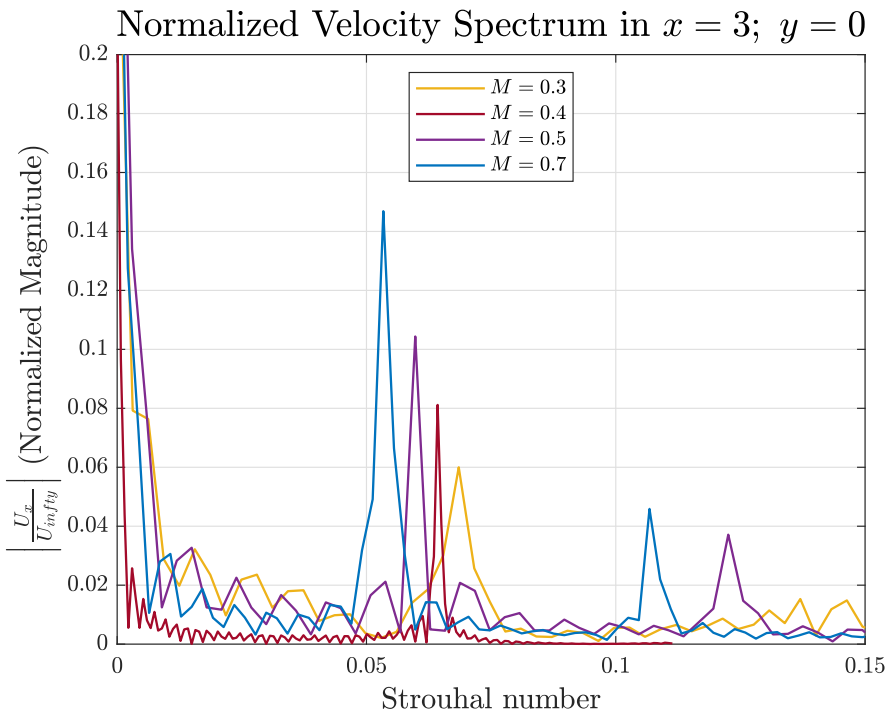

Figure 5.8: *The Mach's influence on the frequency spectrum is depicted here. As the Mach number increases, the Strouhal number of the characteristic shedding phenomena decreases slightly, possibly for the stabilizing effect of compressibility.*

It is possible to see from the frequency spectrum that the characteristic shedding frequency decreases as the Mach number increases. This is probably due to the stabilizing effects of compressibility.

Once the frequencies are obtained it is again possible to apply the Selective Frequency Damping technique to obtain the steady base flow. The different parameters applied are listed in *Table* 5.5:

Mach	**Strouhal**	$\Delta\ [s]$	χ
0.3	0.069	0.143	40
0.4	0.0643	0.114	30
0.5	0.0598	0.110	25
0.6	0.0572	0.090	20
0.7	0.0534	0.079	20

Table 5.5: *In the table the different Strouhal numbers obtained from the FFT are showed for each different Mach number. It is again possible to see how the shedding frequency decreases as the Mach does. In the last two columns the parameters used for the SFD are listed. As the Mach number is decreased, it is necessary to increase the gain parameter to obtain the convergence of the residuals.*

Applying these parameters the base flows are obtained for the different configurations of flow. Again the visualization of the streamlines of the velocity magnitude U are brought to the reader's attention in *Figure* 5.9.

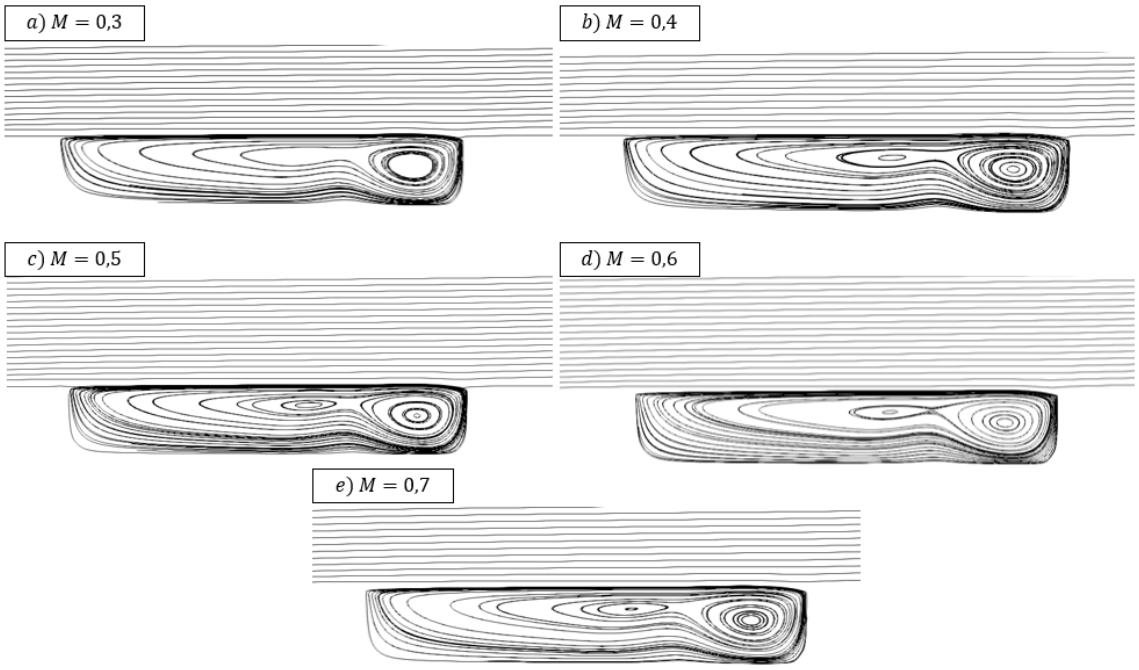

Figure 5.9: *The base flows obtained for the different Mach numbers are here showed using the streamlines of the velocity magnitude U. Compared to the influence of the Reynolds number on the base flow, here there are no evident differences between the cases going from $M = 0.3$ to $M = 0.7$. Even if the increasing value of the Mach number should move the main eddy towards the downstream edge of the cavity, here this effect is not clearly visible. This does not mean that the increasing Mach number won't influence the perturbation's dynamics, as we will see in the eigenspectra.*

We would have expected the main eddy to move towards the downstream edge of the cavity as the Mach number increases. This behaviour is not clearly visible, but we will see that the perturbation's dynamics still changes.
In fact, once the base flow is obtained for each configuration, it is possible to run the stability analysis using again the Chiba difference method, so imposing $\tau = \frac{1}{10} \cdot \Delta$ which is the integration time step, and ϵ which is imposed at 10^{-7} as always. The eigenspectra is then obtained for the different cases (*Figure* 5.10).
From the eigenspectra a few observations can be done: analysing the general trend we can see that each mode reaches a maximum growth rate for intermediate values of the Mach number. In particular, the dominant mode (the most unstable one) reaches a peak value in the growth rate around $M = 0.5$. This behaviour is similar to the one obtained by Mathias and Medeiros [37]. The stabilizing effect of the compressibility tends to influence the perturbation's dynamics approaching higher values of the Mach number, while it is not present when the Mach is still small.

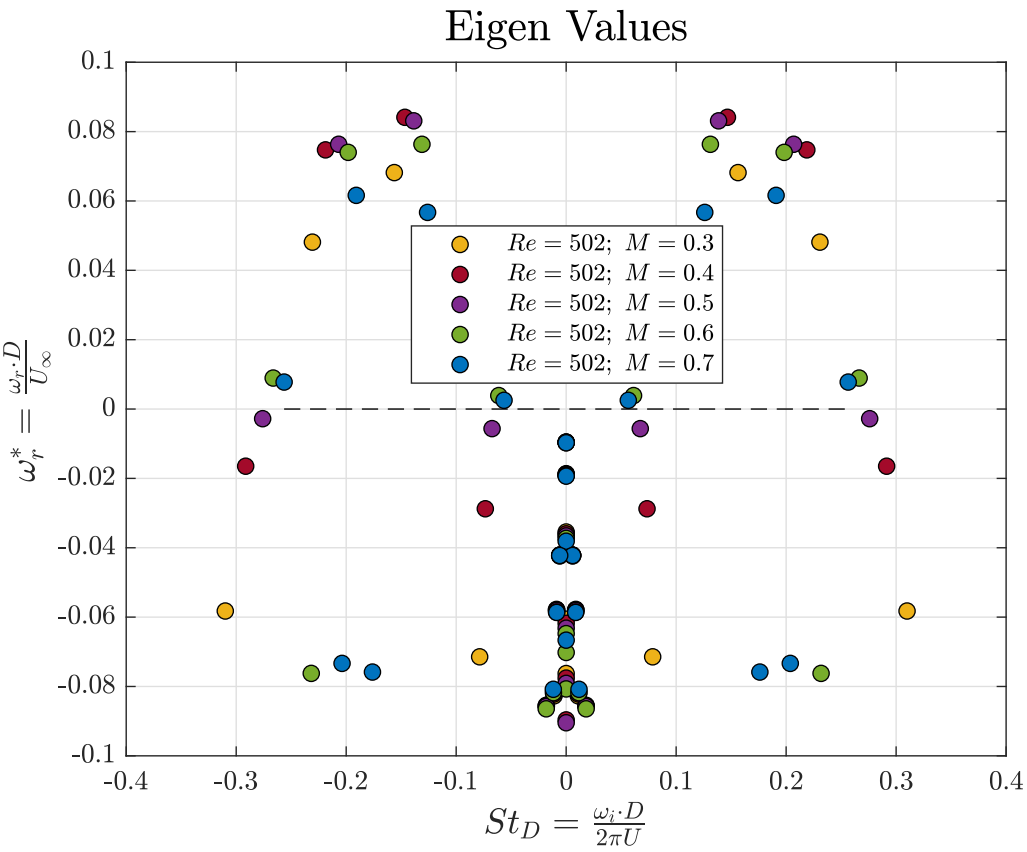

Figure 5.10: *Eigenspectra obtained running the global stability analysis using Chiba difference method on a cavity with aspect ratio* $\frac{L}{D} = 6$*,* $Re = 502$ *and variable Mach. Following the evolution of each mode, it is possible to see that the maximum growth rate of the leading modes is obtained around* $M = 0.5$*. For higher Mach numbers a stabilizing effect occurs. This is a similar behaviour to the one obtained by Mathias and Medeiros [37].*

Looking at the behaviour of each mode in *Figure* 5.11, we acknowledge that the hierarchy remains unvaried between the different cases. There is a single exception which is the most amplified mode: the dominant mode in the range from $M = 0.3$ to $M = 0.6$ becomes the second dominant mode at $M = 0.7$.
The general trend is the same for each one of the four mode studied: going from $M = 0.3$ to $M = 0.5$ the growth rate increases resulting in a destabilizing effect, while for higher Mach numbers this behaviour reverses. This trend is similar to the one showed by Mathias and Medeiros [37].

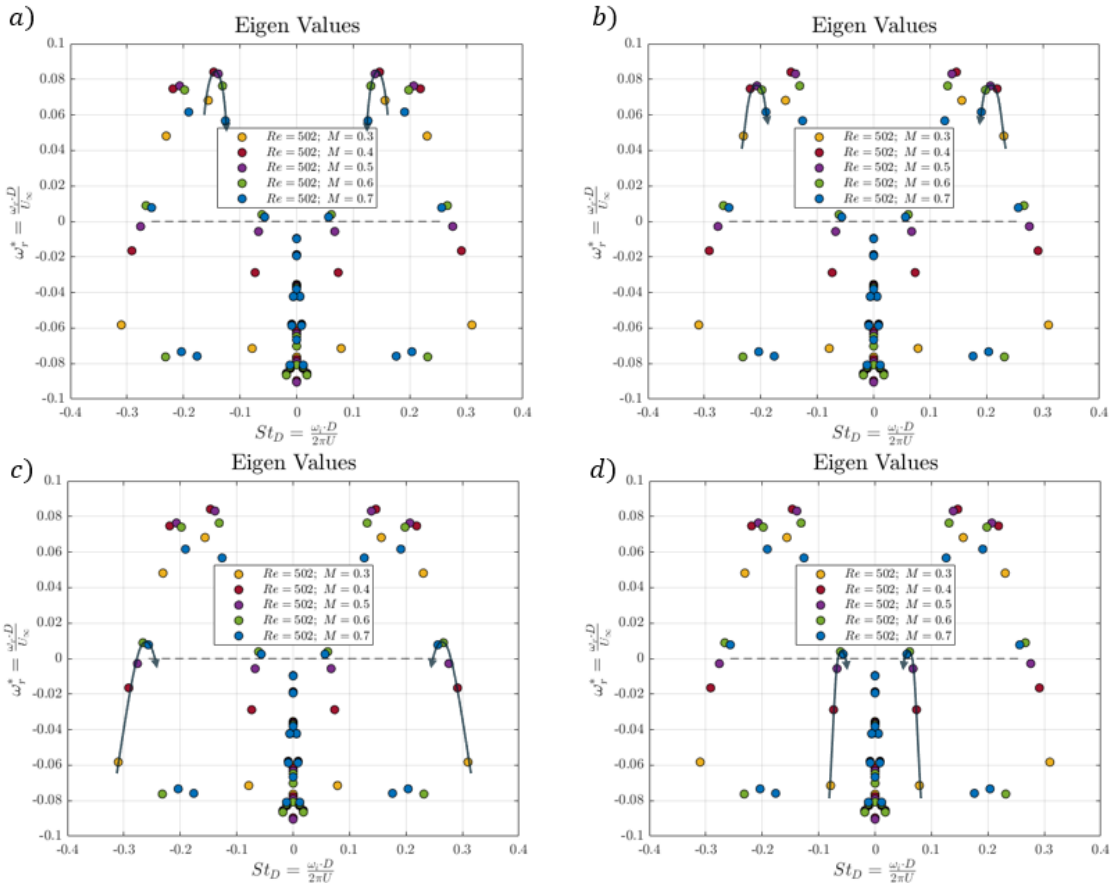

Figure 5.11: *The figure depicts the behaviour of the four modes given by the shedding phenomena at different Mach numbers. Please note that the hierarchy of the different modes remains the same apart from the most amplified mode: while it is the most amplified for Mach going from* $M = 0.3$ *to* $M = 0.6$*, it becomes the second dominant one at* $M = 0.7$*. The other modes maintain the same hierarchy for all the different Mach that were studied. In general we can see how the behaviour changes increasing the Mach number: as from* $M = 0.3$ *to* $M = 0.5$ *the growth rate increases carrying a destabilizing effect, the trend reverses after* $M = 0.5$ *is reached. This behaviour is similar to the one obtained by Mathias and Medeiros [37] for an open cavity flow.*

In order to be sure that the different modes are always related to the shedding phenomena and not to the acoustic resonance, the contours of the real part of $\frac{\hat{U}_x}{u_\infty}$ are showed in the range $[-0.008, 0.008]$ (*Figure* 5.12).

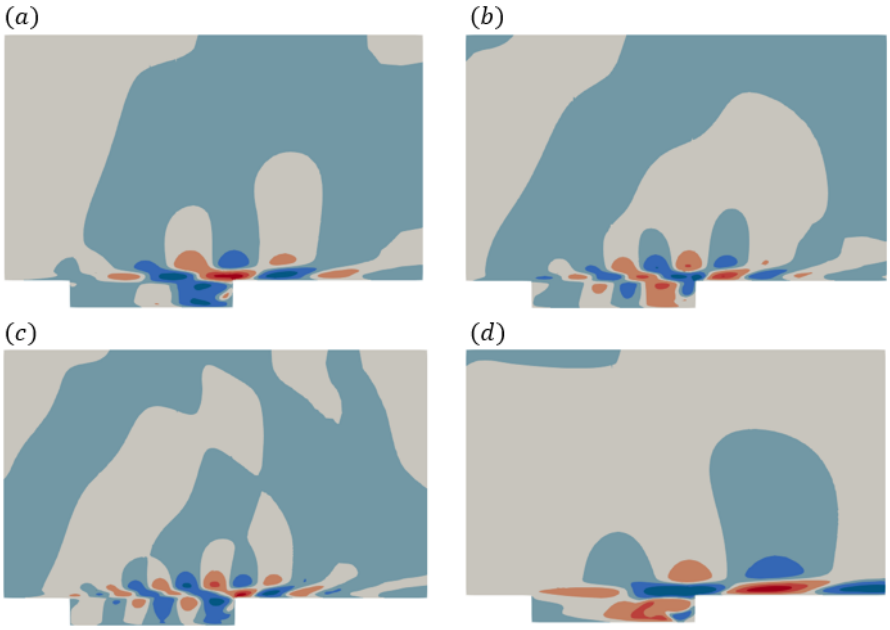

Figure 5.12: *Visualization of the eigenmodes at* $M = 0.4$ *showed as contours of the real part of* $\frac{\hat{U}_x}{u_\infty}$. *In particular,* $\frac{\hat{U}_x}{u_\infty} \in [-0.008, 0.008]$. *From* (a) *to* (d) *the different modes are depicted from the most amplified to the least. The representation is found to be similar for the other cases at different Mach. From this visualizations, similar to the ones showed under the Reynolds influence, we can assume that the shedding phenomena is the one responsible for the flow instability.*

Chapter 6

Conclusions

A modal, global stability analysis has been conducted on a 2D open cavity with aspect ratio $\frac{L}{D} = 6$ under different conditions (specifically changing the Reynolds and Mach numbers) and applying different numerical methods.
The study carries out different results that are coherent with bibliography.
First, a cavity at $Re = 502$ and $M = 0.6$ has been studied in order to compare the results with the paper written by Sun et al. [11]. The same domain used in the article is recreated here to compare the results; a DNS using compressible Navier-Stokes equations is run to determine the frequency of the shedding phenomena developing inside the shear layer of the cavity; applying the Selective Frequency Damping method, the base flow is obtained; the perturbations are applied in form of numerical round-off errors in the boundary layer of the base flow. The eigenspectrum that is obtained shows a great similarity to the one presented in [11]. It is also possible to execute a fictitious local analysis in order to determine the dominant wave numbers of the amplified modes and to obtain their phase velocities.
The same analysis is executed changing the Re and M numbers to consider their influence on the base flow stability. Once again the results obtained show coherence with bibliography. By changing the Reynolds number from lower to higher values, the growth rates of the most amplified (least damped) eigenmodes increase, as showed in Brès and Colonius [28]. It is also possible to determine the critic Reynolds for this cavity geometry, that is found to be equal to $Re_{crit} = 268.54$ considering the cavity depth and freestream velocity as characteristic length and speed respectively. By changing the Mach number, a similar trend to the one obtained by Mathias and Medeiros [37], Yamouni, Sipp, and Jacquin [29] and Sun et al. [26] is obtained. As the Mach goes from low to high values, we first see a destabilizing effect of compressibility that tends to stabilize again the flow approaching the transonic regime.

A future development of this study would be to increase the Reynolds number approaching turbulent flows, and developing stability analysis on a system studied using the RANS equations. Furthermore, it would be useful to determine a map of critic Reynolds and Mach numbers for different Mach and Reynolds number respectively.

Bibliography

[1] Louis Cattafesta et al. "Review of Active Control of Flow-Induced Cavity Resonance". en. In: Orlando, Florida, June 2003, p. 21.

[2] Clarence W. Rowley and David R. Williams. "DYNAMICS AND CONTROL OF HIGH-REYNOLDS-NUMBER FLOW OVER OPEN CAVITIES". en. In: *Annual Review of Fluid Mechanics* 38.1 (Jan. 2006), pp. 251–276.

[3] Daniel Prudhomme et al. "Flight Tests of Passive Flow Control for Suppression of Cavity Aeroacoustics". en. In: *Journal of Aircraft* 58.4 (July 2021), pp. 907–916.

[4] Louis N. Cattafesta et al. "Active control of flow-induced cavity oscillations". en. In: *Progress in Aerospace Sciences* 44.7-8 (Oct. 2008), pp. 479–502.

[5] Scott C. Morris. "Shear-Layer Instabilities: Particle Image Velocimetry Measurements and Implications for Acoustics". en. In: *Annual Review of Fluid Mechanics* 43.1 (Jan. 2011), pp. 529–550.

[6] Clarence W. Rowley, Tim Colonius, and Amit J. Basu. "On self-sustained oscillations in two-dimensional compressible flow over rectangular cavities". en. In: *Journal of Fluid Mechanics* 455 (Mar. 2002), pp. 315–346.

[7] Lloyd N. Trefethen and David Bau Iii. *Numerical Linear Algebra*. en. Philadelphia, PA: Society for Industrial and Applied Mathematics, Jan. 1997.

[8] MORKOVIN M. V. "Transition in open flow systems-a reassessment". In: *Bull. Am. Phys. Soc.* 39 (1994), p. 1882.

[9] Stefania Cherubini, Francesco Picella, and Jean-Christophe Robinet. "Variational Nonlinear Optimization in Fluid Dynamics: The Case of a Channel Flow with Superhydrophobic Walls". en. In: *Mathematics* 9.1 (Dec. 2020), p. 53.

[10] Milton Van Dyke, ed. *An album of fluid motion*. eng. 12. printing. Stanford, Calif: Parabolic Press, 2008.

[11] Y. Sun et al. "Spanwise effects on instabilities of compressible flow over a long rectangular cavity". en. In: *Theoretical and Computational Fluid Dynamics* 31.5-6 (Dec. 2017), pp. 555–565.

[12] Pijush K. Kundu et al. *Fluid mechanics*. eng. Sixth Edition. Amsterdam Boston Heidelberg London: Elsevier, Academic Press, 2016.

[13] Laura Victoria Rolandi. "Stability of low Reynolds number compressible flows". PhD Thesis. 2021.

[14] François Charru. *Instabilités hydrodynamiques*. fre. Les Ulis: EDP Sciences, 2014.

[15] Vicente Hernandez, Jose E. Roman, and Vicente Vidal. "SLEPc: A scalable and flexible toolkit for the solution of eigenvalue problems". en. In: *ACM Transactions on Mathematical Software* 31.3 (Sept. 2005), pp. 351–362.

[16] G. W. Stewart. "A Krylov–Schur Algorithm for Large Eigenproblems". en. In: *SIAM Journal on Matrix Analysis and Applications* 23.3 (Jan. 2002), pp. 601–614.

[17] R. A. S. Frantz, J.-Ch. Loiseau, and J.-Ch. Robinet. "Krylov Methods for Large-Scale Dynamical Systems: Application in Fluid Dynamics". en. In: *Applied Mechanics Reviews* 75.3 (May 2023), p. 030802.

[18] Satoshi CHIBA. *Three-Dimensional Global Stability Analysis for the Time-Periodic Cylinder Wake*. en. 2001.

[19] Asei Tezuka and Kojiro Suzuki. "Three-Dimensional Global Linear Stability Analysis of Flow Around a Spheroid". en. In: *AIAA Journal* 44.8 (Aug. 2006), pp. 1697–1708.

[20] Kunihiko Taira et al. *Modal Analysis of Fluid Flows: An Overview*. arXiv:1702.01453 [physics]. Aug. 2017.

[21] Peter J. Schmid. "Nonmodal Stability Theory". en. In: *Annual Review of Fluid Mechanics* 39.1 (Jan. 2007), pp. 129–162.

[22] Vassilios Theofilis. "Global Linear Instability". en. In: *Annual Review of Fluid Mechanics* 43.1 (Jan. 2011), pp. 319–352.

[23] Paolo Luchini and Alessandro Bottaro. "Adjoint Equations in Stability Analysis". en. In: *Annual Review of Fluid Mechanics* 46.1 (Jan. 2014), pp. 493–517.

[24] Vincenzo Citro et al. "Linear three-dimensional global and asymptotic stability analysis of incompressible open cavity flow". en. In: *Journal of Fluid Mechanics* 768 (Apr. 2015), pp. 113–140.

[25] Yiyang Sun et al. *Resolvent analysis of compressible laminar and turbulent cavity flows*. arXiv:1909.06299 [physics]. Sept. 2019.

[26] Yiyang Sun et al. "Biglobal instabilities of compressible open-cavity flows". en. In: *Journal of Fluid Mechanics* 826 (Sept. 2017), pp. 270–301.

[27] Marlon Sproesser Mathias and Marcello A. F. Medeiros. "The effect of incoming boundary layer thickness and Mach number on linear and nonlinear Rossiter modes in open cavity flows". en. In: *Theoretical and Computational Fluid Dynamics* 35.4 (Aug. 2021), pp. 495–513.

[28] Guillaume A. Brès and Tim Colonius. "Three-dimensional instabilities in compressible flow over open cavities". en. In: *Journal of Fluid Mechanics* 599 (Mar. 2008), pp. 309–339.

[29] Sami Yamouni, Denis Sipp, and Laurent Jacquin. "Interaction between feedback aeroacoustic and acoustic resonance mechanisms in a cavity flow: a global stability analysis". en. In: *Journal of Fluid Mechanics* 717 (Feb. 2013), pp. 134–165.

[30] Peter Roger Bailey, Antonella Abbá, and Daniela Tordella. "Pressure and kinetic energy transport across the cavity mouth in resonating cavities". en. In: *Physical Review E* 87.1 (Jan. 2013), p. 013013.

[31] F. Meseguer-Garrido et al. "On linear instability mechanisms in incompressible open cavity flow". en. In: *Journal of Fluid Mechanics* 752 (Aug. 2014), pp. 219–236.

[32] J.C. Butcher. *Numerical Methods for Ordinary Differential Equations*. en. 1st ed. Wiley, June 2003.

[33] Espen Åkervik et al. "Steady solutions of the Navier-Stokes equations by selective frequency damping". en. In: *Physics of Fluids* 18.6 (June 2006), p. 068102.

[34] Jordi Casacuberta et al. "Effectivity and efficiency of selective frequency damping for the computation of unstable steady-state solutions". en. In: *Journal of Computational Physics* 375 (Dec. 2018), pp. 481–497.

[35] Miguel Fosas De Pando, Denis Sipp, and Peter J. Schmid. "Efficient evaluation of the direct and adjoint linearized dynamics from compressible flow solvers". en. In: *Journal of Computational Physics* 231.23 (Oct. 2012), pp. 7739–7755.

[36] G. Nastro et al. "Global stability, sensitivity and passive control of low-Reynolds-number flows around NACA 4412 swept wings". en. In: *Journal of Fluid Mechanics* 957 (Feb. 2023), A5.

[37] Marlon Sproesser Mathias and Marcello Augusto Faraco de Medeiros. "The effect of Mach number on open cavity flows with thick or thin incoming boundary layers". In: (2022). Publisher: arXiv Version Number: 2.

[38] Yiyang Sun et al. "Numerical Simulations of Subsonic and Transonic Open-Cavity Flows". In: *7th AIAA Theoretical Fluid Mechanics Conference* (2014).